Aerosol Printing of Colloidal Nanocrystals by Aerodynamic Focusing

A DISSERTATION

SUBMITTED TO THE FACULTY OF THE GRADUATE SCHOOL

OF THE UNIVERSITY OF MINNESOTA

BY

Lejun Qi

IN PARTIAL FULFILLMENT OF THE REQUIREMENTS

FOR THE DEGREE OF

DOCTOR OF PHILOSOPHY

David J. Norris and Steven L. Girshick, Advisors

July 2010

Acknowledgements

There are many who have helped me along this five-year journey.

Foremost, I thank my advisors, Professor David Norris and Professor Steven Girshick. Any successes that I have enjoyed would not have been possible without their guidance, patience, and enthusiasm. I am grateful to my unofficial advisor, Professor Peter McMurry, for his advice and support during the past years. I feel very lucky to have had the opportunity to work with them.

I would like to express my gratitude to my dissertation committee members, Professor Eray Aydil and Professor Chris Macosko, for their time and efforts in reviewing my thesis and their valuable suggestions.

I would also like to thank many former and current colleagues from the Norris group, the high temperature and plasma lab, and the particle technology lab, for their insightful discussions and help along the way. Particularly, I thank Andy Wills for his help with chemical synthesis, and Jacob Scheckman for his assistance with aerosol measurements. My thanks also go to Dr. Sang Eon Han, Dr. Linli Meng, Dr. Kurtis Leschkies, Dr. Prashant Nagpal, William Tisdale, Moon Sung Kang, Ayash Sahu, Ankur Khare, Katie Crawford, Jong Hyuk Park, Joel Thomas, Dr. Xiaoliang Wang, Dr. Ken Iida, Dr. Jami Hafiz, Dr. Rajesh Mukherjee, Aaron Beaber, Adam Boies, Ricky Jain, and Pingyan Lei, for all the support they gave me and the happy environment they create in the lab.

Finally, I thank my parents. Words cannot begin to convey my love and gratitude towards them. They have always been with me through the difficult times of my life. Special

thanks to Jian Wang for her love, understanding, patience, and sacrifice. This thesis would not have been possible without their support and encouragement.

This thesis research was supported financially by NSF Nanoscale Interdisciplinary Research Team (NIRT) program (CTS-0506748) and utilized resources at the University of Minnesota Characterization Facility, funded by NSF through the NNIN program.

Abstract

Colloidal semiconductor nanocrystals, or quantum dots, have shown promise as the active material in electronic and optoelectronic applications, because of their high quantum yield, narrow spectral emission band, size-tunable bandgap, chemical stability, and easy processibility. Meanwhile, it is still challenging to print patterns of nanocrystal films with desired linewidth and thickness, which is a critical step in fabrication of nanocrystal-based devices. In this thesis, a direct-write method of colloidal semiconductor nanocrystals has been developed. Like other direct-write techniques, this aerosol based method simplifies printing process and reduces the manufacturing cost, as it avoids mask screening, lithography, and pre-patterning of the substrate. Moreover, the aerosol printing with aerodynamic lenses needs neither microscale nozzles nor sheath gases, and is able to incorporate into the vacuum systems currently used in microelectronic fabrication. This thesis research presents systematic efforts to develop an aerosol-based method to directly write patterns of semiconductor nanocrystals from colloidal dispersions by aerodynamic focusing.

First, the synthesized colloidal nanocrystals in hexane were nebulized into compact and spherical agglomerates suspending in the carrier gas. The details about the impact dynamics of individual aerosolized nanocrystal agglomerates were investigated. As building blocks of printed nanocrystal films, the agglomerate exhibited cohesive and granular behaviors during impact deformation on the substrate. The strength of cohesion between nanocrystals in the agglomerates could be adjusted by tuning the number concentration of colloidal nanocrystal dispersion.

Second, ultrathin films of nanocrystals were obtained by printing monodisperse nanocrystal agglomerates. As the result of the granular property of nanocrystal agglomerates, it was found that the thickness of deposited agglomerates strongly depended on the size of agglomerates. A single monolayer film of nanocrystals was attained by aerodynamically focusing 40-nm nanocrystal agglomerates and translating the carbon substrate at a velocity of 10 μm/s. The formation of nanocrystal films during printing was found strongly influenced by the substrate surface wettability.

Third, microscale towers, lines, and patterns were obtained by printing polydisperse nanocrystal agglomerates. The thickness and line width of the patterns were adjustable by altering experimental conditions. Micropatterns of linewidth of less than 10 μm were demonstrated. Upon exposure to near-UV illumination, the printed nanocrystals exhibited robust fluorescence in the visual, with the color depending on the diameter of the individual nanocrystals.

Table of Contents

List of Tables

List of Figures

1

Introduction

1.1 Semiconductor Nanocrystals (Quantum Dots)

Semiconductor nanocrystals (NCs) or *quantum dots* are a crystalline material with dimensions that approach the Bohr radius of the exciton in the bulk material. The size of NCs ranges from several to around 20 nm. Their unique electrical and optical properties which can be tailored through careful manufacturing processes, makes them one of the hottest research topics in the past decades. The distinct properties of a semiconductor NC originate from its size which nears the natural length of the exciton. Hence the energy bands of the bulk material are quantized due to the potential well made by the boundaries of the NC for the carriers. This phenomenon is known as the *quantum-confinement effect*.

1.1.1 Quantum-confinement Effect

To give a quantitative description of this effect, a simple model named the particle-in-a-sphere model can be used.[1-2] In this model, a spherical NC is surrounded by an infinite

potential barrier. The energy of the electron and hole quantum-size levels, characterized by angular momentum quantum number *l*, can be written in a parabolic approximation as

$$E_{l,n}^{e,h} = \frac{\hbar^2 \phi_{l,n}^2}{2m_{e,h}a^2}, \tag{1-1}$$

where $m_{e,h}$ is the electron and hole effective mass, respectively, a is the nanocrystal radius and $\phi_{l,n}$ is the nth root of the spherical Bessel function of order l.

The Coulomb interaction between the electrons and holes confined within a NC should always be taken into account in the energy estimation. To the first-order perturbation approximation of the Coulomb interaction, the electron-hole pair energy states labeled by a set of quantum numbers ($n_h l_h n_e l_e$) can be described as

$$E_{ehp} = E_g + \frac{\hbar^2}{2a^2}\left(\frac{\varphi_{l_e,n_e}^2}{m_e} + \frac{\varphi_{l_h,n_h}^2}{m_h}\right) \underbrace{- \frac{1.8e^2}{\epsilon a}}_{\textbf{Coulomb Interaction}} \tag{1-2}$$

where, E_g is the bulk band gap, $\varphi_{l,n}$ is the atomic wave function determined from linear combination of atomic orbitals (LCAOs) approximation and ε is the dielectric constant of the semiconductor. The band structure based on this model is shown in Figure 1-1.

Hence, the energy of the lowest electron and hole pair level ($1S_h 1S_e$) increases with decreasing NC size and the total energy of the band edge optical transitions increases, too. Thus, for the photoluminescence of the NC's, we can control the wavelength of the light emission by adjusting the NC size a.

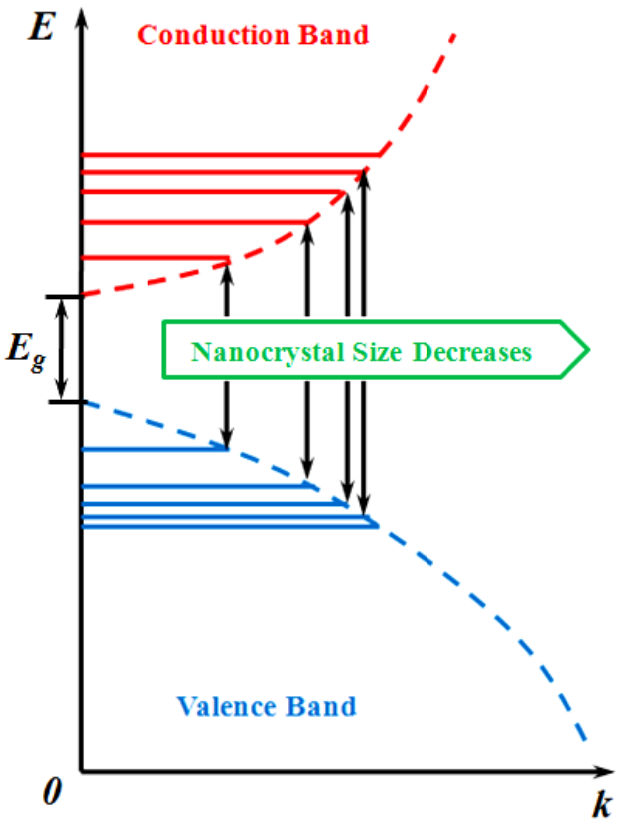

Figure 1-1. Band structure schematic of nanocrystals given by the particle-in-a-sphere model. The bulk conduction and valence bands for semiconductors are assumed to be parabolic in the simple effective mass approximation (dotted line). The finite size of the nanocrystal quantizes the allowed k values. Decreasing the nanocrystal diameter shifts the first state to larger values of k and increases the separation between states.

A variety of semiconductor materials have been made in the NC form and studied extensively so far, such as Group IV single-substance semiconductor (Si and Ge), III-V semiconductor compounds (GaAs, GaP, InP), II-VI compounds (CdSe, CdS, ZnSe, CdTe,

PbS), and I-VII compounds (CuCl, CuBr, AgBr). Figure 1-2 listed the range of bandgap alteration for NCs with diameter from 3 to 10 nm. As we can see, the bandgap of NCs can cover the whole visible spectrum and extend to the infrared region just by tuning the NC size.

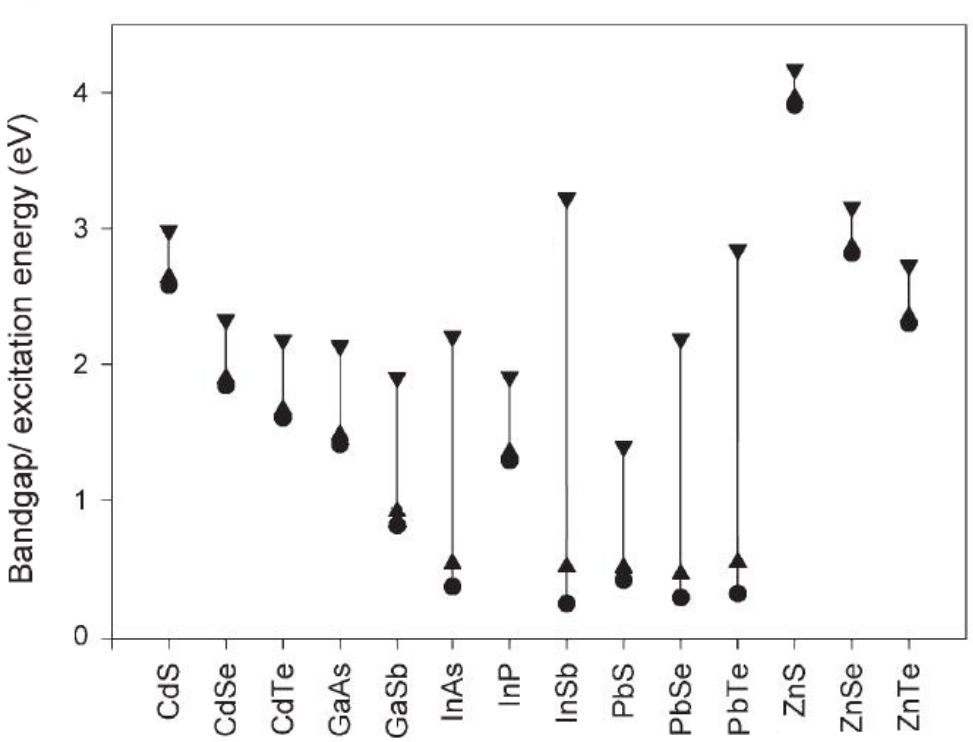

Figure 1-2. Sensitivity of bandgap energies (calculated) to nanocrystal size for a range of semiconductors. Bandgaps are shown for bulk materials (●) and at a nanocrystal diameter of 10 nm (▲)and 3 nm (▼). From ref. 3.

1.1.2 Colloidal Semiconductor Nanocrystals

Semiconductor NCs can be prepared in solid-, liquid-, and gas- phase. Most of the synthesis methods involve thermal reactions of precursors, nucleation, and growth of the nuclei.[4-5] Among these methods, colloidal chemistry synthesis produces samples with best quality, *i.e.* nearly monodisperse, colloidally stable, single crystalline. This synthesizing process is based on the pyrolysis of organometallic reagents by injection into a hot coordinating solvent, which provides temporally discrete nucleation and permits controlled growth of macroscopic quantities of nanocrystallites.[6-7] Size selective precipitation of crystallites from portions of the growth solution isolates samples with narrow size distribution.

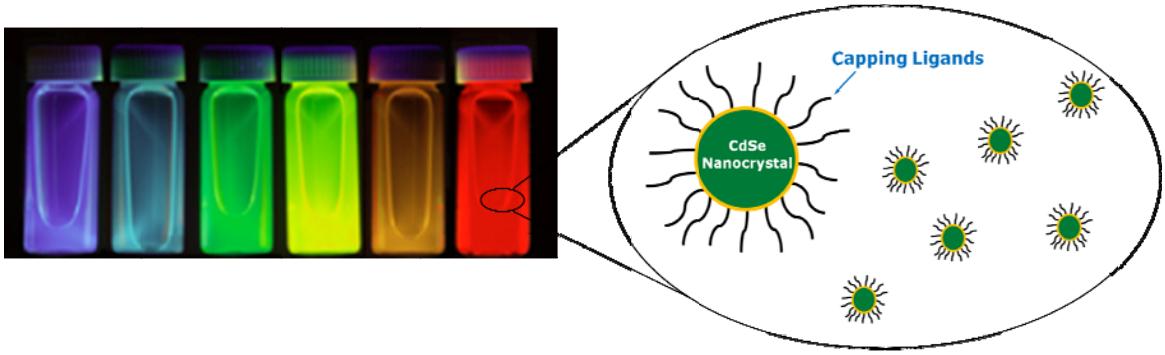

Figure 1-3. Colloidal CdSe nanocrystals dispersed in hexane. Quantum confinement effects allow fluorescent color to be tuned with nanocrystal size under violet illumination (from ref. 8). The enlarged cartoon illustrates the microscopic view of individual nanocrystals capped by long chain ligands.

Bare NCs usually do not fluoresce, as up to half of the atoms are at the surface of the particle, which results in surface defects that can trap charges and catalyze non-radiative

recombination. The NCs made in the aforementioned colloidal chemistry method are capped with the tri-n-octylphosphine oxide (TOPO) and stably dispersed in non-polar solvents.[7] NCs capped with a few atomic monolayers of a higher-gap semiconductor have very high quantum yields.[6, 9] A typical example of this type of core-shell NC is CdSe core with ZnS shell.

1.2 Nanocrystal-based Devices

By taking advantage of the tunable electronic and optical properties discussed in the previous section, semiconductor nanocrystals have been explored to make a variety of electronic and optoelectronic devices, including light-emitting devices (LEDs),[10-12] photodetectors,[13-15] lasers,[16-18] solar cells,[19-23] and field-effect transistors (FETs) . Here, we will briefly review the structure, working principle, and development of LEDs, photodetectors, and FETs based on colloidal NCs.

1.2.1 Light-Emitting Devices (LEDs)

Since the emission colors of colloidal nanocrystals can be easily tuned by their sizes, LEDs using nanocrystals as luminescent centers can cover almost the whole visible range using just one material and the same fabrication procedure. Moreover, the narrow emission band of nanocrystals gives NC-LEDs extra color purity which generates more vivid color images. When nanocrystals with different sizes are mixed properly, the LEDs based on NCs are able to emit white light with higher color rendering index that are more comfortable for human eyes.

The first LED utilizing NCs as emitters was reported by the Alivisatos group in 1994.[12] They used CdSe NCs capped by TOPO-TOP and the emission color could be altered from red to yellow by tuning the NC sizes. Since the NC layer also served as the electron transporting layer, electrons injected into the NCs were imbalanced with the holes from the poly(*p*-phenylenevinylene) (PPV) layer. Thus, the external quantum efficiency, *i.e.* the ratio of the number of photons emitted to the number of carriers injected into the devices, was only 0.001-0.01%. The performance of the NC-LEDs dramatically improved after Coe *et al.* introduced a modified device structure where a single monolayer of NCs was sandwiched between an organic hole-transport layer (HTL) and an electron-transport layer (ETL) (see Figure 1-4).[11] The HTL and ETL pump carriers into the NCs where the carriers are radiatively recombined and photons are subsequently generated. When both HTL and ETL were well optimized, the injection of carriers was balanced resulting in a peak efficiency of about 0.52%.

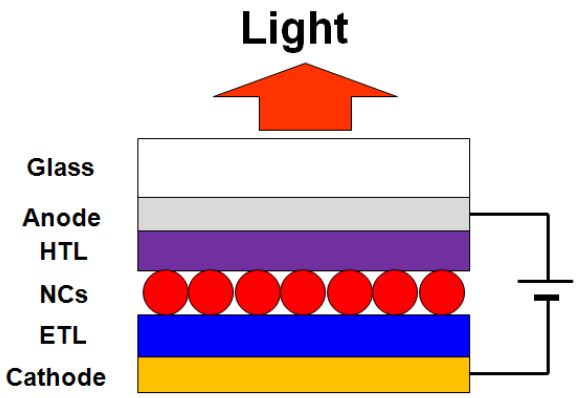

Figure 1-4. Schematic diagram of a typical structure of nanocrystal-based LEDs.

Further modifications and optimizations of NC-LEDs with the sandwich structure have been intensively studied in the past five years. By adding a hole blocking layer between the ETL and NC thin layer, Steckel *et al.* achieved a peak efficiency of 0.5% for low-voltage operation (<10V).[24] Zhao *et al.* utilized thermally polymerized solvent-resistant HTL and reported an efficiency of 0.8%.[25] Sun *et al.* introduced a 25-nm layer of poly(ethylenedioxythiophene):polystyrene sulphonate (PEDOT:PSS) between the anode and HTL in an LED based on CdSe/ZnS core-shell NCs. After optimizing different device parameters, such as the conductive materials in the LED and the thicknesses of the NC layer, they achieved a record efficiency of 2.7%.[26] To date, almost all the best performances of NC-LEDs have been achieved with devices containing NCs of 1–5 monolayers thickness.[27]

Another major challenge of the NC-LEDs aforementioned comes from the organic semiconductor polymers (ETL and HTL), which react to the environment and are unable to support high current densities. This leads to devices that are limited in brightness and degrade in performance under ambient conditions. In 2008, Cargue *et al.* reported the use of sputtered, amorphous alloyed ZnO and SnO_2 as charge transport layers and achieved extended, high-current-density operation.[28] The devices were demonstrated to be capable of operating at current densities exceeding 3.5 A/cm^2 with peak brightness of 1,950 Cd/m^2 and maximum efficiency of nearly 0.1%.[28] Recently, Wood *et al.* successfully made air-stable NC-LEDs with a unipolar device architecture, where the CdSe/ZnS core-shell NCs were sandwiched by two inorganic semiconductor layers.[29] A maximum external quantum efficiency of 0.15% and device life of 40 days were reported.[29]

1.2.2 Photodetectors

There are two major advantages of colloidal NCs for photon detection. Firstly, as aforementioned, the effective band gap of NCs can be tuned by way of the quantum size effect, allowing it to be selected optimally for a given application. Secondly, transport and trap state properties can be separately controlled through the engineering of ligands and the oxidation of NC surfaces either before or after film formation. For example, the NC film conductivity improves significantly when the NCs are cross-linked and/or short ligands are used to cap the NC surfaces.

Figure 1-5 illustrates a typical structure of nanocrystal-based photodetectors. Patterned electrodes made of noble metal (normally Au) are firstly coated on the semiconductor substrate by mask lithography. The spacing between the electrodes are from a few to several hundred microns. A NC film of submicron thick is then deposited between the electrodes atop the substrate. When the electrodes are connected to a voltage supply, a tiny current will be read out from the current meter in Figure 1-5. Once the detector is illuminated, the readout of the current meter will increase since additional mobile charge carriers are generated due to the light.

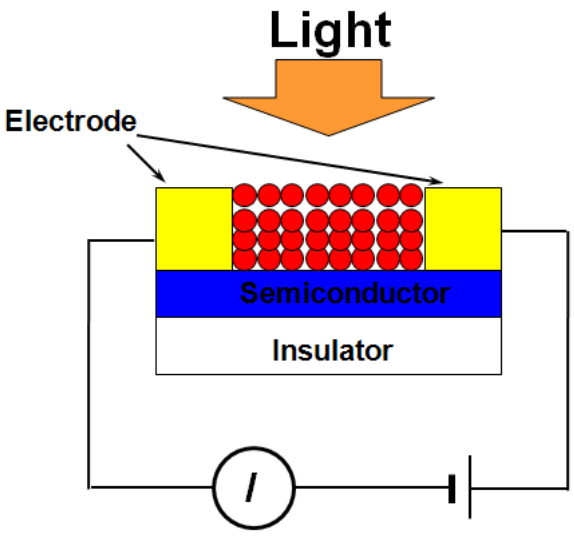

Figure 1-5. Schematic diagram of a typical structure of nanocrystal-based photodetectors.

In 2000, photodetector made from colloidal CdSe NCs working in the visible spectral region was first reported by Leatherdale *et al*.[30] Better performance of the same kind of detectors was achieved by treating the NC films with small molecular linkers like alkylamines.[13, 31] In the near infrared (IR) region where the operation wavelength of optical fibers is located, NCs of narrow bandgap semiconductors, such as InAs and PbS, are strongly competitive compared with other materials, because their band gap can be precisely tuned from about 0.4 eV (~3500 nm) to 3 eV (~413 nm). In 2006, the Sargent group reported highly sensitive IR detectors based on colloidal PbS NCs.[14] It was also found that the trap states due to the defects on the NC surface could be controlled by treating the NCs with different molecules, such as butylamine, formic acid, and short thiols, which consequently shortens the detector response time.[32-33]

1.2.3 Field-Effect Transistors (FETs)

Utilization of colloidal semiconductor NCs as building blocks in FET devices has been explored in the past decade.[34-36] Manufacturing costs of FETs can potentially be decreased, as the solution-based processes offer substantial cost reduction compared with conventional microelectronic fabrication processes, *e.g.* lithography. The FETs can switch between n- and p-type by chemical "activation".[35-36] The electronic and optoelectronic properties of assemblies of NCs can be further understood by studying the performance of the NC-based FETs.

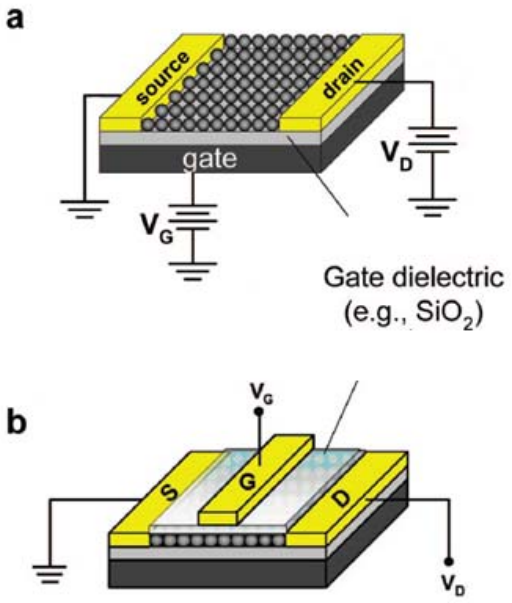

Figure 1-6. Two basic configurations of nanocrystal-based field-effect transistor (FET). (a) Bottom-gated FET, (b) top-gated FET. S, D, and G are the source, drain, and gate electrodes. From ref. 37.

Figure 1-6 illustrates two basic structures of NC-based FETs: bottom-gated and top-gated. The devices include source (S), drain (D), and gate (G) electrodes, all of which connect to the transistor channel. The gate electrode is insulated from the channel by a thin layer of dielectric material (usually SiO_2), which is called a "gate dielectric" as shown in the figure. The thickness of the NCs in the channel is several monolayers. The channel width is usually several microns. Once a bias is applied on the gate, an electric field is created in the channel, which attracts and accumulates carriers with the opposite sign of the channel semiconductor near the gate dielectric. If a voltage is applied between the source and drain electrodes, the additional carriers induced by the gate field either deplete in the channel, or boost the current between the source and drain, depending on the initial type and concentration of the carriers in the transistor channel.

1.3 Printing Techniques of Colloidal Nanocrystals

For the devices discussed in the previous section, the deposition of NC assemblies with controlled thickness and lindwidth is an essential step in the fabrication process. Common methods to deposit large-area thin layers of colloidal NCs include drop casting,[38] spin coating,[39-40] electrophoretic deposition,[41] mist deposition,[27] and contact printing[42]. However, mask screening, lithography, or pre-patterning of the substrate is needed to obtain the patterned NC films with desired width. Thus, direct-write methods such as inkjet printing,[15, 42] e-jet printing,[43] and aerosol jet printing,[44] are attractive because they are capable of writing micropatterns of colloidal nanocrystals without extra

efforts of patterning, thereby simplifying the printing process and allowing inexpensive and rapid prototyping.[45]

1.3.1 Inkjet Printing

Inkjet printing is a pattern deposition technique used for solutions containing a solute dissolved or materials dispersed in a solvent. The inkjet printing process starts with the sudden contraction of a chamber filled with ink in response to a voltage applied due to piezoelectric action. The sudden reduction of chamber volume induces a shockwave in the ink, resulting in an ink drop ejected from a nozzle in the chamber. The ejected drop falls toward a substrate and its trajectory can be deflected in a electric field. After the impingement of the droplet on the substrate, the final print forms after solvent evaporation.

Highly reproducible inkjet printing of colloidal semiconductor NCs in device fabrication was first reported by Böberl *et al.*[15] Photodetectors based on HgTe nanocrystals operating up to 3 μm cut-off wavelength were demonstrated. As shown in Figure 1-7, inkjet printing is successfully employed for the accurate deposition of NCs on electrodes. The ridge-shaped line patterns of NCs deposited are about 1.1 μm thick and 15μm wide. In 2009, Wood *et al.* inkjet printed patterns of nanocrystal-polymer composites to fabricate robust, bright, full-color AC-driven displays.[46]

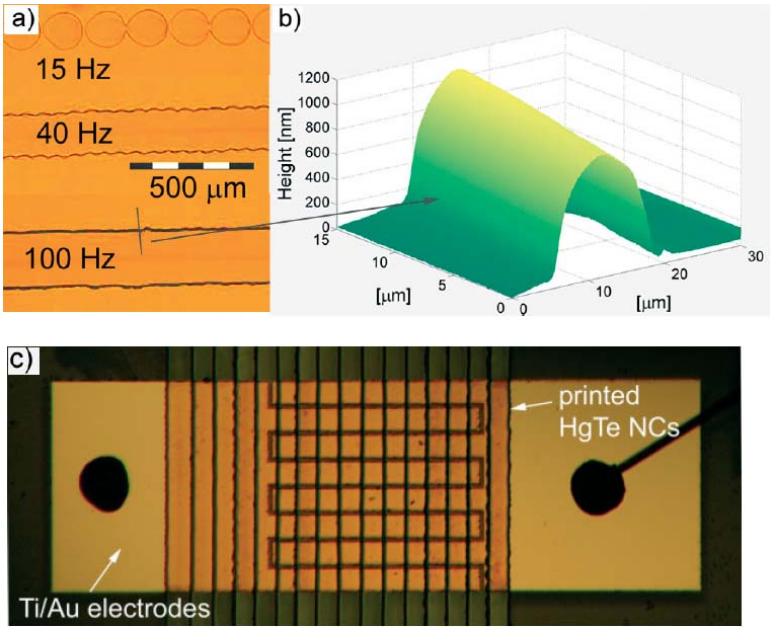

Figure 1-7. (a) Optical image of printed dots and stripes of HgTe nanocrystals on a glass substrate, (b) 3D AFM image of a nanocrystal ridge formed at the perimeter of each printed stripe, and (c) top view optical image of the interdigitated contacts with an array of 16 printed NC stripes. From ref. 15.

Despite the reported successes in depositing patterned colloidal NCs by inkjet printing, there are several challenges in the further progress of inkjet printing colloidal NCs. First, the linewidth of the prints is limited by the drop size ejected from the nozzle, which ultimately depends on jetting conditions, the viscosity and the surface tension of the ink, as well as the nozzle diameter.[47] To obtain a smaller width of the pattern, smaller nozzles are used. However, such nozzles are more expensive and are easier to clog, thereby increasing cost and reducing the reliability and repeatability of inkjet printing. Second, the drying process of the printed droplets on the substrate determines the film morphology and quality. A ring stain of solute that marks the perimeter of the droplet is commonly observed in most of inkjet-printed films, as the outcome of well known

"coffee-ring" effect.[48-49] To solve this issue, a mixture of different solvents was needed to achieve an appropriate evaporation rate.[50] However, this brings complexities in solution stability and change the physical properties of the inks. Furthermore, even using the strategy of mixing solvents, it is hardly to obtain ultrathin films of NCs by inkjet printing, which hinders the application of inkjet printing in the fabrication of NC-based LEDs and FETs where the thickness of the NC film needs to be several monolayers.

1.3.2 Electrohydrodynamic Jet Printing (E-jet Printing)

Electrohydrodynamic jet (e-jet) printing was used to deposit lines consisting of silicon particles or single-walled carbon nanotubes.[43] In this case, high resolution was achieved by liquid jetting driven by an electric field and utilizing fine micro-nozzles. The linewidths of the deposits were approximately equal to the exit diameter of the nozzle. For example, in e-jet printing sub-10-μm features have been deposited using sub-10-μm nozzle tips.[43] However, such fine nozzles can be prone to clogging and can be less durable than larger ones.

Moreover, in the case of e-jet printing or other electrostatic aerosolization methods, adequate electrical conductivity is required to achieve a stable jet mode so as to atomize NC dispersions steadily. Non-polar solvents are poorly conductive, but achieving dispersions of NCs in polar solvents while still maintaining NC fluorescence, is typically achieved after synthesis by further manipulation of the NC surface chemistry, which adds complexity to the process.

1.3.3 Aerosol-based Printing Techniques

To date, two aerosol-based printing techniques have been developed to deposit patterns of NCs — aerosol jet printing and mist deposition. Both methods involve two processing stages. Firstly, the colloidal NCs are transferred from the liquid phase to the gas phase together with the solvents by some aerosolization technique. The NC dispersion then becomes small droplets suspending in the aerosol carrier gas. Secondly, the droplets impinge on the substrate and solvent evaporates. In aerosol jet printing, the droplets are focused by well designed streams of sheath gas before the impingement, resulting in micropatterned deposits of NCs.[44] In mist deposition, no focusing mechanism is applied. Thus, a large-area of uniform thin film of NCs is obtained.[27]

Aerosol jet printers employ a stream of sheath gas in the nozzle to deposit ultrasonically aerosolized droplets (see Figure 1-8a). Using a metallic ink of colloidal Ag nanoparticles, Mette *et al.* successfully used this printing technique in the front side metallization of highly efficient industrial silicon solar cells.[44] With a nozzle exit diameter of 100 μm, linewidths of 14 μm were obtained, indicating focusing (Figure 1-8b). Even finer line widths could be obtained with a 50-μm nozzle. Pang *et al.* utilized an aerosol jet printer to directly write ordered silica nanostructures on arbitrary flat and curved surfaces with a homogenous solution of soluble silica, ethanol, water, and surfactant as a self-assembling ink.[51] However, no ultrathin patterns (monolayers) of NCs fabricated by aerosol jet printing have been reported to date.

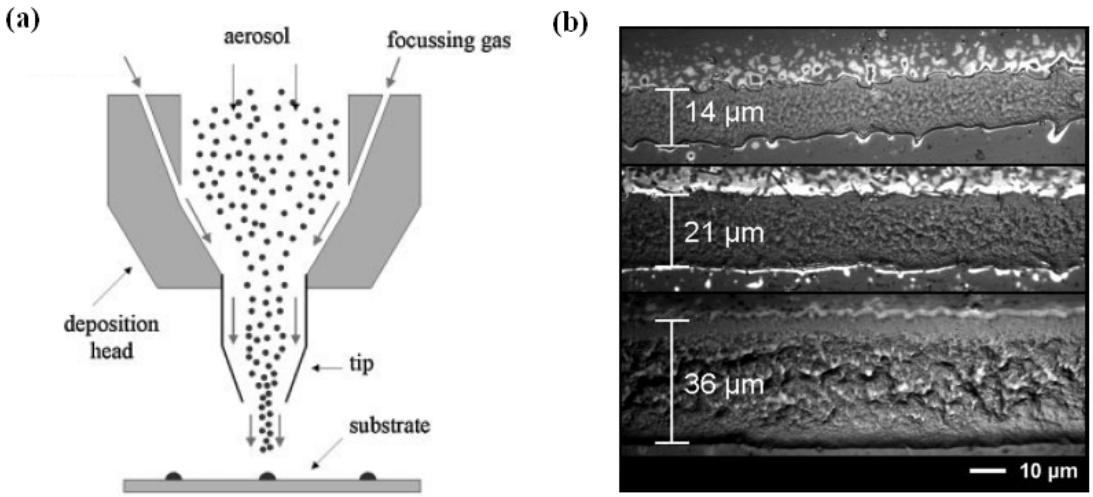

Figure 1-8. (a) Schematic diagram of aerosol jet printer, (b) optical microscope pictures of metal aerosol jet printed lines on glass substrate. From ref. 44.

Mist deposition has been reported to deposit colloidal CdSe NCs with monolayer precision (see Figure 1-9).[27] As toluene was chosen to disperse the NCs, the evaporation of the aerosolized droplets was slow. To avoid the "coffee-ring" effect that occurs in inkjet printing, a series of impactors was employed to remove large droplets in the aerosol. Only droplets containing a few NCs were selected to print on the substrate, which reduces the deposition rate. A 6×6 matrix of alternating pixels composed of 5 nm diameter CdSe NCs (green) and 8 nm diameter CdSe NCs (red) on a glass substrate was successfully fabricated by sequential mist deposition through two optically aligned shadow masks.

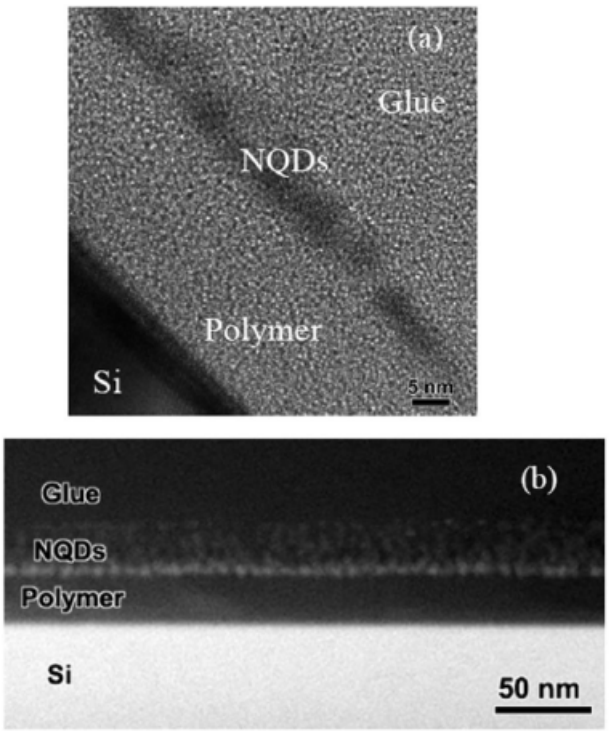

Figure 1-9. Cross-sectional transmission electron microscopy (TEM) images of nanocrystal layers of (a) 1 monolayer and of (b) 5 monolayer deposited over poly(3,4-ethylenedioxythiophene): poly(styrenesulfonate) (PEDOT/PSS)-coated silicon substrates. Above the nanocrystal layer is the glue layer (M-Bond610, Structure Probe, Inc.) used during the preparation of cross-sectional TEM samples. From ref. 27.

1.4 Aerodynamic Focusing

Collimated particle beams have facilitated online particle measurements and nanostructure fabrication for diverse applications such as particle mass spectrometry[52-53] , precise control of nanoparticle beam deposition[54], electron lithography, ion implantation, and so on. Electrically charged particles can be focused with electric and/or magnetic fields. For example, the "ion funnel" described by Smith *et al.* uses radiofrequency fields to focus ions[55]. Focusing neutral particles is more challenging. Aerodynamic focusing is

one option. Supersonic nozzles have been used to focus small particles and molecules but a specific nozzle only focuses particles in a narrow size range[56-57]. Prof. McMurry and co-workers developed aerodynamic lenses to collimate particles covering a wide range of sizes into narrow, collimated beams.

1.4.1 Aerodynamic Lenses

To understand the working principles of aerodynamic lenses, let us start by considering the flow of an aerosol (i.e., a suspension of particles in a gas) through a single thin-plate orifice, as illustrated in Figure 1-10. Due to their inertia, particles deviate from the gas streamlines (shown in blue) as they flow through the orifice. The Stokes number is a dimensionless number that determines the extent of this deviation:

$$St=\tau \cdot v/d_p, \qquad (1\text{-}3)$$

where τ, v, and d_p are the relaxation time, velocity and diameter of the particle, respectively.[58] Very small particles (St<<1) follow the gas streamlines almost perfectly. Very large particles (St>>1) acquire high radial velocities as they converge towards the orifice and impact on the downstream walls of the transport tubing. Particles of intermediate size (St~1), however, have just enough momentum to be transported to the centerline before their radial momentum is dissipated. Particles that move closer to the axis of the flow during transport through the orifice are said to be "aerodynamically focused".

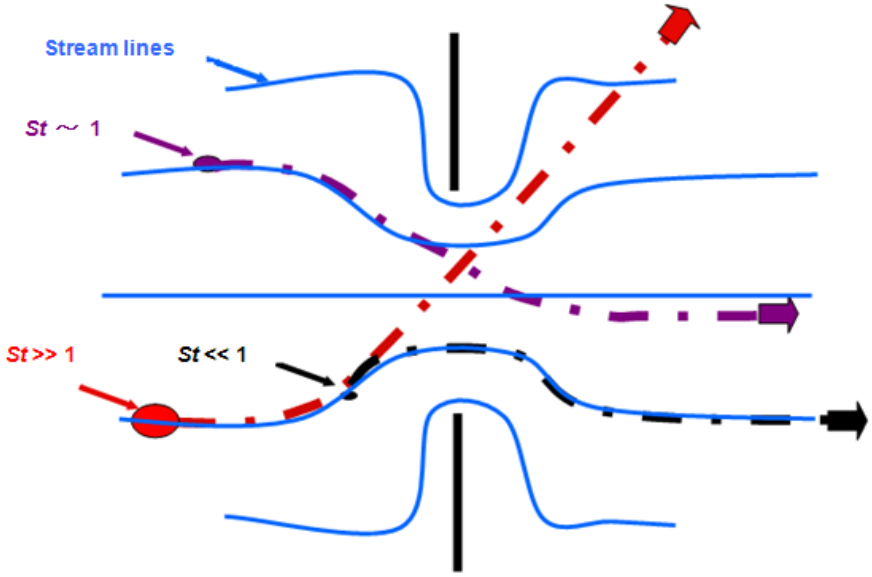

Figure 1-10. Illustration of aerosol particle trajectories through an orifice. Very small particles (black, St << 1) follow the fluid flow while very large ones (red, St >> 1) cannot relax back after the contraction and are lost to the cylinder walls. Particles that undergo "aerodynamic focusing" (purple, St ~ 1) end up on a fluid streamline (blue) closer to the lens axis than before the contraction.

Typically an aerodynamic lens assembly consists of three parts: a flow control orifice, several focusing lenses (thin plate orifices) in series, and an acceleration nozzle as shown in Figure 1-11.[59] First, the choked inlet orifice fixes the mass flow rate through the system and reduces pressure from ambient to the value required to achieve aerodynamic focusing. Second, the flow passes through the series of orifices. When the particle-laden gas passes through the lenses, converging accelerations and diverging decelerations occur for the carrier gas, during which particles having Stokes numbers less than a critical value are separated from the gas due to their inertia and are focused into a tight particle beam. By using multiple lenses in series, tighter focusing can be achieved for a wider range of sizes than is possible for only one lense. Finally, the accelerating nozzle controls the

operating pressure within the lens assembly and accelerates particles to downstream destinations.

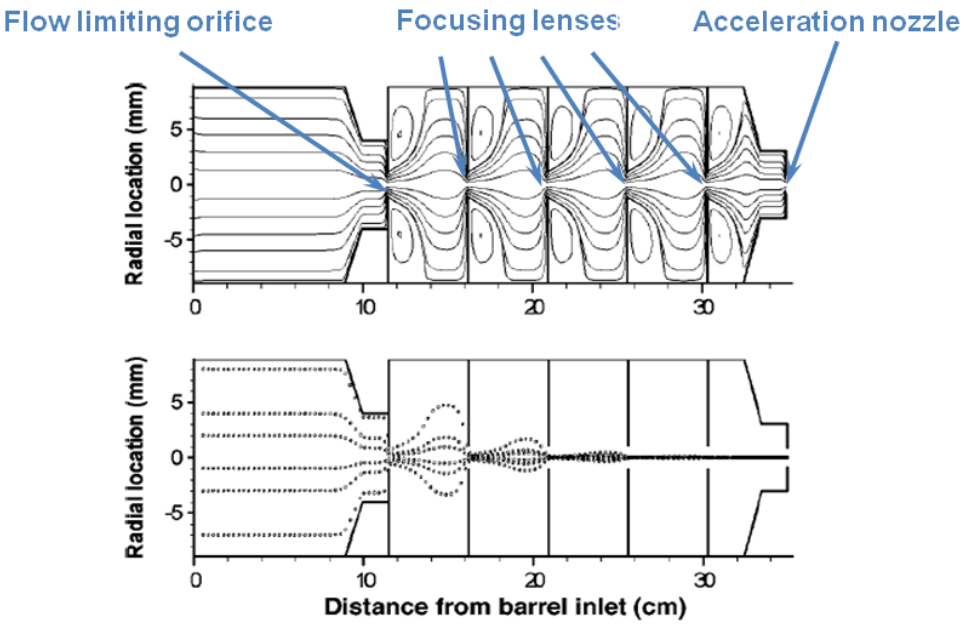

Figure 1-11. Simulated flow streamlines (top) and particle trajectories (bottom) within an aerodynamic lens assembly. From ref. 54.

1.4.2 Design of Aerodynamic Lenses

Aerodynamic lens systems were first designed and analyzed by Liu *et al.*[60-61] They showed that all sampled particles with St<1 can, in principle, be focused onto the axis and that the major effects that limit the minimum beam width are Brownian motion and lift forces on non-spherical particles during the nozzle expansion. An analytical expression for the diffusion-controlled particle beam width downstream of the accelerating nozzle was given by assuming that all particles start from the axis with a frozen Maxwell-Boltzmann radial velocity distribution.

In 2005, Wang *et al.* developed a systematic procedure to design aerodynamic lens systems for nanoparticles.[62] They showed that lighter carrier gases such as helium are preferred for focusing small particles, and developed criteria for optimizing lens dimensions and operating conditions to effectively focus 3-30 nm diameter spherical particles of unit density. Detailed numerical simulations of flow and particle transport were carried out by using the commerical CFD software FLUENT.[59] They also characterized the performance of the lens system experimentally by focusing singly charged oil droplets, sodium chloride particles and protein molecules ranging in mobility diameter from 3 to 30 nm.[63] In their experiment, the particle transport efficiencies were greater than 50% for all particles tested, however the focused particle beam diameters were about three times those predicted by the numerical simulations.

1.4.3 Micropattern Deposition Using Aerodynamic Focusing

Aerodynamic lens systems have been applied by many researchers to focus a variety of particles. In 2000, Di Fonzo et al. designed a lens system to focus SiC particles 10-100 nm in diameter using a mixture of argon and hydrogen as the carrier gas.[54] High-aspect-ratio microtower and microline patterns made of SiC paricles were obtained (see Figure 1-12). In 2003, Gidwani performed a numerical simulation of particle trajectories incorporating Brownian motion.[64] Lee *et al.* focused micron-sized particles at atmospheric pressure using a single lens.[65] In 2004, Dong *et al.* used a lens system to focus 10-200 nm silicon particles in hydrogen.[66]

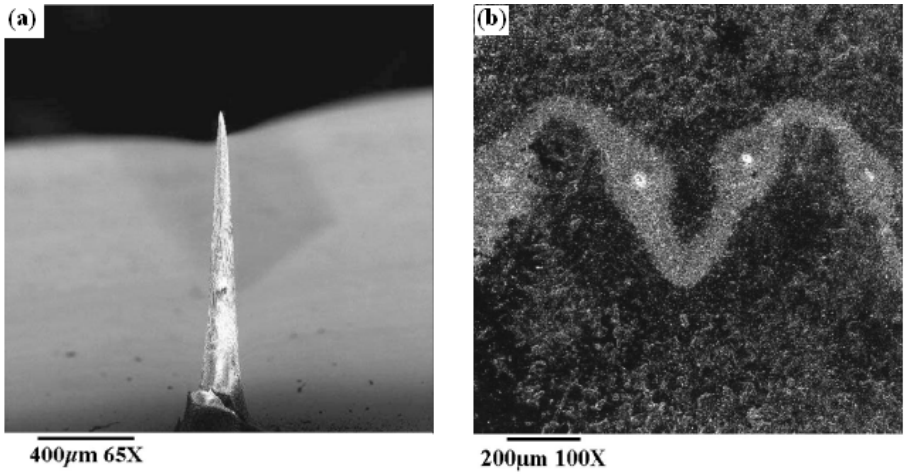

Figure 1-12. Scanning electron micrograph of (a) a "tower" composed of silicon carbide nanoparticles deposited on a stationary substrate, and (b) a zig-zag pattern composed of silicon carbide nanoparticles deposited on a manually translated substrate. From ref.54 .

1.5 Organization of Thesis

Prior to this research no efforts have been made to employ aerodynamic focusing in printing colloidal nanomaterials. Compared with other direct-write methods discussed in section 1.3, the requirement of the low pressure downstream the lens system seems a significant disadvantage of aerodynamic focusing. However, vacuum chambers are widely used in depositing thin metal films, conducting organic films, and oxide layers. As introduced in section 1.2, all these deposits are functioning parts in NC-based devices. An aerodynamic lens assembly can also be readily incorporated into these vacuum systems and take advantage of the pressure drop from ambient to the chamber to deposit the NCs. Moreover, aerodynamic lenses consist of easily manufactured thin metal plates with orifices that are greater than a millimeter in diameter, avoiding the clogging issue of

micro-nozzles used for micropenning and e-jet printing, and reducing the manufacturing cost of the printing apparatus.[43, 67] Finally, designing and evaluating an aerodynamic lens system can be accomplished with a simple Excel-based tool, the Aerodynamic Lens Calculator.[68] Input parameters for the Aerodynamic Lens Calculator include particle properties, carrier gas properties, upstream pressure, aerosol flow rate, the number of lenses, and the deposition chamber pressure. The Calculator can then be used either to design an optimal lens system or to evaluate the performance of an existing lens system. The goal of this research is to apply aerodynamic focusing in printing colloidal nanocrystals and to study the behavior of nanocrystal assemblies during impact deformation.

Starting with a detailed introduction to the colloidal synthesis of CdSe NCs, Chapter 2 summarizes the experimental apparatus and techniques used in this research. Methods used to synthesize and characterize individual NC and NC dispersions in hexane are also included. The chapter ends with details about the home-made nebulizer to atomize the NC dispersion, the aerodynamic lenses deposition system, and the electrostatic precipitator.

Chapter 3 investigates the impact dynamics of aerosolized NC agglomerates. The NC agglomerates were impacted on carbon substrates by either electrostatic precipitation or by impaction from the jet formed by the nozzle in an aerodynamic lens system. Electrostatic precipitation leads to low-speed (1-2 cm/s) impact, while aerodynamic focusing leads to impact at much higher speeds (100-150 m/s). Cohesive and granular behavior of the agglomerates was found by quantitatively comparing the morphologies of deposited agglomerates at these two deposition speeds.

Chapter 4 presents the capability of aerodynamic focusing for printing ultrathin films of colloidal NCs. A single monolayer thickness was achieved by selectively focusing 40-nm NC agglomerates. By printing 100-nm agglomerates, microline NC patterns several monolayers thick were obtained. The effect of surface wettability on the morphology of final prints was also investigated.

Chapter 5 discusses the preparation of thicker NC deposits by aerodynamic focusing without pre-selection of agglomerate sizes. Linewidths below 10 μm at full-width half-maximum were demonstrated. The properties of NCs after high-velocity impact were examined by measuring the fluorescence of the deposited patterns under near UV illumination.

Chapter 6 provides a summary of this thesis research and a list of recommendations for future research.

1.6 References

(1) Brus, L. E., *Journal of Chemical Physics* **1984,** *80*, 4403-4409.

(2) Kanskaya, L. M., Kokhanovskii, S. I., Seisyan, R. P. and Efros, A. L., *Soviet Physics Semiconductors-Ussr* **1982,** *16*, 1315-1317.

(3) Harrison, M. T.; Kershaw, S. V.; Burt, M. G.; Rogach, A. L.; Kornowski, A.; Eychmüller, A.; Weller, H., *Pure and Applied Chemistry* **2000,** *72*, 295-307.

(4) Murray, C. B.; Kagan, C. R.; Bawendi, M. G., *Annual Review of Materials Science* **2000,** *30*, 545-610.

(5) Swihart, M. T., *Current Opinion in Colloid & Interface Science* **2003,** *8*, 127-133.

(6) Reiss, P.; Bleuse, J.; Pron, A., *Nano Letters* **2002,** *2*, 781-784.

(7) Murray, C. B.; Norris, D. J.; Bawendi, M. G., *Journal of the American Chemical Society* **1993,** *115*, 8706-8715.

(8) Frankel, F.; Bawendi, M. G. http://nanocluster.mit.edu/

(9) Hines, M. A.; Guyot-Sionnest, P., *The Journal of Physical Chemistry* **1996,** *100*, 468-471.

(10) Cheng, K.-Y.; Anthony, R.; Kortshagen, U. R.; Holmes, R. J., *Nano Letters* **2010,** *10*, 1154-1157.

(11) Coe, S.; Woo, W.-K.; Bawendi, M.; Bulovic, V., *Nature* **2002,** *420*, 800-803.

(12) Colvin, V. L.; Schlamp, M. C.; Alivisatos, A. P., *Nature* **1994,** *370*, 354-357.

(13) Oertel, D. C.; Bawendi, M. G.; Arango, A. C.; Bulovic, V., *Applied Physics Letters* **2005,** *87*, 213505-3.

(14) Konstantatos, G.; Howard, I.; Fischer, A.; Hoogland, S.; Clifford, J.; Klem, E.; Levina, L.; Sargent, E. H., *Nature* **2006,** *442*, 180-183.

(15) Böberl, M.; Kovalenko, M. V.; Gamerith, S.; List, E. J. W.; Heiss, W., *Advanced Materials* **2007,** *19*, 3574-3578.

(16) Klimov, V. I., *The Journal of Physical Chemistry B* **2006,** *110*, 16827-16845.

(17) Klimov, V. I.; Ivanov, S. A.; Nanda, J.; Achermann, M.; Bezel, I.; McGuire, J. A.; Piryatinski, A., *Nature* **2007,** *447*, 441-446.

(18) Klimov, V. I.; Mikhailovsky, A. A.; Xu, S.; Malko, A.; Hollingsworth, J. A.; Leatherdale, C. A.; Eisler, H.-J.; Bawendi, M. G., *Science* **2000,** *290*, 314-317.

(19) Liu, D.; Kamat, P. V., *The Journal of Physical Chemistry* **1993,** *97*, 10769-10773.

(20) Huynh, W. U.; Dittmer, J. J.; Alivisatos, A. P., *Science* **2002,** *295*, 2425-2427.

(21) Gur, I.; Fromer, N. A.; Geier, M. L.; Alivisatos, A. P., *Science* **2005,** *310*, 462-465.

(22) Robel, I.; Subramanian, V.; Kuno, M.; Kamat, P. V., *Journal of the American Chemical Society* **2006,** *128*, 2385-2393.

(23) Leschkies, K. S.; Divakar, R.; Basu, J.; Enache-Pommer, E.; Boercker, J. E.; Carter, C. B.; Kortshagen, U. R.; Norris, D. J.; Aydil, E. S., *Nano Letters* **2007,** *7*, 1793-1798.

(24) Steckel, J. S.; Snee, P.; Coe-Sullivan, S.; Zimmer, J. P.; Halpert, J. E.; Anikeeva, P.; Kim, L.-A.; Bulovic, V.; Bawendi, M. G., *Angewandte Chemie International Edition* **2006,** *45*, 5796-5799.

(25) Zhao, J.; Bardecker, J. A.; Munro, A. M.; Liu, M. S.; Niu, Y.; Ding, I. K.; Luo, J.; Chen, B.; Jen, A. K. Y.; Ginger, D. S., *Nano Letters* **2006,** *6*, 463-467.

(26) Sun, Q.; Wang, Y. A.; Li, L. S.; Wang, D.; Zhu, T.; Xu, J.; Yang, C.; Li, Y., *Nature Photonics* **2007,** *1*, 717-722.

(27) Zhu, T.; Shanmugasundaram, K.; Price, S. C.; Ruzyllo, J.; Zhang, F.; Xu, J.; Mohney, S. E.; Zhang, Q.; Wang, A. Y., *Applied Physics Letters* **2008,** *92*, 023111.

(28) Caruge, J. M.; Halpert, J. E.; Wood, V.; Bulovic, V.; Bawendi, M. G., *Nature Photonics* **2008,** *2*, 247-250.

(29) Wood, V.; Panzer, M. J.; Caruge, J.-M.; Halpert, J. E.; Bawendi, M. G.; Bulović, V., *Nano Letters* **2009,** *10*, 24-29.

(30) Leatherdale, C. A.; Kagan, C. R.; Morgan, N. Y.; Empedocles, S. A.; Kastner, M. A.; Bawendi, M. G., *Physical Review B* **2000,** *62*, 2669-2680.

(31) Jarosz, M. V.; Porter, V. J.; Fisher, B. R.; Kastner, M. A.; Bawendi, M. G., *Physical Review B* **2004,** *70*, 195327.

(32) Konstantatos, G.; Sargent, E. H., *Applied Physics Letters* **2007,** *91*, 173505-3.

(33) Konstantatos, G.; Levina, L.; Fischer, A.; Sargent, E. H., *Nano Letters* **2008,** *8*, 1446-1450.

(34) Ridley, B. A.; Nivi, B.; Jacobson, J. M., *Science* **1999,** *286*, 746-749.

(35) Talapin, D. V.; Murray, C. B., *Science* **2005,** *310*, 86-89.

(36) Law, M.; Luther, J. M.; Song, Q.; Hughes, B. K.; Perkins, C. L.; Nozik, A. J., *Journal of the American Chemical Society* **2008,** *130*, 5974-5985.

(37) Talapin, D. V.; Lee, J.-S.; Kovalenko, M. V.; Shevchenko, E. V., *Chemical Reviews* **2009,** *110*, 389-458.

(38) Murray, C. B.; Sun, S. H.; Gaschler, W.; Doyle, H.; Betley, T. A.; Kagan, C. R., *IBM Journal of Research and Development* **2001,** *45*, 47-56.

(39) Finlayson, C. E.; Ginger, D. S.; Greenham, N. C., *Applied Physics Letters* **2000,** *77*, 2500-2502.

(40) Snee, P. T.; Chan, Y. H.; Nocera, D. G.; Bawendi, M. G., *Advanced Materials* **2005,** *17*, 1131-1136.

(41) Islam, M. A.; Herman, I. P., *Applied Physics Letters* **2002,** *80*, 3823-3825.

(42) Kim, L.; Anikeeva, P. O.; Coe-Sullivan, S. A.; Steckel, J. S.; Bawendi, M. G.; Bulović, V., *Nano Letters* **2008,** *8*, 4513-4517.

(43) Park, J. U.; Hardy, M.; Kang, S. J.; Barton, K.; Adair, K.; Mukhopadhyay, D. K.; Lee, C. Y.; Strano, M. S.; Alleyne, A. G.; Georgiadis, J. G.; Ferreira, P. M.; Rogers, J. A., *Nature Materials* **2007,** *6*, 782-789.

(44) Mette, A.; Richter, P. L.; Hörteis, M.; Glunz, S. W., *Progress in Photovoltaics: Research and Applications* **2007,** *15*, 621-627.

(45) Chrisey, D. B., *Science* **2000,** *289*, 879-881.

(46) Wood, V.; Panzer, M. J.; Chen, J.; Bradley, M. S.; Halpert, J. E.; Bawendi, M. G.; Bulovi, V.; cacute. *Advanced Materials* **2009,** *21*, 2151-2155.

(47) Singh, M.; Haverinen, H. M.; Dhagat, P.; Jabbour, G. E., *Advanced Materials* **2010,** *22*, 673-685.

(48) Deegan, R. D., *Physical Review E* **2000,** *61*, 475-485.

(49) Deegan, R. D.; Bakajin, O.; Dupont, T. F.; Huber, G.; Nagel, S. R.; Witten, T. A., *Nature* **1997,** *389*, 827-829.

(50) Lim, J. A.; Lee, W. H.; Lee, H. S.; Lee, J. H.; Park, Y. D.; Cho, K., *Advanced Functional Materials* **2008,** *18*, 229-234.

(51) Pang, J.; Stuecker, J. N.; Jiang, Y.; Bhakta, A. J.; Branson, E. D.; Li, P.; III, J. C.; Sutton, D.; Calvert, P.; Brinker, C. J., *Small* **2008,** *4*, 982-989.

(52) Ziemann, P. J.; Liu, P.; Rao, N. P.; Kittelson, D. B.; McMurry, P. H., *Journal of Aerosol Science* **1995,** *26*, 745-756.

(53) Jayne, J. T.; Leard, D. C.; Zhang, X.; Davidovits, P.; Smith, K. A.; Kolb, C. E.; Worsnop, D. R., *Aerosol Science and Technology* **2000,** *33*, 49 - 70.

(54) Di Fonzo, F.; Gidwani, A.; Fan, M. H.; Neumann, D.; Iordanoglou, D. I.; Heberlein, J. V. R.; McMurry, P. H.; Girshick, S. L.; Tymiak, N.; Gerberich, W. W.; Rao, N. P., *Applied Physics Letters* **2000,** *77*, 910-912.

(55) Shaffer, S. A.; Tang, K. Q.; Anderson, G. A.; Prior, D. C.; Udseth, H. R.; Smith, R. D., *Rapid Communications in Mass Spectrometry* **1997,** *11*, 1813-1817.

(56) Fernández-Feria, R., P. Riesco-Chueca, J. Rosell-Llompart, J. Fernández de la Mora, and; O'Brien, J., *Brownian Motion Limited Aerodynamic Focusing of Heavy Molecules*. Weinheim: 1991.

(57) Fernández de la Mora, J., J. Rosell-Llompart, and P. Riesco-Chueca, *Aerodynamic Focusing of Particles and Molecules in Seeded Supersonic Jets*. AIAA: Washington DC, 1989.

(58) Hinds, W. C., *Aerosol Technology- properties, behavior, and measurement of airborne particles*. 2nd ed.; John Wiley & Sons, Inc.: Los Angeles, CA, 1999.

(59) Wang, X. L.; Gidwani, A.; Girshick, S. L.; McMurry, P. H., *Aerosol Science and Technology* **2005,** *39*, 624-636.

(60) Liu, P., Ziemann, P. J.,Kittelson, D. B. and McMurry, P. H., *Aerosol Science and Technology* **1995,** *22*, 293-313.

(61) Liu, P., Ziemann, P. J., Kittelson, D. B. and McMurry, P. H., *Aerosol Science and Technology* **1995,** *22*, 314-324.

(62) Wang, X. L.; Kruis, F. E.; McMurry, P. H., *Aerosol Science and Technology* **2005,** *39*, 611-623.

(63) Wang, X. L.; McMurry, P. H., *International Journal of Mass Spectrometry* **2006,** *258*, 30-36.

(64) Gidwani, A. Studies of Flow and Particle Transport in Hypersonic Plasma Particle Deposition and Aerodynamic Focusing. University of Minnesota, Minneapolis, 2003.

(65) Lee, J.-W., M.-Y. Yi, and S.-M. Lee. *Journal of Aerosol Science* **2003,** *34*, 211-234.

(66) Dong, Y., A. Bapat, S. Hilchie, U. Kortshagen, and S. A. Campbell. *Journal of Vacuum Science and Technology B* **2004,** *22*, 1923-1930.

(67) Suzuki, T.; Imazeki, N.; G. Yu, H. I.; Oda, M., Direct Drawing System with Micro-Dispenser Using Dispersed Ultra Fine Particle Paste. In *IEMT/IMC Symposium, 1st Joint International Electronic Manufacturing Symposium and the International Microelectronics Conference*, 1997; pp 267-270.

(68) Wang, X. L.; McMurry, P. H., *Aerosol Science and Technology* **2006,** *40*, 320-334.

2

Experimental Methods

This chapter focuses on the experimental methods and techniques utilized in this thesis research. The details about the colloidal NC synthesis and characterization are first discussed. The aerosolization of synthesized NCs and subsequent characterization are then presented. The experimental setups of the two methods to deposit aerosolized NCs used in this study are finally introduced.

2.1 Nanocrystal Synthesis

The CdSe nanocrystals (NCs) are synthesized in a mixed TOPO/hexadecylamine (HDA) solvent with a molar ratio of 60-80% HDA and using CdO complexed with dodecylphosphonic acid as the cadmium precursor.[1-2] The experimental setup is depicted in Figure 2-1 and the synthesis is done in a fumehood. A precursor mixture of CdO (Strem, 0.051g), dodecylphosphonic acid (DDPA) (PCI Synthesis, 0.201g),

hexadecylamine (HDA) (Aldrich, 2.2g), and TOPO (Aldrich, 1.056g) were heated up to 90°C in a three-neck round bottom flask. The flask was evacuated to 50 milli-torr and purged with dry nitrogen gas. The degassing and nitrogen purging were repeated three to four times before the final pressure in the flask was below 25 milli-torr. Under nitrogen atmosphere, the mixture was further heated to 270-300° C and was held at that temperature until the solution turned from brown to colorless. A solution of selenium (Alfa Aesar, 0.5 mmol) in trioctylphosphine (TOP) (Aldrich, 2 mL) was then rapidly injected into the flask. The temperature of the reaction solution was stabilized at 250 °C to keep NC growing upon injection. Once per minute, 0.1 mL of the colloidal solution was transferred to a two-side-polished cuvette (Spectrocell) and diluted with hexane. The absorption spectra of the diluted solutions were measured to track the NC growth. Once the desired size was obtained, the heat source was removed from the flask and NCs stopped growing. Absolute ethanol was added into the colloidal solution to precipitate out the NCs. After the solution was removed, the precipitates were dried and redispersed in hexane. The precipitation and redispersion were repeated three times to remove the excess capping groups. The colloidal solution was cooled down in a refrigerator (-20°C) for 20 minutes and quickly filtered through a PTFE filter (0.1 μm). The CdSe NCs dispersion in hexane was finally transferred into a glass vial, which was stored in the dark before thin shell coating or aerosolization.

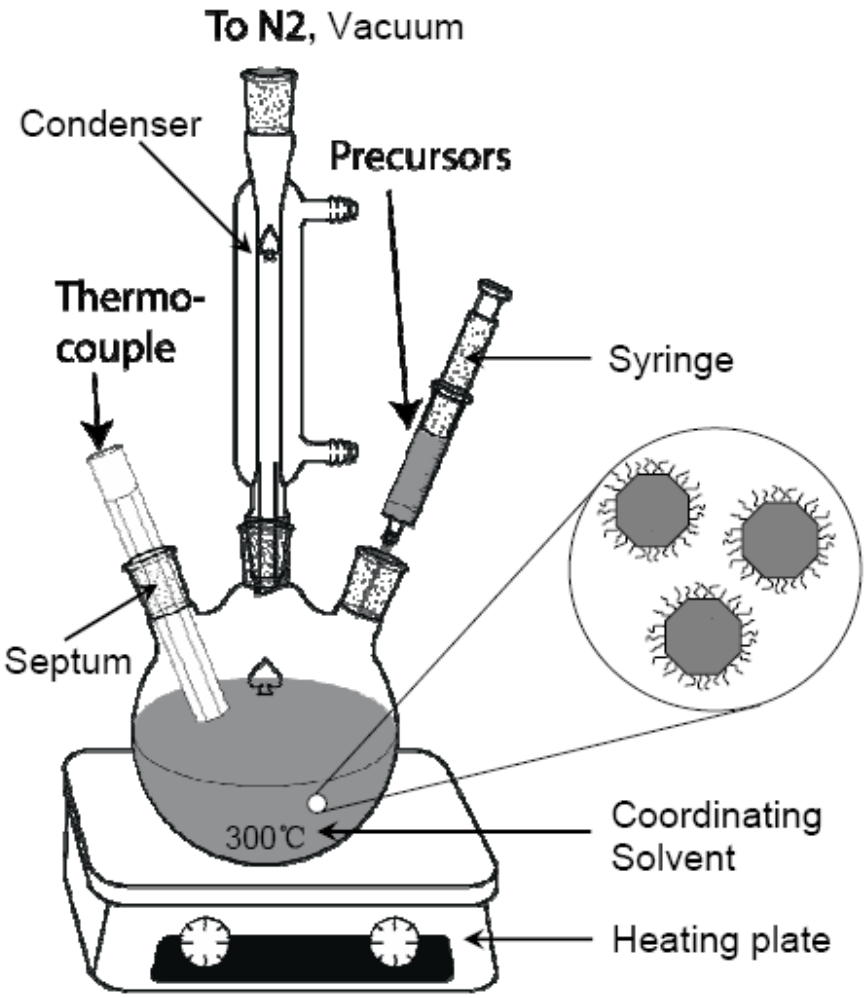

Figure 2-1. Schematic diagram of the experimental setup of NC synthesis from ref. 3. NCs are synthesized by rapidly injecting organometallic precursors into a hot coordinating solvent. The cartoon in the figure shows several individual NCs. The NC surfaces are passivated by surfactants.

One more hot injection synthesis was required to coat a thin ZnS shell on the synthesized CdSe NCs.[4] Roughly 0.3 μmol of CdSe NCs dispersion was placed into a three-neck round bottom flask via syringe and dried. 2.5 g HDA and 5 g TOPO were added into the flask and the mixture was heated to 90°C. The flask was degassed and

purged with dry nitrogen gas three times. The reaction solution was then heated up to ~250°C under nitrogen and the solution turned red and clear. A solution of diethylzinc (Strem, 40 μL) in 3 mL TOP was loaded into a syringe inside a nitrogen glove box. The syringe was then moved out of the glove box and hexamethyldisilathiane (Aldrich, 107 μL) was added into the syringe in the fumehood. The Zn and S precursor solution was injected dropwise into the reaction vessel which was maintained at ~220°C. The reaction lasted 5 minutes and was terminated by removing the heat source. The excess capping surfactants in the colloidal solution were removed by following the same procedure used to synthesize the CdSe core NCs. The CdSe/ZnS core/shell NC dispersion in hexane was finally stored in a glass vial in the dark before it was nebulized.

2.2 Colloidal Nanocrystal Characterization

Properties of synthesized NCs were characterized by optical spectroscopic measurement. Important information, such as NC size, bandgap, as well as NC number concentration in dispersion, were collected. Transmission electron microscopy (TEM) was employed to determine the morphology and size of individual NCs.

2.2.1 Optical Spectroscopy

Figure 2-2 shows the absorption and photoluminescence (PL) spectra of bare CdSe and CdSe/ZnS core-shell NCs in hexane. The NC dispersion is stored in a 1 cm path length cuvette (Spectrocell). Optical absorption spectra were obtained by a UV-Vis spectrometer (SD 200, Ocean Optics). Photoluminescence spectra were measured by a

spectrofluorometer (Fluorolog-2, SPEX) with two monochromators (double-grating, 0.22m, SPEX 1680) and a 450W Xenon lamp as the excitation source. The absorption peak and the PL peak of the pure CdSe NCs were found at 537 nm and 545 nm, while the corresponding peaks for CdSe/ZnS NCs were found at 546 nm and 558 nm (see Figure 2-2). The red shift of both the absorption and PL peaks indicates that a ZnS shell was successfully coated on the surface of synthesized CdSe NCs.[4]

The size of CdSe NCs can be calculated from the peak wavelength of the absorption spectrum. Using the empirical equation reported by Yu *et al.*,[5] we found that the diameter of the CdSe NCs with the absorption peak of 537 nm was 2.8 nm. The number concentration of CdSe NC dispersion in hexane can also be extracted from the absorption spectrum. According to Beer-Lambert law, the absorbance of a dilute dispersion follows:[6]

$$A_\lambda = \varepsilon_\lambda \cdot c \cdot l \qquad (2\text{-}1)$$

where A_λ is the absorbance at wavelength λ, ε_λ is the molar absorptivity ($M^{-1}cm^{-1}$) at wavelength λ, c is the molar concentration of the dispersion (M), and l is the path length (cm). Meanwhile, the relationship between C_{abs}, the effective absorption cross-section of an individual NC (cm^2), and the molar absorptivity is

$$C_{abs,\lambda} = \frac{2303 \cdot \varepsilon_\lambda}{N_A} \qquad (2\text{-}2)$$

where N_A is the Avogadro's number.

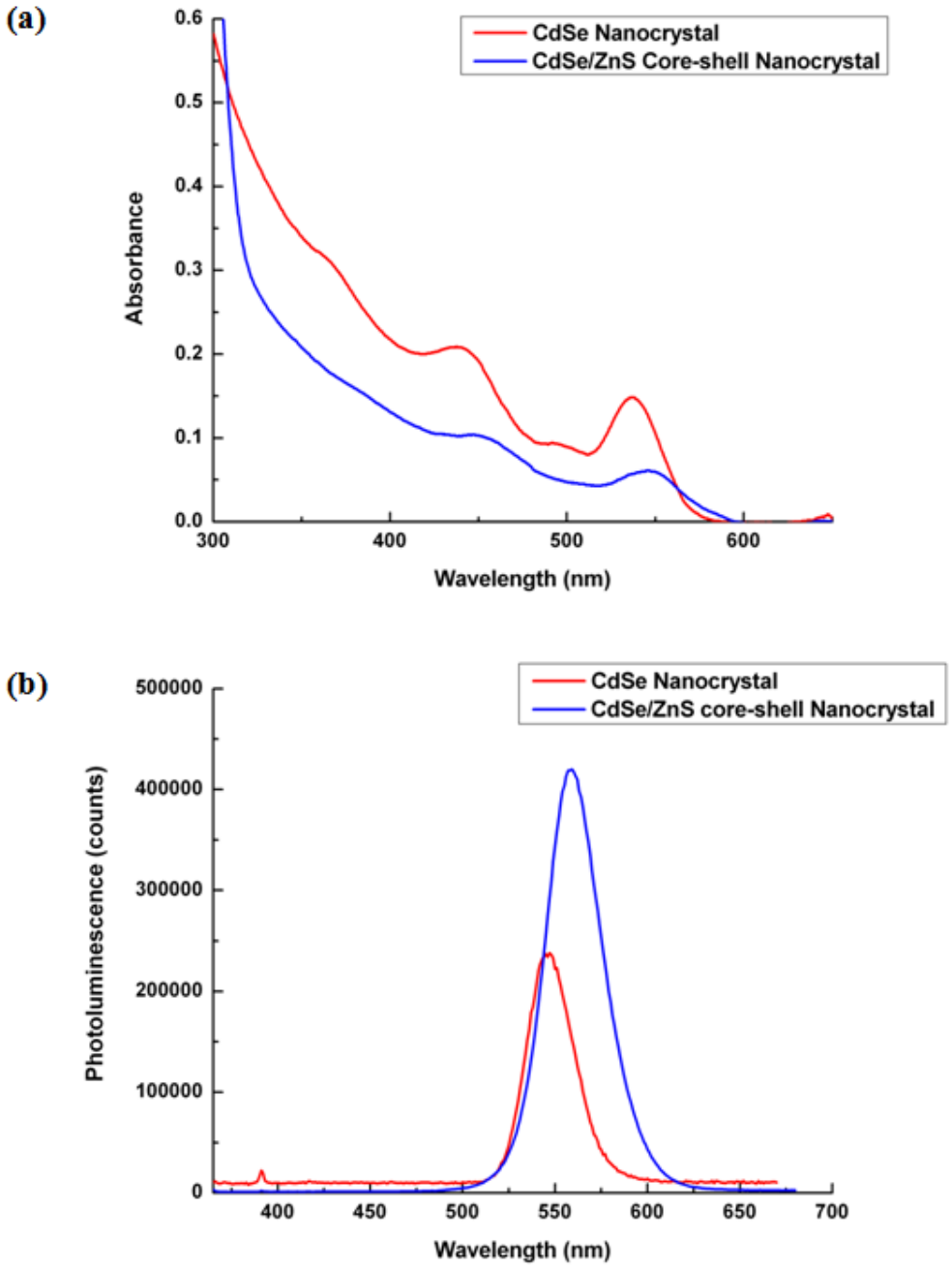

Figure 2-2. (a) Absorption (Abs) and (b) Photoluminescence (PL) spectra of CdSe and CdSe/ZnS core-shell NCs. The excitation light wavelength of PL measurement was 340 nm. The PL spectrum of CdSe NCs has been amplified by 10 times.

Combining equations 2.1 and 2.2, the molar concentration can be calculated by

$$c = \frac{2303 \cdot A_\lambda}{N_A \cdot C_{abs,\lambda} \cdot l} . \qquad (2\text{-}3)$$

For CdSe NC dispersions in hexane, Leatherdale *et al.* measured the C_{abs} at 350 nm for different NC sizes (see Figure 2-3).[7] C_{abs} can then be obtained from the curve in Figure 2-3, once the NC size is known from the absorption peak. The absorbance at 350 nm can be easily determined from the absorption spectrum. Thus, the molar concentration of the CdSe NC dispersion can be calculated by equation 2.3.

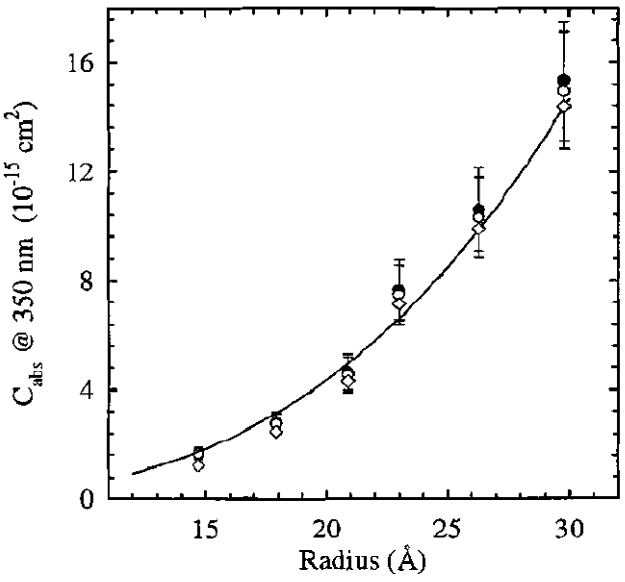

Figure 2-3. Absorption cross section of an individual CdSe NC (C_{abs}) at 350 nm as a function of size for CdSe NCs dispersed in hexane from ref. 7.

The NC number concentration n (NCs/cm^3) can be obtained from the molar concentration, N_A, using Equation 2.4:

$$n = \frac{c \cdot N_A}{10^3} = \frac{2.303 \cdot A_{350}}{C_{abs,350} \cdot l} \,. \qquad (2\text{-}4)$$

As a dilute dispersion is required by the Beer-Lambert law, the synthesized and cleaned CdSe NC dispersion was diluted by a factor of 20-30 before the absorption measurement.

2.2.2 Transmission Electron Microscopy (TEM)

TEM images were acquired by a field-emission gun transmission electron microscope (G2 F30, Tecnai) with an operating voltage at 300 kV. To characterize the size and morphology of the synthesized NCs, a dilute NC dispersion in hexane was prepared and drop cast onto carbon-film-coated copper grids (300 mesh, Ted Pella). After fast evaporation of hexane, the droplet was dried, resulting in scattered NC islands of a single monolayer. Figure 2-4 is a typical TEM image of synthesized CdSe NCs from deposits prepared in this manner.

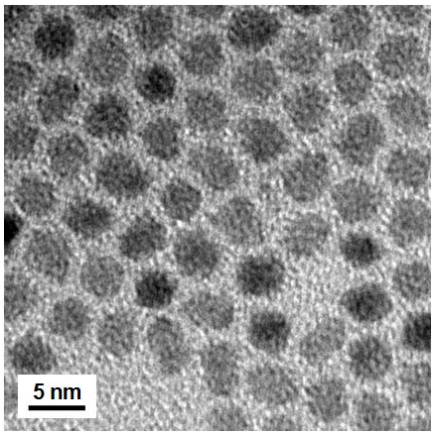

Figure 2-4. TEM image of synthesized CdSe NCs. The average diameter is ~ 3.6 nm.

2.3 Nanocrystal Aerosolization and Characterization

The NCs need to be transferred from solution to the gas phase before printing, which is called aerosolization or atomization. Two methods have been tried to aerosolize the synthesized NC dispersion: electrospray and pneumatic nebulization. It turned out that the latter method was easier to operate and efficient. During nebulization, solution droplets that contained multiple NCs were produced. When the solvent evaporated, particles that contained a mixture of the organic capping ligands and the nanocrystalline cores remained. We refer to these as "nanocrystal solids" or "quantum dot solids." *In situ* measurements of mobility distributions were carried out on the quantum dot solids. Also, the masses of mobility classified particles were measured.

2.3.1 Colloidal Nanocrystal Aerolization

Electrospray was first attempted to atomize NC dispersions. An electrospray aerosol generator (TSI, Model 3480) was used in these experiments. This instrument produces high concentrations of monodisperse, submicrometer aerosol particles from 2 to 100 nm. Like e-jet printing, electrospray also requires that the conductivity of solution is high enough to form a steady cone-shaped jetting mode in an applied electrical field. However, the NC dispersions in nonpolar solvents were not conductive. To increase the electrical conductivity of these solutions, NCs needed to be stably dispersed in polar solvents such as methanol or water, which was successfully completed through ligand exchange. By switching the capping group on CdSe NCs to short thiols, NCs were stably dispersed in methanol and water.[8] However, this exchange led to a decrease in the luminescent yield of the CdSe NCs. Therefore, a thin shell of ZnS was applied to the CdSe cores. Nevertheless, the conductivity of pure methanol or pure water was still not high enough

to maintain a stable cone-jet mode for electrospray. Extra efforts were made to further increase the conductivity. Electrolytes like sodium chloride and ammonium acetate were added to the solution, but we found that a tiny amount of electrolyte was enough to precipitate the NCs out of the solution. Acids or alkali were also tried, and the dispersion became unstable as the colloidal stability of NCs was also sensitive to the solution PH values.

Because of the difficulties encountered when electrospraying the NC dispersions, pneumatic nebulization was usede instead. This is the approach that is most commonly used to aerosolize solutions.[9] Compared with electrospray, nebulization generates polydisperse aerosol particles but has no requirements for the dispersion conductivity. A home-made pneumatic nebulizer (Collison atomizer) was used to atomize the NC dispersions in non-polar solvents (see Figure 2-5). Carrier gas (helium or air) was dried, filtered, and then injected into the nebulizer at a pressure of 240 kPa. A plastic capillary tube drew the solution from the NC dispersion reservoir up to the spray chamber, where the dispersion was sheared into droplets with an average diameter of ~3 μm. An impactor removed large droplets, to ensure that the atomized agglomerates were small enough for our work. Hexane solvent quickly evaporated when the aerosol flowed through an activated carbon denuder after nebulization, although toluene did not. The nebulized aerosol particles are all charged, due to friction between the organic solvents and the metallic nozzle of the nebulizer (*Static Electrification*).[10]

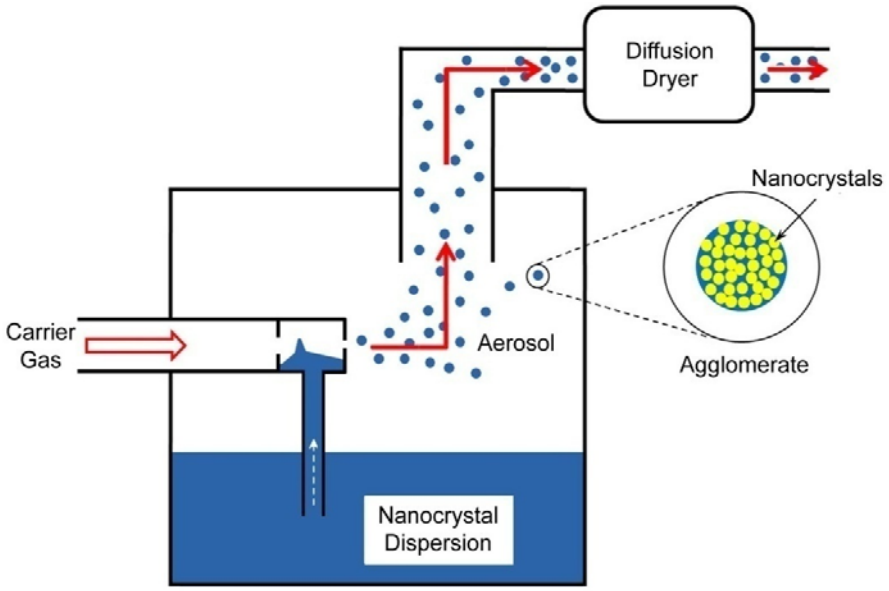

Figure 2-5. Schematic illustration of NC aerosolization from ref. 11. Red lines indicate the direction of gas flow. Dry helium gas is injected as a carrier gas into a home-made nebulizer. Aerosol droplets are created from a dispersion of CdSe NCs in hexane. Evaporated hexane vapor is removed by a diffusion dryer containing freshly activated carbon powders.

2.3.2 Aerosol Characterization

Two types of tandem measurements were conducted to characterize the properties of aerosolized NCs. The mobility size distribution was measured with a scanning mobility particle analyzer (SMPS).[12-13] The mass and morphology of aerosolized particles were characterized by the mass-size measurements.[14-15]

2.3.2.1 Scanning Mobility Particle Analyzer (SMPS)

The SMPS system includes a differential mobility analyzer (DMA) and a condensation particle counter (CPC). Prior to the measurement, the aerosol particles were

passed through a bipolar neutralizer using a radioactive source (Po-210) to ensure no more than a single charge per particle. The flow schematics of the aerosol within a DMA are shown in Figure 2-6. Aerosol enters the DMA as a thin annular stream at the periphery of a laminar flow of clean dry air between two concentric metallic cylinders. The external cylinder is grounded. Only the aerosol particles with the desired mobility size, which is determined by the voltage applied on the internal cylinder, exit from the outlet.

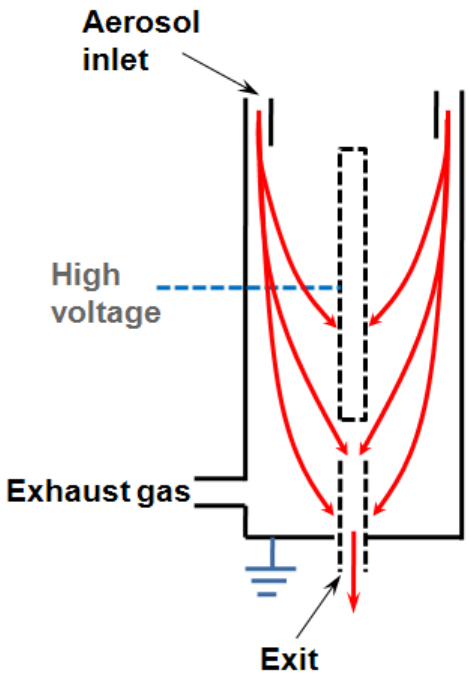

Figure 2-6. Schematic illustration of a differential mobility analyzer (DMA). Red arrows indicate the trajectories of aerosol particles inside DMA.

The monodisperse aerosol selected by the DMA is then fed into a CPC (Model 3025A, TSI),[16] which saturates the monodisperse aerosol with 1-butanol vapor and then cools it by conduction as it flows through a cold condenser tube to create the level of super-saturation required for growth. All aerosol particles grow to droplets about 10 μm in diameter regardless of their initial sizes. Finally, the number concentration of droplets, or the concentration of aerosol particles with the mobility size selected by DMA, is determined by counting pulses of light scattered from individual particles downstream of the condenser. By continuously changing the high voltage applied on the DMA, the number concentration of aerosol particles within the corresponding mobility size range can be obtained. A typical size distribution of nebulized NCs was shown in Figure 2-7, which peaks at 35 nm. The peak diameter increases when the number concentration of the NC dispersion increases.

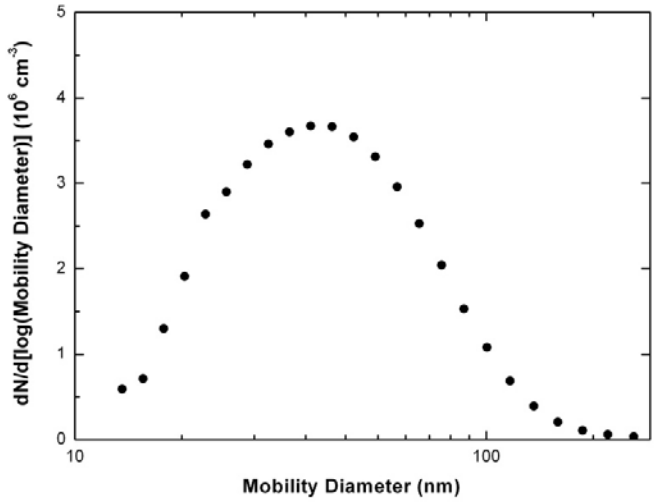

Figure 2-7. A typical size distribution of aerosolized NCs measured by a SMPS system. From ref. 11.

2.3.2.2 Aerosol Particle Mass Analyzer (APM)

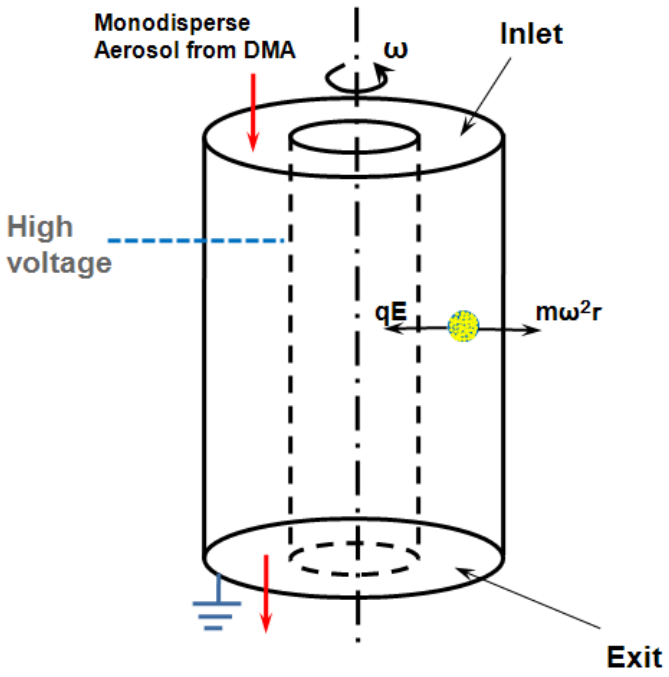

Figure 2-8. Schematic illustration of aerosol particle mass analyzer (APM). Red arrows indicate the direction of aerosol flow when the electrical force is balanced with the centrifugal force.

An aerosol particle mass analyzer (APM, Kanomax Japan Inc.)[17] was used to measure the mass of the monodisperse aerosol particles from the DMA. An APM consists of two concentric thin metal cylinders as illustrated by Figure 2-8. The outer cylinder is grounded and a high voltage is applied to the inner cylinder, creating a radial electrical field across the annular gap between the two cylinders. Meanwhile, the monodisperse and charged aerosol particles are introduced into the gap and rotate at the same as the cylinders. Only when the electrical force on the particles is balanced with the centrifugal force, the aerosol particles can pass through APM and then be detected by a CPC located

downstream (see Figure 2-8). The mass of the particles can then be calculated from first principles.[18] The details about data analysis of DMA-APM tandem measurement were discussed by Emery [19]. The results of the size distribution and mass measurements for aerosolized NCs will be presented and analyzed in Chapter 3.

2.4 Deposition Methods of Aerosolized Nanocrystals

Two different methods were employed to deposit aerosolized NCs: electrostatic precipitation and aerodynamic focusing deposition. In this section, the working principles and experimental setups of both of the deposition methods will be introduced.

2.4.1 Electrostatic Precipitator (ESP)

The electrostatic precipitator consists of two flat plate electrodes as depicted in Figure 2-9. The spacing between two copper electrodes is 1 cm. One electrode is grounded and the other is connected with a high voltage supply (2000-2500 V), resulting in an electrical field between the electrodes normal to the direction of the aerosol flow. A plastic tee (PFA Fittings, Swagelok®) was used to accommodate the electrodes and aerosol flow. Charged particles suspending in the carrier gas experience the electrical field and drift towards one of the electrodes at a steady velocity determined by the balance between the electrical and aerodynamic drag forces.[20] The substrate (*e.g.* TEM grids) was attached to one of the electrodes by a piece of double sided adhesive conductive carbon tape, to collect the particles. Aerosol particles that were not collected by the ESP were removed by a HEPA filter (HEPA Capsule, Gelman Laboratory). During sample collection, the system was connected to the house vacuum line and a

critical orifice (~ 38 μm diameter) set the flow rate to ~1.22 L/min (air). The collection usually took 2-10 minutes.

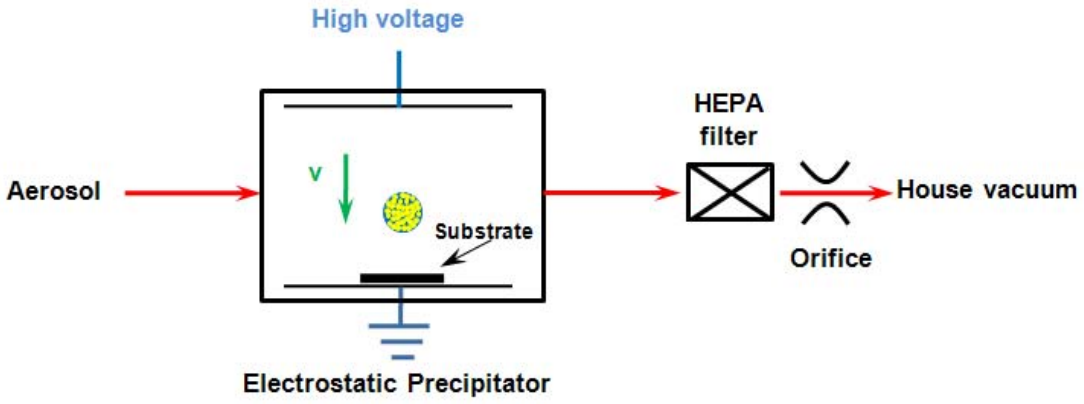

Figure 2-9. Experimental setup schematic of aerosol deposition using electrostatic precipitator (ESP). Red arrows indicate the direction of aerosol flow. The aerosol particle inside the ESP is positively charged and drifts downward to the grounded electrode.

2.4.2 Aerodynamic Focused Beam Deposition System

The aerosol deposition system with aerodynamic lenses is composed of three parts: the aerodynamic lens assembly, the vacuum subsystem, and the substrate translation subsystem.[21] Figure 2-10 is a photograph of this deposition system.

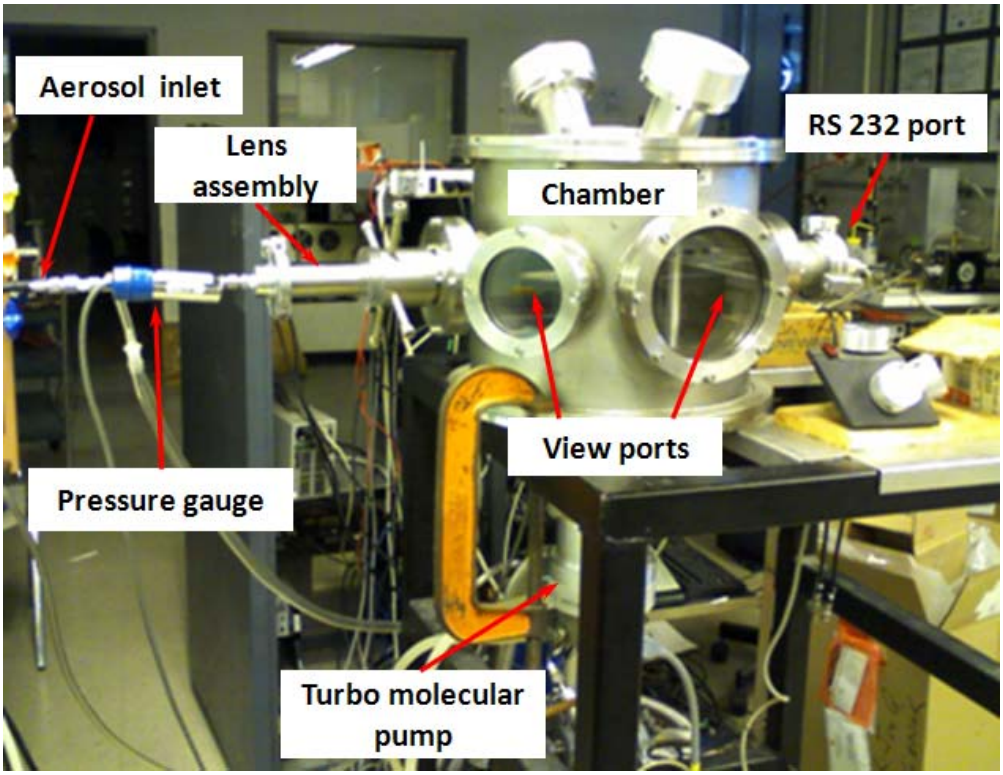

Figure 2-10. Side-view photograph of the aerosol deposition system with aerodynamic lenses.

The schematic of the aerodynamic lenses utilized in this study is shown in Figure 2-11. Each lens is a 0.3 mm thick stainless steel plate with an orifice diameter of 2.26 mm. The lense assembly consists of five such lenses placed at 47 mm intervals. The exit nozzle has an inner diameter of 1.85 mm, which opens into the deposition chamber. An orifice (200 μm in diameter) is usually placed upstream the first lens to limit the aerosol flow rate and to control the pressure within the lenses to achieve conditions that are conducive to focusing. A pressure transducer (Convectron Gauge, Granville-Philips) is placed between the orifice and the lens assembly to measure at the inlet to the first focusing lens (see "Pressure gauge" in Figure 2-10).

The stainless steel deposition chamber is ~ 30.6 cm in diameter and ~ 35.6 cm in height, and it can be opened from the top flange. Altogether there are six ports on the chamber body. The aerodynamic lens assembly is sealed into the chamber by a system of double o-rings. A turbomolecular pump (Model TMH 260, Pfeiffer Vacuum) is connected to the chamber through a central port at the bottom. A mechanical roughing pump (Model CMP-19, NAVCO) is connected to the turbo pump via a valve. The exhaust of the pumping system is filtered and is connected to a fume hood. Two viewports on the side of the chamber were used for observation and for a sample switch. A pressure transducer (Convectron Gauge, Granville-Philips) is connected to the chamber through a port to monitor the chamber pressure. The sixth port was used to house the RS-232 type connection for the substrate translation system.

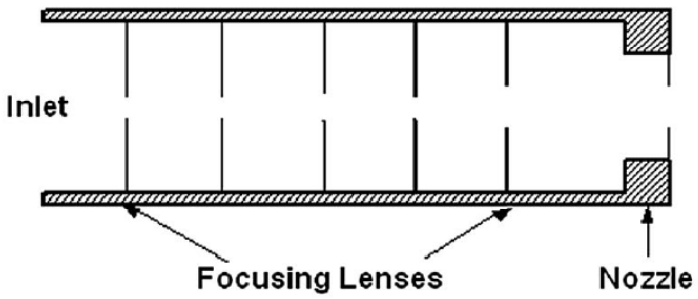

Figure 2-11. Schematic of aerodynamic lens assembly from ref. 21 (not to scale). Each focusing lens is a 2.26 mm diameter orifice and the nozzle is 1.85 mm in diameter. Lens separation is 47 mm.

A 3-axis computer controlled motor system (MP-285, Sutter Instruments) was used to translate the deposition substrate. The stepper motors drive the 3-axes with a step

length of 0.2 μm over a range of 25 mm. The motors are intentionally designed to be non-lubricated and to be suitable for the vacuum systems. An external controller communicates with the motors using a RS-232 cable. A dovetailed substrate holder is designed to easily mount on the motor stage and accommodate different substrates, such as glass slides, silicon wafers, and TEM grids. Before each deposition, a diode laser (670 nm, Melles Griot) is attached to the inlet of the lens system via a Kwik-flange coupling. The deposition position is then illuminated by the laser beam and can be adjusted accordingly through the motor controller.

2.5 References

(1) Peng, Z. A.; Peng, X. G., *Journal of the American Chemical Society* **2001,** *123*, 183-184.

(2) Peter Reiss, J. B., and Adam Pron. *Nano Letters* **2002,** *2*, 781-784.

(3) Zu, L. Doping Semiconductor Nanocrystals. University of Minnesota, Minneapolis, 2006

(4) Hines, M. A.; Guyot-Sionnest, P., *The Journal of Physical Chemistry* **1996,** *100*, 468-471.

(5) Yu, W. W.; Qu, L. H.; Guo, W. Z.; Peng, X. G., *Chemistry of Materials* **2003,** *15*, 2854-2860.

(6) Lakowicz, J. R., *Principles of Fluorescence Spectroscopy* 3rd ed.; Springer Science+Business Media, LLC: New York, NY, USA, 2006.

(7) Leatherdale, C. A.; Woo, W. K.; Mikulec, F. V.; Bawendi, M. G., *The Journal of Physical Chemistry B* **2002,** *106*, 7619-7622.

(8) Aldana, J.; Wang, Y. A.; Peng, X., *Journal of the American Chemical Society* **2001,** *123*, 8844-8850.

(9) Bayvel, L. P.; Orzechowski, Z., *Liquid Atomization*. Taylor & Francis: Washington D.C., USA, 1993.

(10) Loeb, L. B., *Static Electrification* Springer-Verlag: Berlin, Germany, 1958.

(11) Qi, L.; McMurry, P. H.; Norris, D. J.; Girshick, S. L., *Aerosol Science and Technology* **2010,** *44*, 55 - 60.

(12) Wang, S. C.; Flagan, R. C., *Aerosol Science and Technology* **1990,** *13*, 230-240.

(13) McMurry, P. H., *Atmospheric Environment* **2000,** *34*, 1959-1999.

(14) Park, K.; Cao, F.; Kittelson, D. B.; McMurry, P. H., *Environmental Science & Technology* **2002,** *37*, 577-583.

(15) Scheckman, J. H.; McMurry, P. H.; Pratsinis, S. E., *Langmuir* **2009,** *25*, 8248-8254.

(16) Stolzenburg, M. R.; McMurry, P. H., *Aerosol Science and Technology* **1991,** *14*, 48 - 65.

(17) Ehara, K.; Hagwood, C.; Coakley, K. J., *Journal of Aerosol Science* **1996,** *27*, 217-234.

(18) Scheckman, J. H. Mass-Mobility Relationship for Silica Agglomerates: Implications for Transport and Morphological Properties. University of Minnesota, Minneapolis, 2008.

(19) Emery, M. S. Theoretical Analysis of Data from DMA-APM System. University of Minnesota, Minneapolis, 2005.

(20) Hinds, W. C., *Aerosol Technology: Properties, Behavior, and Measurement of Airborne Particles*. 2nd ed.; 1999.

(21) Mukherjee, R. Mechanical Properties of Impact-Assembled Nanoparticle Composites: Fabrication, Measurements, and Simulation. University of Minnesota, Mineneapolis, 2007.

3

Impact Dynamics of Aerosolized Nanocrystal Agglomerates

The impact dynamics of aerosolized nanocrystal agglomerates is studied in this chapter. Tandem measurements by differential mobility analysis-aerosol particle mass analysis (DMA-APM) indicate that the aerosolized agglomerates are close to spherical. These measurements also show that the distance between neighboring nanocrystals in the agglomerate is reduced by increasing their concentration in the colloidal dispersion. Experiments were conducted in which the agglomerates were impacted on carbon substrates by either electrostatic precipitation or aerodynamic focusing, leading to low-speed (1-2 cm/s) or high-speed (100-150 m/s) impact, respectively. The impact deformation mode of agglomerates was found to undergo a solid-like to liquid-like transition as the concentration of nanocrystals in the colloidal dispersion was increased. Impact behavior in the solid-like regime is similar to that observed in granular materials.

The results also show the range of conditions under which deposits consisting of single monolayers (or other desired number of monolayers) of nanocrystals can be obtained, which is of potential interest for device applications.

3.1 Introduction

Colloidal semiconductor nanocrystals (NCs), or "quantum dots," with unique electrical, chemical, and optical properties have been intensively studied over the past two decades. Manufacturing of electronic and optoelectronic devices using colloidal nanocrystals as building blocks can potentially reduce the cost of fabrication.[1] The functionality and stability of these devices are strongly influenced by the detailed structure of the close-packed assemblies of NCs obtained from colloidal dispersion. The colloidal synthesis produces NCs that are composed of inorganic nanocrystallite cores and organic capping ligands. Thus the assembled NCs are a hybrid material consisting of inorganic cores and organic spacers. Such materials have been termed "nanocrystal solids"[1-3] or "quantum dot solids."[4-8] Better understanding of the properties of NC solids is of fundamental interest, and could also lead to improvements in the fabrication of NC devices. Previous studies have explored both the cohesive and granular properties of NC solids through static measurements and analysis. It has been shown that different cohesive strengths between the NC cores in NC solids can produce dramatically different behavior. Mueggenburg *et al.* demonstrated that a close-packed monolayer sheet of gold NCs ligated by dodecanethiol behaves like an elastic membrane,[9] while Lee *et al.* [2] showed by nanoindentation measurements that films of CdSe NCs capped by

trioctylphosphine oxide (TOPO) and trioctylphosphine (TOP) have viscoplastic properties. NC cores are chemically bonded to their neighbors by cross-linking. Ultrathin films of CdSe NCs were observed to crumple like thin sheets of paper or aluminum foil by Lin *et al.*,[10] and plastic deformation of spherical agglomerates made of cross-linked metallic NCs was observed by Klajn *et al*.[11] To our knowledge, the only previous report concerning the granular nature of NC solids was that of Lee *et al*.[2] They found that CdSe NC films ligated by TOPO and TOP have more of a polymeric nature than a granular character, but that granular features become apparent after crosslinking of NCs and removal of capping ligands.

Aerosolization of a colloidal dispersion containing semiconductor NCs by means of a nebulizer produces agglomerate particles that have been termed "quantum dot nanospheres," where each nanosphere contains multiple inorganic NCs, organic capping ligands and possibly other organic residue from the colloidal dispersion.[12-13] Each nanosphere can thus be thought of as a small piece of quantum dot solid.

Atomization of liquid dispersions containing quantum dots is used in the "mist deposition" technique for fabricating light-emitting diodes.[14] In previous work we showed that aerosolized quantum dot nanospheres could be focused using aerodynamic lenses to direct-write photoluminescent microscale lines and patterns.[15] Here we report the use of aerosol techniques to investigate the cohesive granular property of CdSe NC solids. The properties of quantum dot nanospheres aerosolized from colloidal dispersion were tested by impacting them on carbon substrates. Instead of chemical crosslinking that binds the NCs to each other, we find that the attractive interaction between the NC cores can be adjusted by varying the NC concentration in the colloidal dispersion. The

granular nature of the nanospheres was also studied by comparing the morphologies of deposited splats having different sizes and at different impact velocities. To our knowledge, this work represents the first study of the granular nature of quantum dot solids consisting of uncrosslinked CdSe NCs.

3.2 Tandem Aerosol Measurement of Size and Mass

The nearly monodisperse colloidal NCs used in this study were CdSe NCs prepared by the standard route.[16-17] Synthesized NCs were 4.7 nm in diameter and were capped by TOPO and dispersed in hexane. The number concentration, *n*, of the NCs in the colloid was determined from the optical absorbance at 350 nm.[18-19] Suspensions of NC agglomerates in carrier gas were sprayed from colloidal dispersions with a Collison atomizer. The atomization process was the same as that described in our previous work.[15]

The morphology and mass density of the aerosol particles produced by atomization were characterized by aerosol tandem measurements of size and mass.[20-21] Although the agglomerates are charged after aerosolization due to friction between the solvent and the metallic nozzle of the nebulizer, they were passed through a bipolar neutralizer using a radioactive source (Po-210) to ensure no more than a single charge per agglomerate. Aerosol enters the differential mobility analyzer (DMA) as a thin annular stream at the periphery of a laminar flow of clean dry air between two concentric cylinders. Only agglomerates with a specified mobility diameter exit from the outlet. The mass of these agglomerates is then determined by an aerosol particle mass analyzer (APM), located

downstream of the DMA, by balancing the electrical force on the agglomerates with the centrifugal force. Agglomerates from colloidal dispersions with four different concentrations (same synthesis batch) were characterized. Particles of known mobility diameter (from 70 nm to 160 nm) were selected with the DMA. For each of these particle sizes, mass was measured with the APM. Relationships between the mass (m) and mobility diameter (d_m) of the NC agglomerates are shown in Figure 3-1. For agglomerates composed of monodisperse and spherical primary particles, the relationship between m and d_m can be described as $m = kd_m^{D_f}$, where k is a constant, and D_f is referred to as the mass-mobility exponent, an indicator of particle morphology.[22] As can be seen in Figure 3-1, the m vs. d_m data for all dispersions tested are well fit by straight lines on a log-log plot. The mass-mobility exponents of the agglomerates (i.e., the slopes of these lines), are listed in Table 3-1. For all the dispersions tested these measurements yield a mass-mobility exponent of 3.0 ± 0.1, implying that the agglomerates are compact and close to spherical.

Knowing that the agglomerates are close to compact spheres, one can then calculate the mass density of the aggregates based on their diameter and mass. These results are shown in Figure 3-2. The measured mass densities of the agglomerates ranged from 1.32 to 2.50 g/cm^3, depending on the NC concentration in the colloidal dispersion. These values are all much higher than that of pure hexane (0.655 g/cm^3 at room temperature), suggesting nearly complete evaporation of free hexane from the droplets atomized from the dispersion. As most of the hexane evaporates after atomization, the agglomerates are composed of inorganic CdSe NCs in an organic matrix consisting of capping ligands and

organic residues. For agglomerates from the same dispersion, the mass density is seen to remain constant when the agglomerate mobility diameter increases, implying that the volume fraction comprised by the inorganic cores is independent of the agglomerate size. However, when the NC number concentration in the dispersion is increased, the volume fraction in the agglomerates increases as well, resulting in an increase in the agglomerate mass density (Table 3-2).

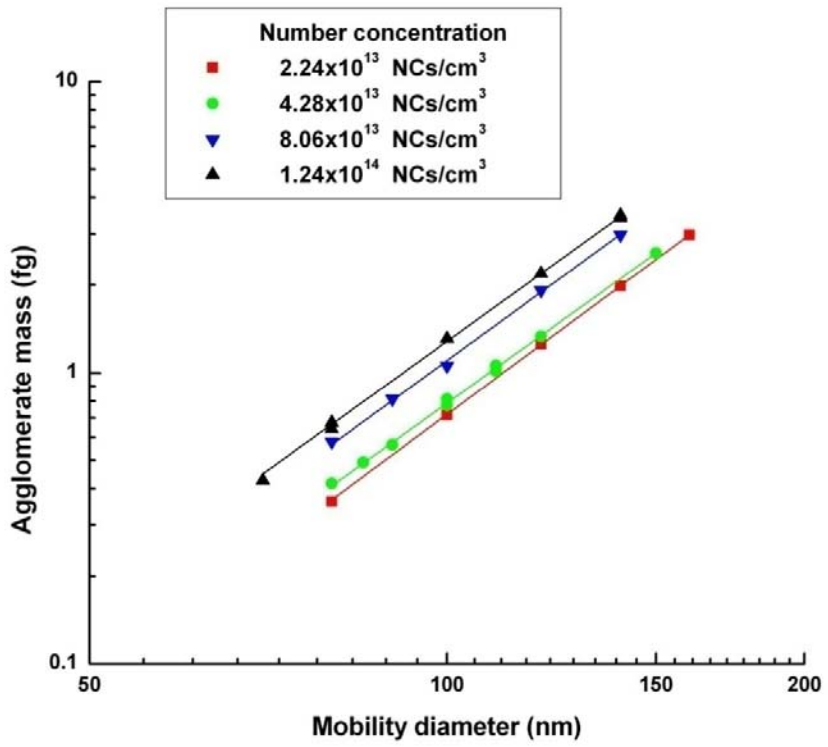

Figure 3-1. Mass-mobility relationships for nanocrystal agglomerates from differently concentrated colloidal dispersions in a log-log plot.

Table 3-1. The mass-mobility exponents D_f obtained from the fitting lines for different concentrations.

Number Concentration (NCs/cm^3)	**Mass-mobility exponent** D_f
2.24×10^{13}	3.04
4.28×10^{13}	2.91
8.06×10^{13}	2.95
1.24×10^{14}	2.99

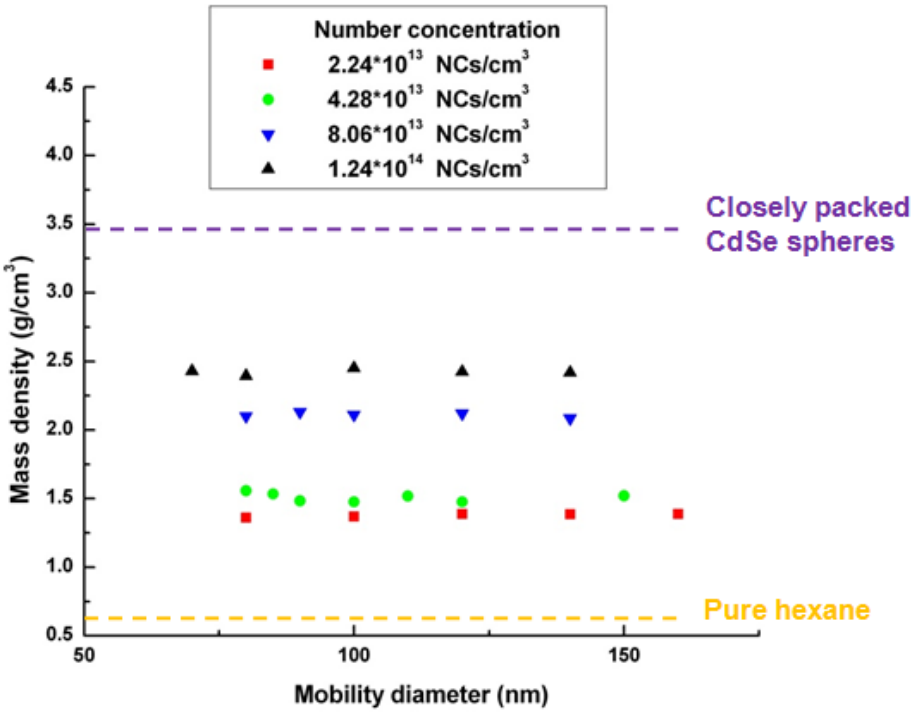

Figure 3-2. Relationships between calculated mass density of the nanocrystal agglomerates and their size. The orange dashed line shows the mass density of pure hexane solvent at room temperature. The purple dashed line indicates the mass density of randomly close-packed CdSe hard spheres at room temperature.

Table 3-2. The average mass density of nanocrystal agglomerates aerosolized from differently concentrated nanocrystal dispersions.

Number Concentration (NCs/cm^3)	**Average Mass Density** (g/cm^3)
2.24×10^{13}	1.32
4.28×10^{13}	1.63
8.06×10^{13}	2.09
1.24×10^{14}	2.50

3.3 Effect of Free Solvent in the Aerosolized Nanocrystals

Proceeding from this knowledge of the structure and morphology of the aerosolized NC agglomerates, experiments were conducted in which the agglomerates were impacted onto carbon substrates. As illustrated in Figure 3-3, two different methods were employed to impact-deform the nanospheres. When the aerosol was fed into a electrostatic precipitator, charged agglomerates approached the substrate at a steady drift velocity due to the electrical field applied across the electrode plates, resulting in an impact velocity of several centimeters per second. For high-velocity impaction tests, the aerosol was first electrically neutralized by a bipolar neutralizer using a radioactive source (Po-210). Then the agglomerates were focused by an aerodynamic lens system (a series of center-collimated orifices), after which they were accelerated to a terminal velocity of several hundred meters per second before bombarding a substrate located in a vacuum chamber. Details of this process are discussed by Qi *et al.*[15]. A difference in impact velocity of four orders of magnitude was thus achieved by utilizing these two different deposition processes. Hydrophobic carbon films (Ted Pella, Ultrathin Carbon

Type-A grids) were used as deposition substrates. The surface roughness of the substrates was measured by atomic force microscopy to equal ~0.7 nm.

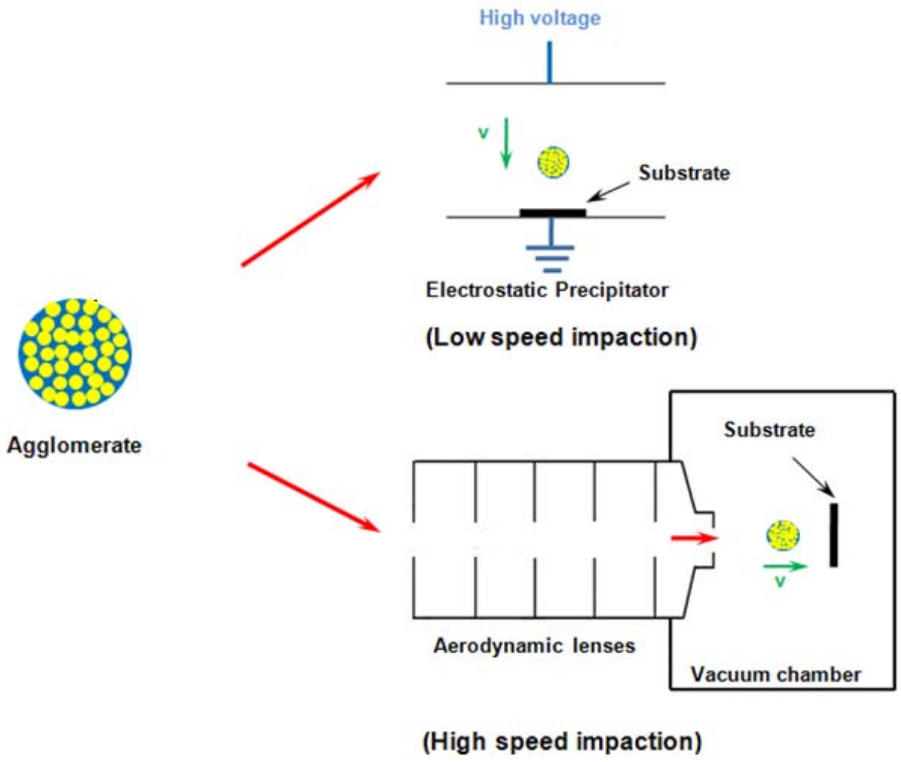

Figure 3-3. Schematic of experimental setup for low speed and high speed impactions of spherical nanocrystal agglomerates. Refer to Chapter 2 for details.

3.3.1 Nanocrystal Dispersions in Hexane

Figures 3-4a and 3-4b present typical morphologies of splats formed by nanospheres impacting on carbon substrates at ~2 cm/s and ~150 m/s respectively. At first glance, no obvious difference in the splat morphologies is seen between the two cases. All the

deposits have a roughly circular shape, without signs of either fracture or splash, suggesting that the NC cores within the agglomerates interact cohesively.

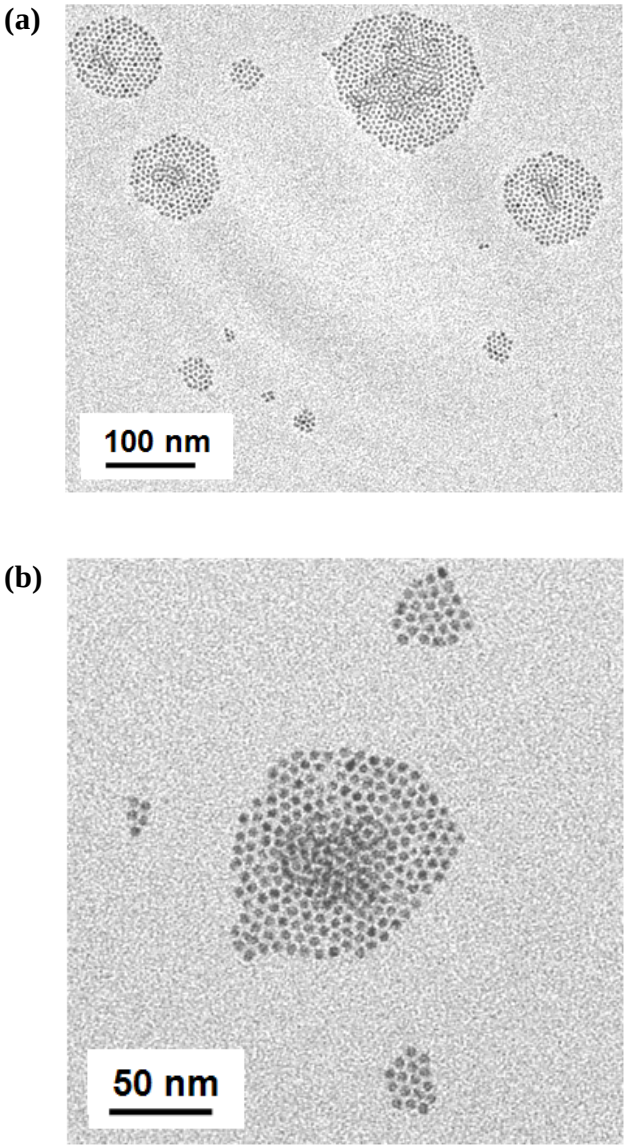

Figure 3-4. Transmission electron microscopy (TEM) images of impacted nanocrystals on carbon substrate. (a) nanospheres impact at ~2 cm/s. (b) nanospheres impact at ~150 m/s.

3.3.2 Nanocrystal Dispersions in Toluene

To verify the cohesion between NC cores in agglomerates aerosolized from colloidal dispersion hexane, the impaction experiments were repeated using NC dispersions in toluene, which is less volatile than hexane. The mass density of these agglomerates, measured by DMA-APM, equalled 0.87 g/cm^3, virtually identical to the density of pure toluene (0.867 g/cm^3). This indicates that the agglomerates of NCs in toluene were dilute solution droplets rather than spherical NC aggregates before bombardment on the substrates. Under identical experimental conditions, the impact morphologies were notably different for agglomerates prepared from toluene and hexane solutions. For toluene, ring patterns of NCs are formed at low impact velocity (Figure 3-5a), while the deposits formed by high-velocity impact appear to consist of randomly scattered NCs (Figure 3-5b). These morphologies both suggest an absence of cohesion between the NCs. The NCs stably disperse in toluene, resulting in repulsive interaction between the NC cores, a well-known "good solvent" effect.[23] When the aerosolized droplets impacted the substrate at low velocity (Figure 3-5a), they spread on the hydrophobic carbon surface. The ring patterns of NCs are probably due to the "coffee ring" effect, in which the non-uniform evaporation rate of solvent across the droplet induces the replenishment of solvent from the interior to the edge, resulting in capillary flows that push the NCs in the droplet to the edge.[24] Under high-velocity impact (Figure 3-5b), the droplets appeared to splash and break up into smaller drops.[25] After evaporation of the toluene, randomly distributed NCs remain. Thus, comparison of the morphologies of impacted NCs that were originally dispersed in either hexane or toluene further confirms the complete

evaporation of hexane but not toluene, and the existence of NC cohesive interaction within the aerosolized NC agglomerates in the hexane case but not the toluene case.

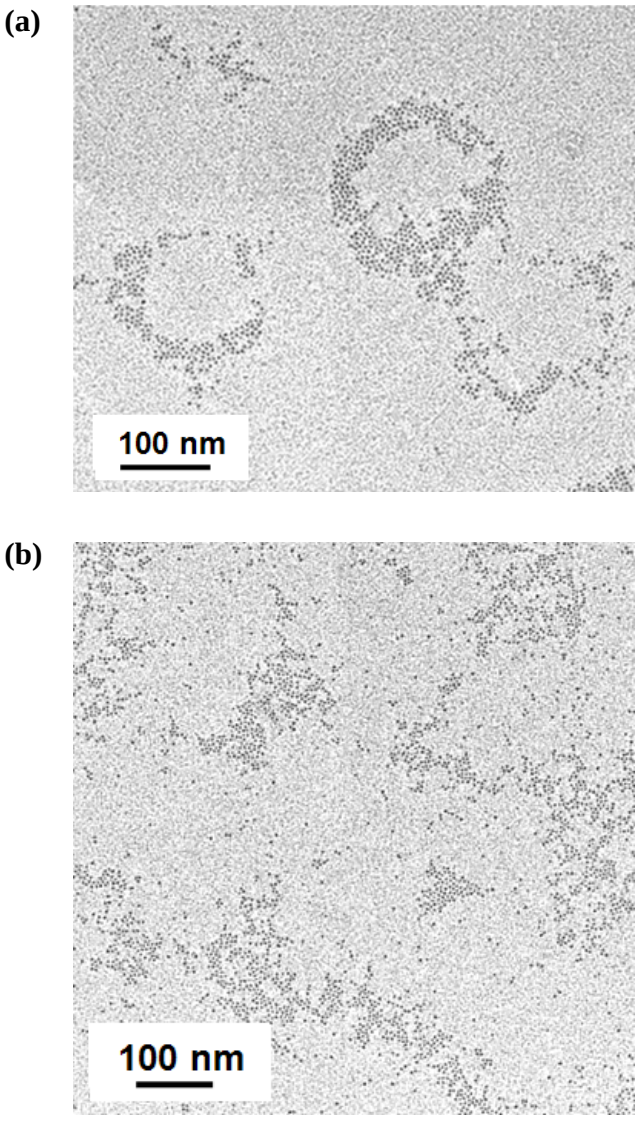

Figure 3-5. Transmission electron microscopy (TEM) images of impacted nanocrystals on carbon substrate. The nanocrystals were aerosolized from dispersion in toluene. (a) colloidal droplet impact at ~1 cm/s, (b) colloidal droplet impact at ~100 m/s.

3.4 Effect of Number Concentration

Figures 3-6 and 3-7 show scanning transmission electron microscopy (STEM) images of nanosphere splats produced under different impact scenarios, using in all cases dispersions in hexane. Figures 3-6a and 3-6b show images of deposits from a relatively concentrated NC dispersion (n = 1.24×10^{14} NCs/cm^3) impacting at either high or low velocity, respectively, while Figures 3-7a and 3-7b show the corresponding images for the case of more dilute dispersion (n = 4.28×10^{13} NCs/cm^3).

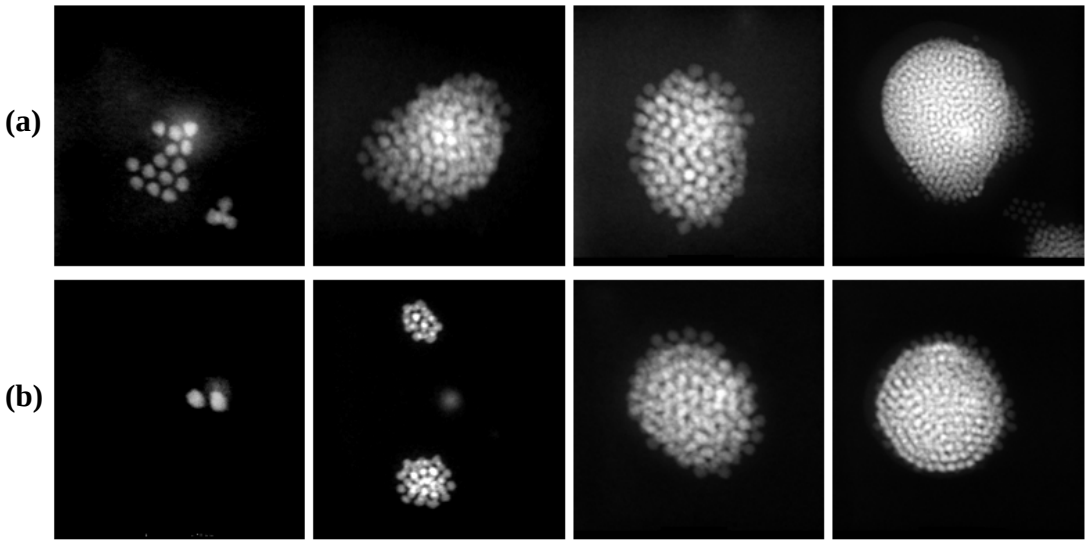

Figure 3-6. STEM images of deformed nanocrystal solid spheres on carbon substrate. (a) nanocrystal solid spheres aerosolized from concentrated NC dispersion (1.24×10^{14} NCs/cm^3) and impacted at ~150 m/s. (b) nanocrystal solid spheres aerosolized from concentrated NC dispersion (1.24×10^{14} NCs/cm^3) and impacted at ~2 cm/s.

The number of NCs per agglomerate increases from left to right in each row of images. The leftmost images in each row indicate that, for any given set of conditions, agglomerates containing a sufficiently small number of NCs tend to form splats consisting of a single monolayer. For larger agglomerates, however, the splat morphology is strongly affected by the concentration of the NC dispersion, and to a lesser extent by the impact velocity.

In the case of more concentrated dispersion, Figures 3-6a and 3-6b, the nanospheres resist spreading on the substrate, suggesting glassy solid-like behavior and strong cohesion between the NCs. For the case of more dilute dispersion, Figures 3-7a and 3-7b, the agglomerates behave more like a viscous liquid during impact, spreading on the carbon substrate and forming pile-shaped structures with multiple-monolayer centers and single-monolayer skirts. For the case of both dilute dispersion and high impact velocity (Figure 3-7a), large nanospheres tend to splash, leaving a separate ring around the central splat. In this case randomly distributed branching of NCs at the splat periphery, which is one of the characteristics of droplet impaction (also called "fingering" in droplet impact dynamics), is also evident. According to the results of the mass density measurements discussed above, the volume fraction of NC cores in the agglomerates increases with the number concentration of NCs in the colloidal dispersion. Since the CdSe NCs in this study are all of the same size, this increase in volume fraction implies that there is less organic material and thus narrower spacing between neighboring NCs. As the NCs become closer, their cohesion becomes stronger, inducing a liquid-to-solid transition in the impact behavior of the NC agglomerates. Thus, cohesion between the NCs plays a critical role in determining the rheological properties of colloidal quantum dot

nanospheres. Moreover, the cohesion can be modified by simply adjusting the number concentration of the colloidal dispersion that is aerosolized.

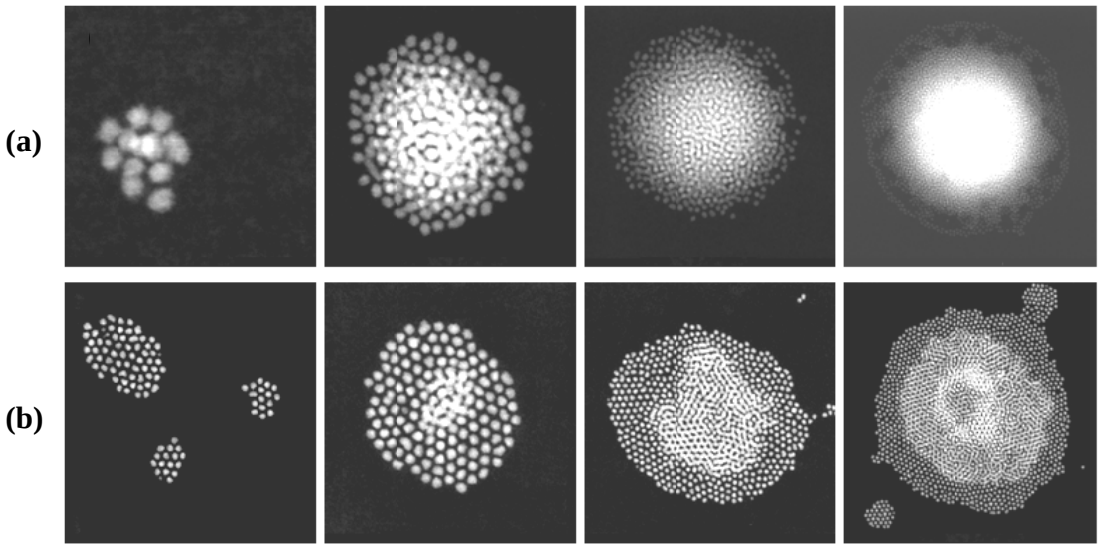

Figure 3-7. STEM images of deformed nanocrystal solid spheres on carbon substrate. (a) nanocrystal solid spheres aerosolized from diluted NC dispersion (4.28×10^{13} NCs/cm^3) and impacted at ~150 m/s. (b) nanocrystal solid spheres aerosolized from diluted NC dispersion (4.28×10^{13} NCs/cm^3) and impacted at ~ 2 cm/s.

3.5 Quantitative Characterization of Scanning Transmission Electron Microscopy (STEM) Images

Since STEM uses a narrow (~1 Å wide) electron beam that rasters the selected region, the high-angle annular dark-field image represents the collection of incoherently

and elastically scattered electrons. The intensity of each pixel in the image is therefore linearly proportional to the local sample thickness, especially for the small CdSe NCs imaged.[26] By scanning across a line one can then infer the thickness profile of the agglomerate splats, and the corresponding number of NC monolayers.

3.5.1 Thickness Determination of Deformed Nanocrystal Agglomerates

Figure 3-8a shows a STEM image of a monolayer of 16 NCs on carbon substrate. Since the NCs are nearly monodisperse, the peak brightness of each single NC in Figure 3-8b is also close to each other. Here, we use the one monolayer of NC as the unit of measure to determine the height of the deformed agglomerates. As the local brightness is proportional to the thickness of the material in STEM images in this case, the thickness can be determined the formula as following:

$$\text{Thickness of the deformed agglomerate} = \frac{240-10}{60-10} \approx 4.6 \text{ monolayers.}$$

For the sample shown in Figure 3-9a, we know that the maximum brightness is 200, that peak brightness of an individual NC is 192 (red dotted box), and that the background brightness is about 35, by reading the brightness intensity curve shown in Figure 3-9b. Thus, the thickness of this sample is (200-35)/(192-35)≈1.05 monolayers, which is consistent with the single monolayer shown in the figure. In the same manner, we can obtain the thickness of the sample shown in Figure 3-9a, which is (240-10)/(60-10) ≈4.6 monolayers.

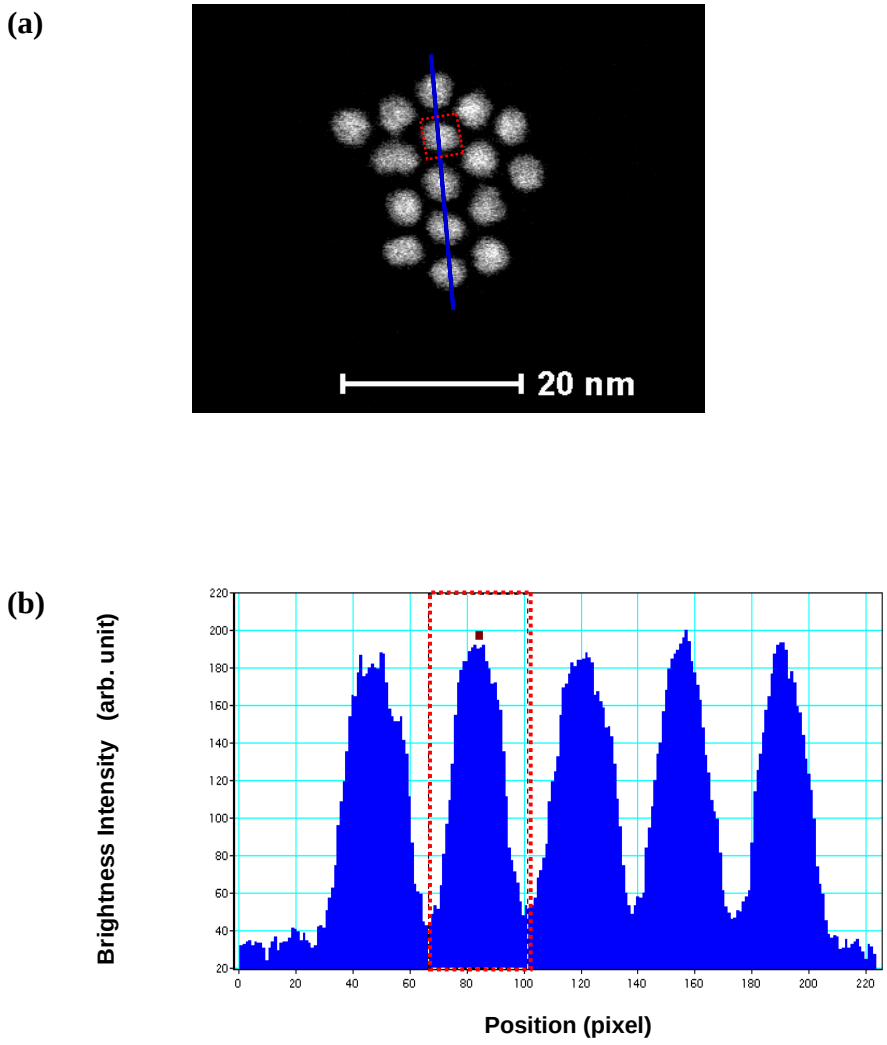

Figure 3-8. (a) STEM image of a single monolayer of impacted nanocrystals on carbon substrate. (b) Brightness intensity of each pixel along the blue line in (a).

(a)

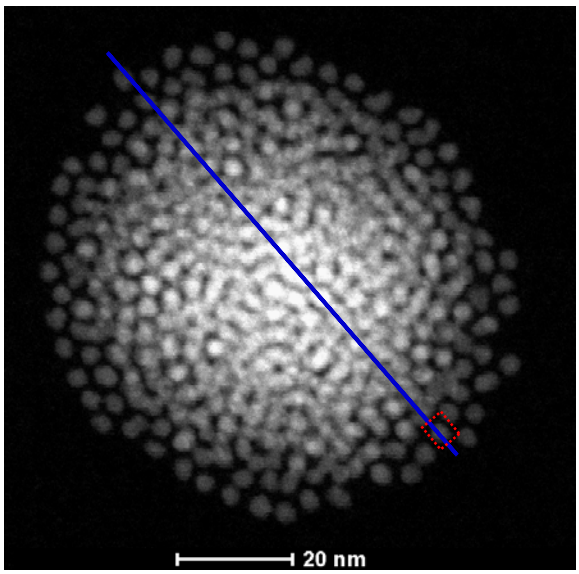

(b)

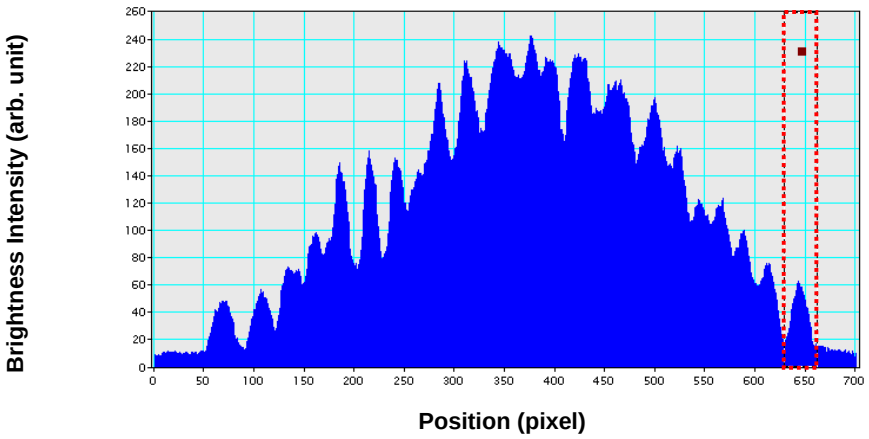

Figure 3-9. (a) STEM image of a deformed nanocrystal sphere on carbon substrate after impaction. (b) Brightness intensity of each pixel along the blue line in (a).

3.5.2 Estimation of the number of nanocrystals

The integral brightness over an area was used to estimate the number of NCs in the STEM image. The integral brightness was calculated by summing the brightness of each pixel within a selected region. If we use the integral brightness of a single NC as the base, then the total number of NCs in the sample can be estimated by the following formula:

$$\text{Number of NCs} = \frac{\text{Integral brightness of the whole sample} - \text{Background}}{\text{Integral brightness of a single NC} - \text{Background}} .$$

For the background brightness, the average background brightness per pixel was firstly obtained by sampling a dark region in the image. Then the background brightness for the sample and the individual NC were the product of the pixel background brightness and the number of pixels in the selected area.

Take the sample in Figure 3-10a for example. The yellow dotted square denotes the selected area for the integral brightness of the whole sample, and the red square shows the region selected to calculate the integral brightness of a single NC. Thus, the total number of NCs in the sample is (2602072.3-0.093×191×170)/(155064.5-0.093×33×33) ≈ 16.8. By counting the number of NCs directly from the image, we know the exact number is 16. The number of NCs in Figure 3-10b and 3-10c can be estimated in the same manner. The results of estimation are summarized in Table 3-3. The errors of estimation are 5%, -11%, and 6%, respectively. Overall, comparisons between the estimation and direct counting show that the maximum error of the estimation is about 15%. Thus, 15% error bars were marked on the data points in Figure 3-14.

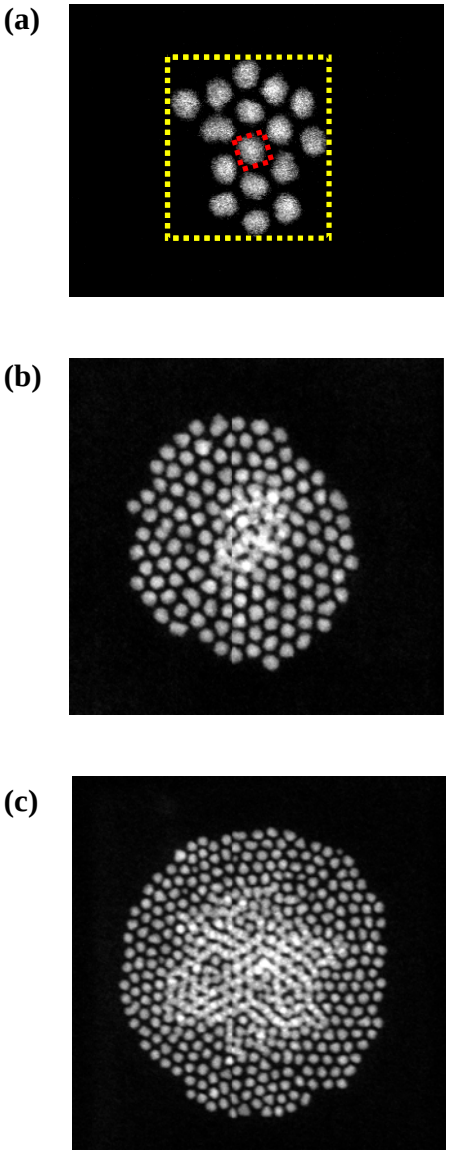

Figure 3-10. STEM images of impacted nanocrystal agglomerates on carbon substrate. The agglomerate consists of (a)16 nanocrystals, (b) ~152 nanocrystals, and (c) ~510 nanocrystals. The diameter of the each nanocrystal is about 4.7 nm.

Table 3-3. The comparison between the estimated number of nanocrystals in the sample and the actual number by direct counting STEM images.

Sample	Estimated Number	Actual Number	Error
(a)	16.8	16	5%
(b)	135.7	152	-11%
(c)	541.2	510	6%

3.5.3 Estimation of Volume Fraction of Nanocrystals in Agglomerates

Since we know the individual NC diameter and the number of NCs within an agglomerate, the volume fraction of NCs in the agglomerate can be determined if we know the size of the agglomerate, which can be measured by the DMA. Figure 3-11 are STEM images of high-velocity-impacted NC agglomerates, which were sized by the DMA. Since the NCs were atomized from a dilute dispersion in hexane (2.24×10^{13} NCs/cm^3), deformed agglomerates spread on the carbon substrate like a viscous liquid. The sizes of splats are close for the agglomerates with the same diameter, as shown in Figure 3-11.

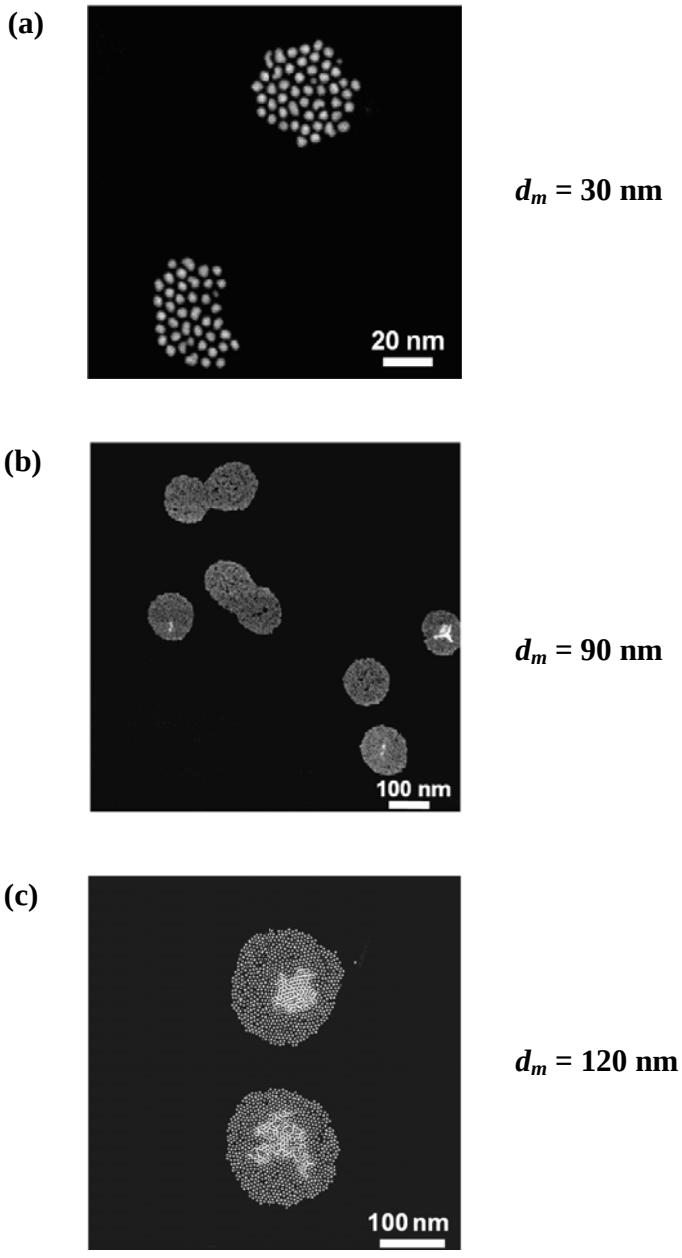

Figure 3-11. STEM images of splats of nanocrystal agglomerates classified by DMA after high-velocity impact. The mobility sizes of the impacted agglomerates are (a) 30 nm, (b) 90 nm, and (c) 120 nm. The number concentration of nanocrystal dispersion is 2.24×10^{13} NCs/cm^3.

By the means mentioned in section 3.5.2, the number of the NCs per agglomerate (N_a) can be estimated from the STEM images. Figure 3-12 summarizes the N_a vs. d_m data, which are well fit by a straight line in the log-log plot. The exponent of the equation in the inset of Figure 3-12 is given by the slope of the fitting line. The value of the exponent is 2.934, which is close to 3.0, again indicating that the agglomerates are compact spheres. As the diameter of the NCs is 4.7 nm, we can then calculate the volume fraction of NCs based on the N_a vs. d_m data. Similar to the mass densities of agglomerates with different sizes, the volume fraction of NCs is also consistent, as can be seen in Figure 3-13. The average volume fraction of NCs is about 21%.

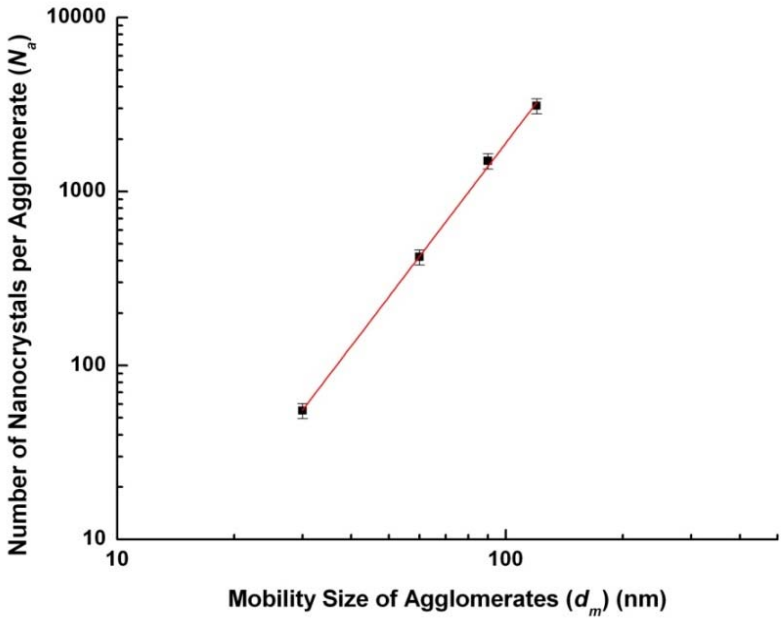

Figure 3-12. The relationship of mobility size and number of nanocrystals per agglomerate.

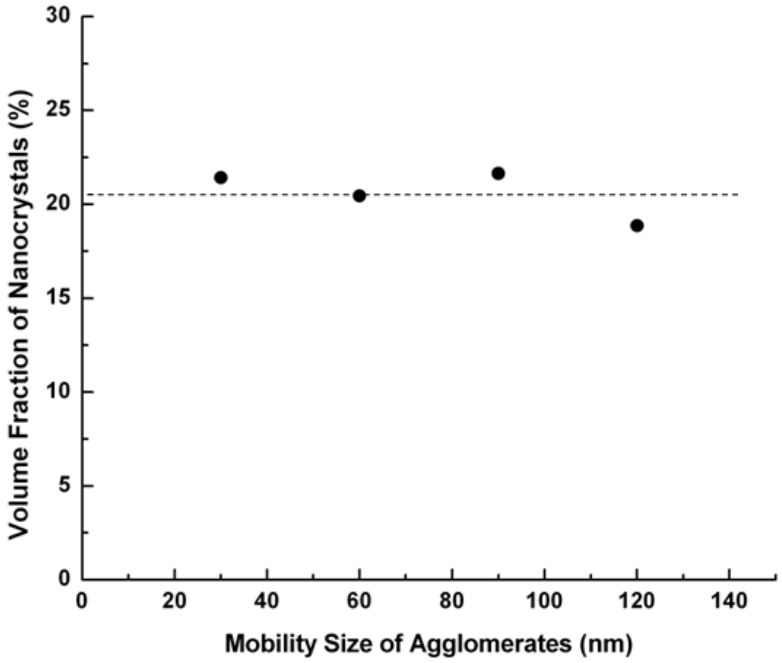

Figure 3-13. The relationship of mobility size and volume fraction of nanocrystal cores for agglomerates. Dotted line indicates the average volume fraction is around 21%.

3.6 Granular Nature of the Nanocrystal Agglomerates

STEM images were also used to characterize the granular nature of the splats. Based on data extracted from the STEM images, Figure 3-14 summarizes the results relating the thickness (number of monolayers) of the agglomerate splats, the number N_a of NCs per agglomerate, the NC concentration n in the dispersion, and the impact velocity. Several trends that are evident in this figure can be related to the relative strength of cohesive forces between the NCs in an agglomerate.

For a sufficiently small number N_a of NCs per agglomerate, the deposits consist of a single monolayer, regardless of the dispersion concentration or the impact velocity. As

N_a increases beyond some critical value a second monolayer begins to form, and thereafter the deposit thickness increases as a step function of N_a. The stacking of NCs is analogous to "arching" in granular materials (for example, in sand).[27] For solid granular media, grain particles arch because of the friction between particle contacts. In the case of colloidal quantum dot nanospheres, our results suggest that arching occurs due to the cohesion between the NC cores.

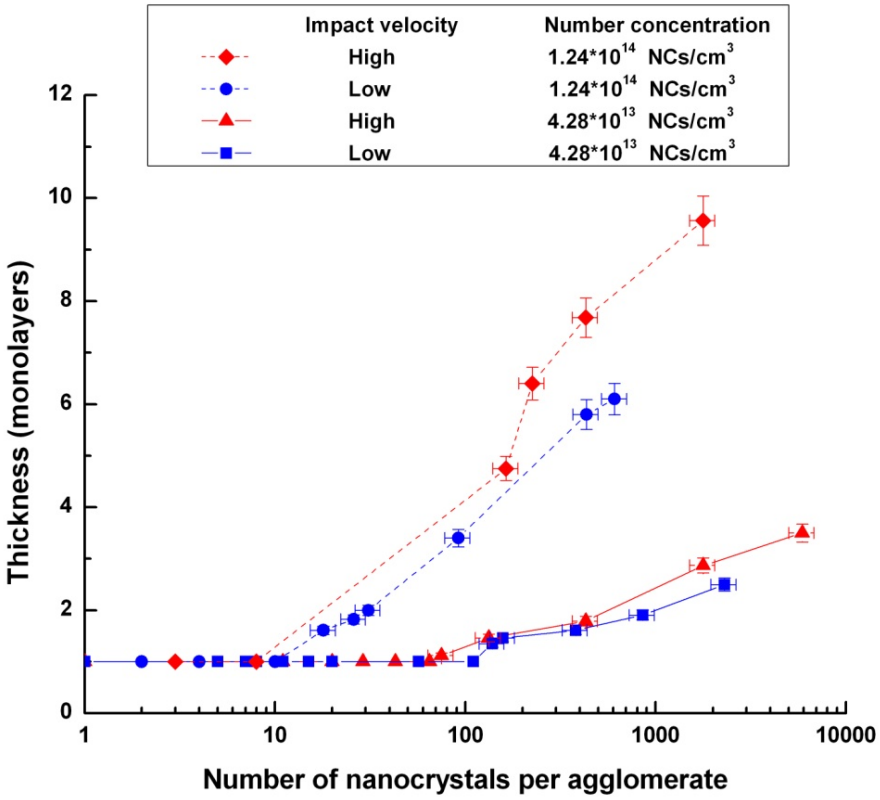

Figure 3-14. Relationships between the thickness of the deformed nanospheres and the number of nanocrystals within the spheres.

Once the deposits are thicker than a monolayer, Figure 3-14 indicates that high-velocity impacts tend to produce thicker deposits than low-velocity impacts, for agglomerates containing the same number of NCs. This thickening effect can be interpreted in terms of the time-dependent cooperative rearrangement of NCs during impact deformation, as NCs inside the agglomerate are likely to jam if impacted at high velocity.

It is known that granular materials can flow like a liquid, if an external perturbation whose strength is above a certain threshold level is applied.[28] Attractive forces between the grains will increase the level of this threshold. Strongly cohesive nanoparticles are unlikely to flow, as demonstrated in Figures 3-6a and 3-6b, and ref.[11] This phenomenon is more evident when two splats overlap, as shown in the TEM images in Figure 3-15. Figures 3-15a and 3-15b show deposits from the high-concentration dispersion, from high-velocity and low-velocity impacts, respectively, while Figures 3-16a and 3-16b show corresponding deposits for the case of the low-*n* dispersion. In the high-*n* (strong NC cohesion) case the boundaries of each nanosphere are clearly seen in the overlap region, regardless of the impact velocity, while in the low-*n* case the NCs in the overlap region start to flow and rearrange themselves. The nanospheres aerosolized from the more dilute dispersion are able to coalesce and form a more continuous deposit of NCs in both the high- and low-velocity impact cases. These results are consistent with the solid-to-liquid transition discussed in section 3.4.

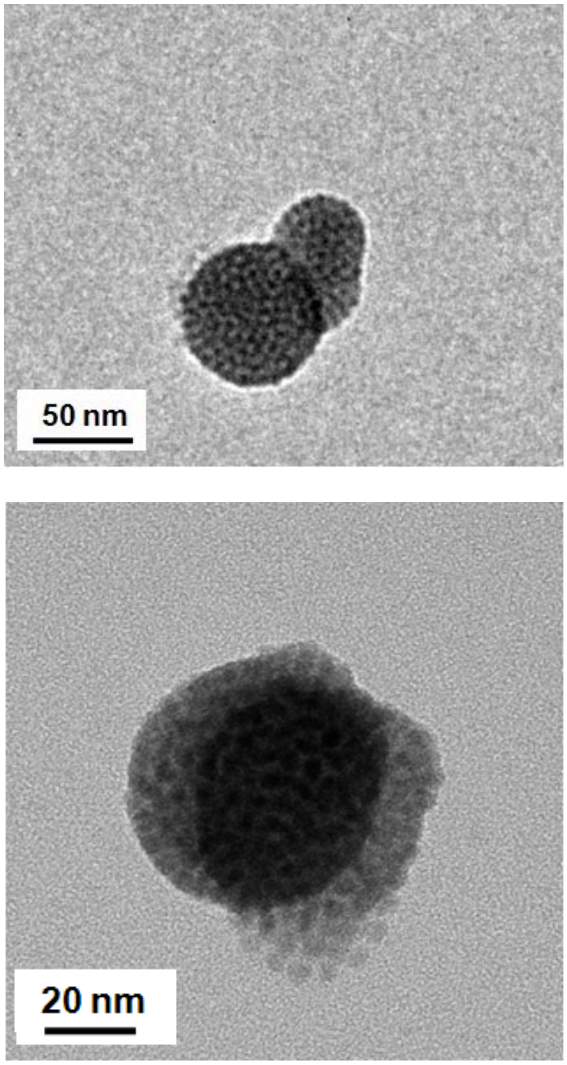

Figure 3-15. TEM images of overlapped splats on carbon substrate after impaction. (a) nanocrystal agglomerates aerosolized from concentrated NC dispersion (1.24×10^{14} NCs/cm^3) and impacted at ~150 m/s. (b) nanocrystal agglomerates aerosolized from concentrated NC dispersion (1.24×10^{14} NCs/cm^3) and impacted at ~2 cm/s.

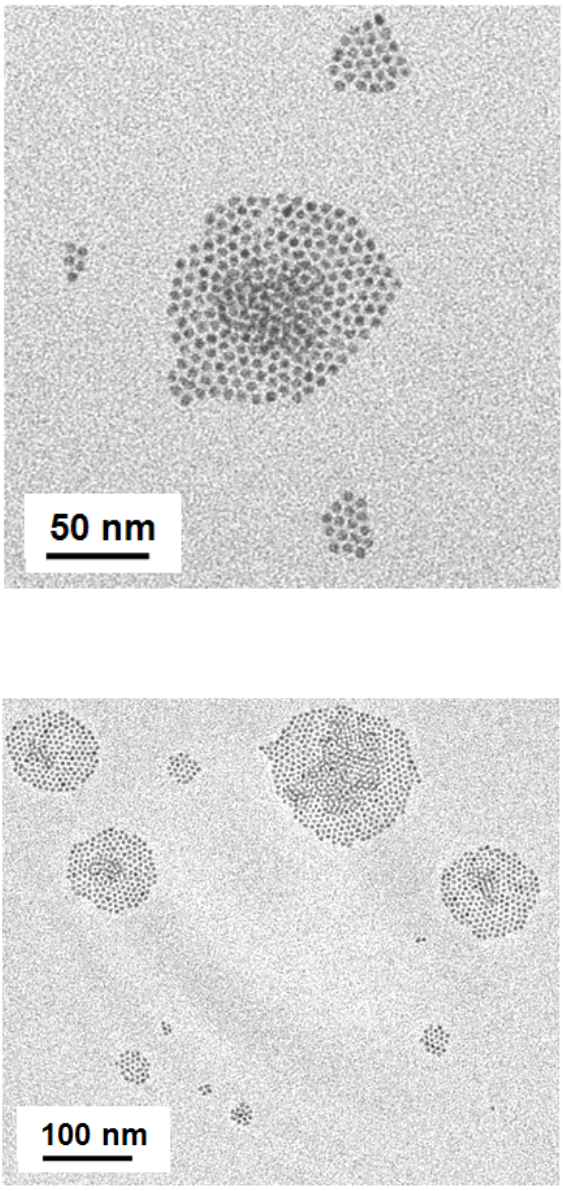

Figure 3-16. TEM images of overlapped splats on carbon substrate after impaction. (a) nanocrystal agglomerates aerosolized from concentrated NC dispersion (4.28×10^{13} NCs/cm^3) and impacted at ~150 m/s. (b) nanocrystal agglomerates aerosolized from concentrated NC dispersion (4.28×10^{13} NCs/cm^3) and impacted at ~2 cm/s.

3.7 Conclusion

In summary, we have studied the impact dynamics of aerosolized colloidal quantum dot nanospheres, where each nanosphere consists of an agglomerate of CdSe NCs in an organic matrix. Aerosol mass-mobility measurements indicate that these agglomerates are close to spherical, and also reveal that the spacing between NCs decreases as the NC concentration in the colloidal dispersion increases. As the spacing between NCs is reduced, their attractive interaction becomes stronger. Experiments conducted with both high- and low-velocity impact of the nanospheres on carbon substrates demonstrated that the impact dynamics are decisively determined by the cohesive interaction (or lack thereof) of the nanospheres. As the spacing between NCs is reduced, the nanosphere impacts undergo a liquid-to-solid transition behavior. Mildly cohesive nanospheres that are aerosolized from relatively dilute dispersions exhibit liquid-like behavior, including splashing at high-velocity impaction and coalescence of overlapping splats. In contrast, strongly cohesive nanospheres that are aerosolized from more concentrated dispersions exhibit arching and thickening, typical behavior of granular materials.

Aside from their fundamental significance, the results of this study may be helpful in guiding aerosol-based printing of colloidal NCs. Our findings suggest that the number of monolayers deposited can be controlled by adjusting the concentration of NCs in the colloidal dispersion, and, to a lesser extent, by the impact velocity.

3.8 Acknowledgement

This work was supported by the NSF Nanoscale Interdisciplinary Research Team (NIRT) program (CTS-0506748) and utilized resources at the University of Minnesota

Characterization Facility, funded by NSF through the NNIN program. D.J.N. benefited from financial support from the Alexander von Humboldt Foundation. We thank J. Scheckman for his assistance in the DMA-APM measurements, M.S. Kang for his help with the AFM characterization of carbon substrate, and U. Ozan for helpful discussions of STEM imaging.

3.9 References

(1) Talapin, D. V.; Murray, C. B., *Science* **2005,** *310*, 86-89.

(2) Lee, D.; Jia, S.; Banerjee, S.; Bevk, J.; Herman, I. P.; Kysar, J. W., *Phys. Rev. Lett.* **2007,** *98*, 026103.

(3) Murray, C. B.; Kagan, C. R.; Bawendi, M. G., *Annual Review of Materials Science* **2000,** *30*, 545-610.

(4) Vanmaekelbergh, D.; Liljeroth, P., *Chem. Soc. Rev.* **2005,** *34*, 299–312.

(5) Houtepen, A. J.; Kockmann, D.; Vanmaekelbergh, D., *Nano Lett.* **2008,** *8*, 3516–3520.

(6) Chandler, R. E.; Houtepen, A. J.; Nelson, J.; Vanmaekelbergh, D., *Phys. Rev. B* **2007,** *75*, 085325.

(7) Houtepen, A. J.; Vanmaekelbergh, D., *J. Phys. Chem. B* **2005,** *109*, 19634–19642.

(8) Soreni-Harari, M.; Mocatta, D.; Zimin, M.; Gannot, Y.; Banin, U.; Tessler, N., *Adv. Funct. Mater.* **2010,** *20*, 1005-1010.

(9) Mueggenburg, K. E.; Lin, X. M.; Goldsmith, R. H.; Jaeger, H. M., *Nat. Mater.* **2007,** *6*, 656-660.

(10) Lin, Y.; Skaff, H.; Boker, A.; Dinsmore, A. D.; Emrick, T.; Russell, T. P., *J. Am. Chem. Soc.* **2003,** *125*, 12690-12691.

(11) Klajn, R.; Bishop, K. J. M.; Fialkowski, M.; Paszewski, M.; Campbell, C. J.; Gray, T. P.; Grzybowski, B. A., *Science* **2007,** *316*, 261-264.

(12) Chu, M. Q.; Wu, F.; Zhang, Q.; Liu, T. T.; Yu, Y.; Ji, A. L.; Xu, K. Y.; Feng, Z. H.; Zhu, J., *Nanoscale* **2010,** *2*, 542-547.

(13) Kim, D. J.; Koo, K. K., *Cryst. Growth Des.* **2009,** *9*, 1153-1157.

(14) Zhu, T.; Shanmugasundaram, K.; Price, S. C.; Ruzyllo, J.; Zhang, F.; Xu, J.; Mohney, S. E.; Zhang, Q.; Wang, A. Y., *Appl. Phys. Lett.* **2008,** *92*, 3.

(15) Qi, L.; McMurry, P. H.; Norris, D. J.; Girshick, S. L., *Aerosol Sci. Technol.* **2010,** *44*, 55-60.

(16) Peng, Z. A.; Peng, X. G., *J. Am. Chem. Soc.* **2001,** *123*, 183-184.

(17) Reiss, P.; Bleuse, J.; Pron, A., *Nano Lett.* **2002,** *2*, 781-784.

(18) Klimov, V. I.; McBranch, D. W.; Leatherdale, C. A.; Bawendi, M. G., *Phys. Rev. B* **1999,** *60*, 13740-13749.

(19) Leatherdale, C. A.; Woo, W. K.; Mikulec, F. V.; Bawendi, M. G., *J. Phys. Chem. B* **2002,** *106*, 7619-7622.

(20) Park, K.; Kittelson, D. B.; McMurry, P. H., *Aerosol Science and Technology* **2004,** *38*, 881-889.

(21) Scheckman, J. H.; McMurry, P. H.; Pratsinis, S. E., *Langmuir* **2009,** *25*, 8248-8254.

(22) Mandelbrot, B. B., *The Fractal Geometry of Nature*. Freemann: San Francisco, 1982.

(23) Schapotschnikow, P.; Pool, R.; Vlugt, T. J. H., *Nano Lett.* **2008,** *8*, 2930-2934.

(24) Deegan, R. D.; Bakajin, O.; Dupont, T. F.; Huber, G.; Nagel, S. R.; Witten, T. A., *Nature* **1997,** *389*, 827-829.

(25) Yarin, A. L., *Annu. Rev. Fluid Mech.* **2006,** *38*, 159-192.

(26) Liu, J. Y., *J. Electron Microsc.* **2005,** *54*, 251-278.

(27) Duran, J., *Sands, Powders, and Grains: An Introduction to the Physics of Granular Materials*. Springer-Verlag: New York, 2000.

(28) Jaeger, H. M.; Nagel, S. R.; Behringer, R. P., *Rev. Mod. Phys.* **1996,** *68*, 1259-1273.

4

Direct Aerosol Printing of Monolayer Nanocrystal Films

The capability of aerodynamic lenses in direct-writing ultrathin patterns of colloidal nanocrystals will be tested in this chapter. Proceeding from the knowledge of cohesive granular properties of aerosolized nanocrystal agglomerates from colloidal dispersion in hexane, single monolayer of CdSe nanocrystals was deposited from collimated beams of nanocrystal agglomerates formed by aerodynamic focusing. For individual nanocrystal diameters of 4.3 nm, the upper limit on the agglomerate diameter for monolayer deposition was found to equal ~50 nm. Multiple-layer micropatterns of nanocrystals were printed by focusing 100-nm nanocrystal agglomerates. The effect of surface wettability of the substrates was also investigated. We found that deposits of individual NC agglomerates on carbon (hygrophobic) and silica (hygrophilic) films were similar in appearance. However, while it was possible to form uniform monolayers of NC

agglomerates on the carbon films, the agglomerates deposited on silica under identical conditions accumulated in islands that were surrounded by regions that contained no NCs.

4.1 Introduction

Due to their high quantum yield, narrow spectral emission band, size-tunable bandgap, chemical stability, and easy processibility, semiconductor nanocrystals (NCs) researchers have been exploring their applications to new electronic and optoelectronic devices.[1-2] A variety of NC-based devices, such as light emitting devices (LEDs),[3-6] photodetectors,[7-9] solar cells,[10-14] and thin film transistors,[15-17] have been developed. On the other hand, it is still challenging to print patterned monolayer NC films, which is an essential step in the fabrication of some devices. To date, almost all the record performances of NC-LEDs have been achieved with devices containing NCs of 1-5 monolayer thickness.[3-6] NC-based transistors also require patterned deposits that are 1-3 monolayers thick.[15-17]

Here, we report the direct aerosol printing of monolayer films of colloidal CdSe NCs on carbon substrates by aerodynamic focusing. To our knowledge, for the first time, a single monolayer NC film was obtained by direct-write techniques. Compared with other deposition methods, the operation of aerodynamic lenses requires low pressures in the focusing and deposition parts of the system, which might appear to be a significant disadvantage. However, vacuum systems have been widely used in the deposition of other functional layers in device fabrication, such as thin metal electrodes, conducting organic films, and oxide layers. An aerodynamic lens assembly can be designed so that it

can be readily incorporated into these vacuum systems. Thus, the device fabrication can be completed within one vacuum chamber.

4.2 Deposition of Polydisperse Nanocrystal Agglomerates

The nearly monodisperse CdSe NCs used in this study were synthesized by the standard route.[18-19] The diameter of synthesized NCs was 4.3 nm. The NCs were capped by trioctylphosphine oxide (TOPO) and dispersed in hexane (CHROMASOLV Plus, Aldrich). The atomization and aerodynamic focusing were the same as described in our previous work.[20] The number concentration of the colloidal NC dispersion was about 2×10^{13} NCs/cm^3. Without specific declaration, the deposition substrate was ultrathin carbon film (Ultrathin Carbon Type-A grids, Ted Pella). As shown in Figure 2-7, polydisperse NCs agglomerates were generated by a Collison atomizer using pressurized air. Figure 4-1 presents the TEM image of a typical deposit obtained by focusing these polydisperse agglomerates, when the substrate was translated at a velocity of 80 μm/s. Not surprisingly, a non-uniform and discontinuous film was deposited on the carbon substrate. As shown in the enlarged blue square, very dark dots appear like supraspheres of NCs, which are probably deposits of very big NC agglomerates. Many islands of multiple layers of NCs show up as in the enlarged red square, which are the deposits of smaller agglomerates. Since no obvious boundaries could be seen for overlapped agglomerate deposits, the dispersion was dilute and the NCs were mildly cohesive to each other in the agglomerates. The aerosolized NC agglomerates behaves like an assembly of cohesive granules during impact deformation (see section 3.6).

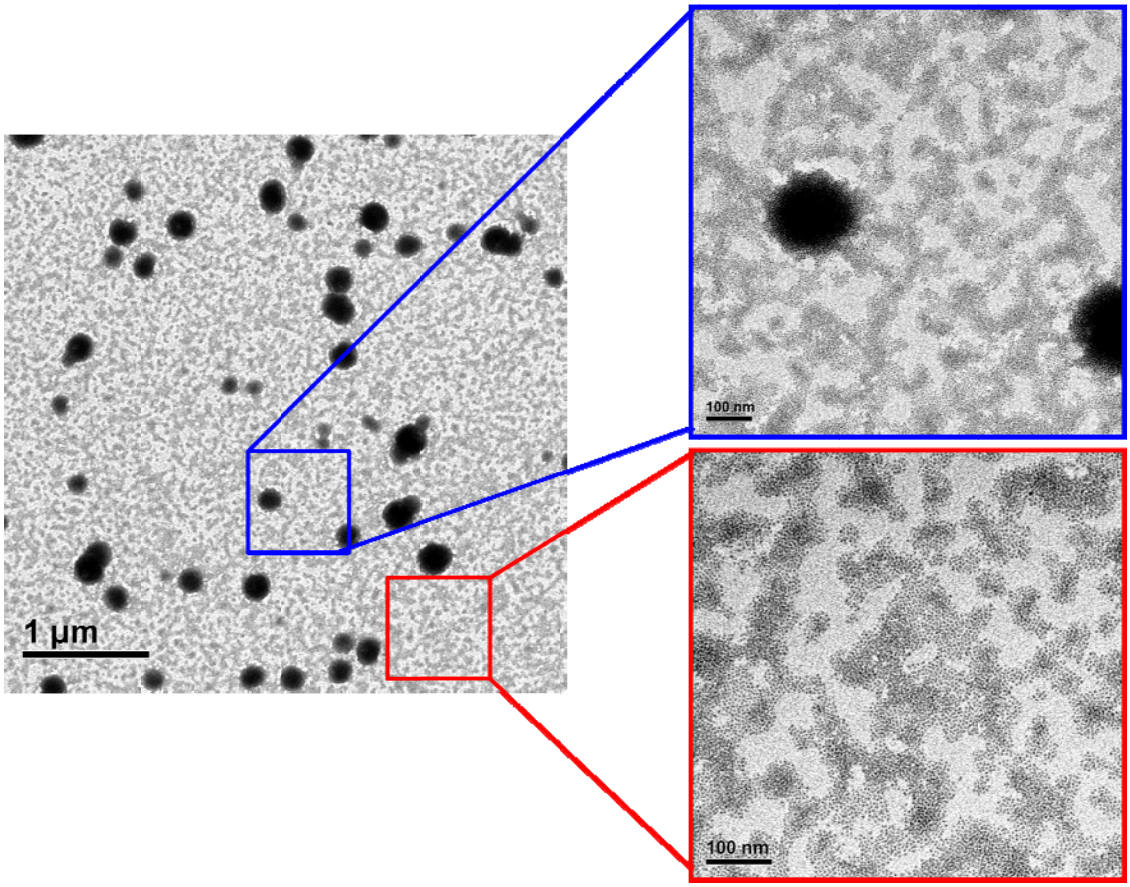

Figure 4-1. TEM images of a typical deposit obtained by printing polydisperse nanocrystal agglomerates onto carbon substrates with aerodynamic lenses. Enlarged blue and red squares give a more detailed look at the deposit.

4.3 DMA-APM Measurement

Before aerosol printing, the morphology and mass density of the NC agglomerates were characterized by tandem aerosol measurements.[21-22] The aerosol first flowed through a bipolar charger with a radioactive source (Po-210). The aerosolized NCl agglomerates with desired mobility diameter (d_m) were then classified by a differential mobility analyzer (DMA). The mass of the agglomerates (m) with a specific size was finally measured by an aerosol particle mass analyzer (APM).

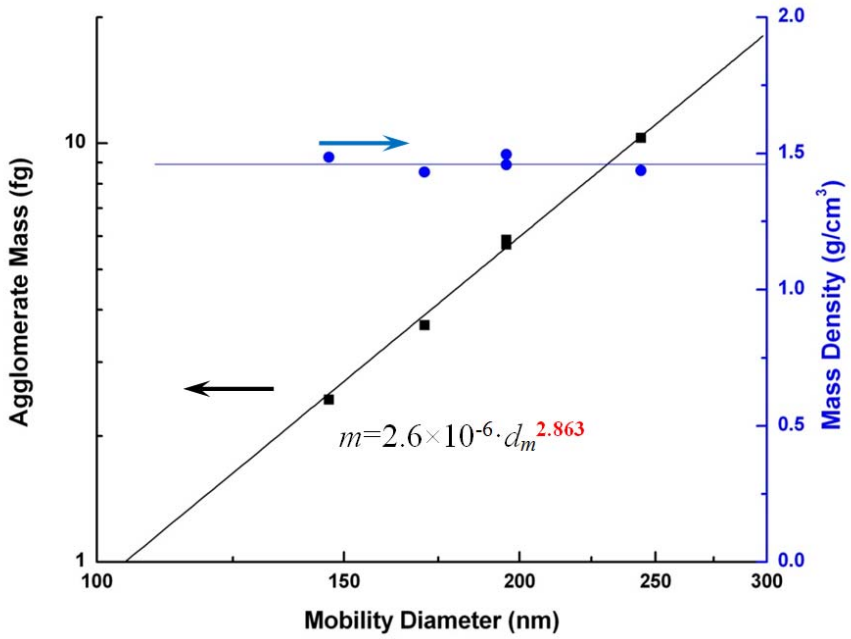

Figure 4-2. The relationship between mass and mobility diameter of the nanocrystal agglomerates (■), and the relationship between the mass density and the mobility diameter of the agglomerates (●).

Figure 4-2 plots the mass vs. mobility diameter data on a log-log scale. A straight line with a slope of 2.863 well fits the data points, indicating the agglomerates are

compact and close to spherical.[23] The mass densities of the compact and spherical agglomerates of different sizes were then calculated. As shown in Figure 4-2, the average mass density of the agglomerates is about 1.48 g/cm^3. The mass density of agglomerates is close for different mobility diameters, indicating that the composition of NC agglomerates with different sizes should also be consistent.

4.4 Effect of Agglomerate Size

As the building blocks of a printed NC film, the deposited individual agglomerate has to be a single monolayer thick, to obtain a single monolayer film of NCs. Meanwhile, the thickness of impacted agglomerates strongly depends on the number of NCs the agglomerate contains, or equivalently the agglomerate size (section 3.6). Thus, the dependence of the deposit morphology on the agglomerate size was investigated by printing monodisperse agglomerates sized by a differential mobility analyzer (DMA). Figure 4-3 exhibits TEM images of impacted NC agglomerates with mobility diameters selected by the DMA, which are similar to the STEM images in Figure 3-7b. A circular shaped deposit was obtained for all cases. When the agglomerate size is smaller than ~ 60 nm, the deposit is single monolayer thick. As the size increases to 90 nm, a multiple layer region appears at the center with monolayer skirts around. When the size further increases to 300 nm and beyond, a corona ring forms around the edge of the deposits, which is the characteristic sign of splashing. Therefore, agglomerate size should be less than 60 nm, to deposit a single monolayer. If thicker films are needed, agglomerates of 60-300 nm in diameter will be deposited.

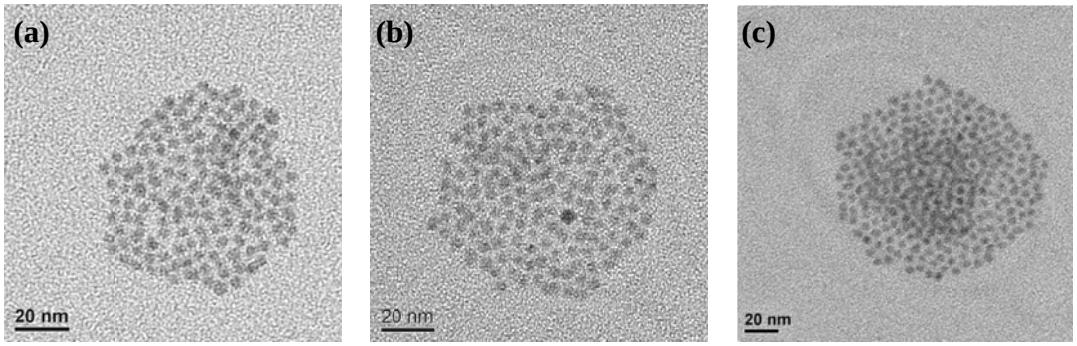

d_m = 40 nm d_m = 55 nm d_m = 90 nm

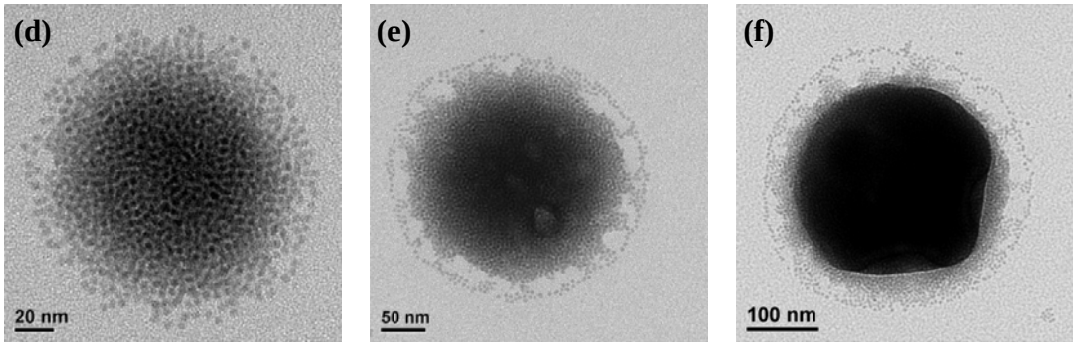

d_m = 300 d_m > 300 d_m >> 300 nm

Figure 4-3. TEM images of deposited nanocrystal agglomerates with mobility diameters of (a) 40 nm, (b) 55 nm, (c) 90 nm, (d) 300 nm, (e) > 300 nm, and (f) >> 300 nm, respectively. The agglomerates were deposited on carbon film substrates.

4.5 Ultrathin Nanocrystal Film Printing

Deposits with controlled morphologies were deposited using mobility classified particles of known size and with the substrate translated at a known speed relative to the beam. Agglomerates having mobility diameters of 40-nm were chosen to deposit a single monolayer NC films. When the substrate was translated at the speed of 80 μm/s, "pancakes" of monolayer NCs were scattered on the substrate (Figure 4-4a). The sizes of the deposits were very close to each other. When the translation speed of the substrate was reduced to 10 μm/s, a monolayer NC film with about 80% coverage was obtained (Figure 4-4b). Again, no sign of the boundaries between overlapped agglomerate deposits was obvious, indicating complete coalescence of the printed agglomerates. When the translation was further reduced to 5 μm/s, 100% coverage of single monolayer deposits was achieved (Figure 4-4c). A few multi-layer islands appeared in the deposit.

Lines produced from mobility-classified agglomerates of 100 nm contained multiple layers of NCs when the substrate was translated at 40 μm/s (Figure 4-5a).The central region of the microline was fully covered by NCs with multiple layers over most of the region (Figure 4-5b). Around the edges of the microline, the deposit became thinner and discontinuous (Figure 4-5c). The line width of major continuous portion of the microline is about 5 μm.

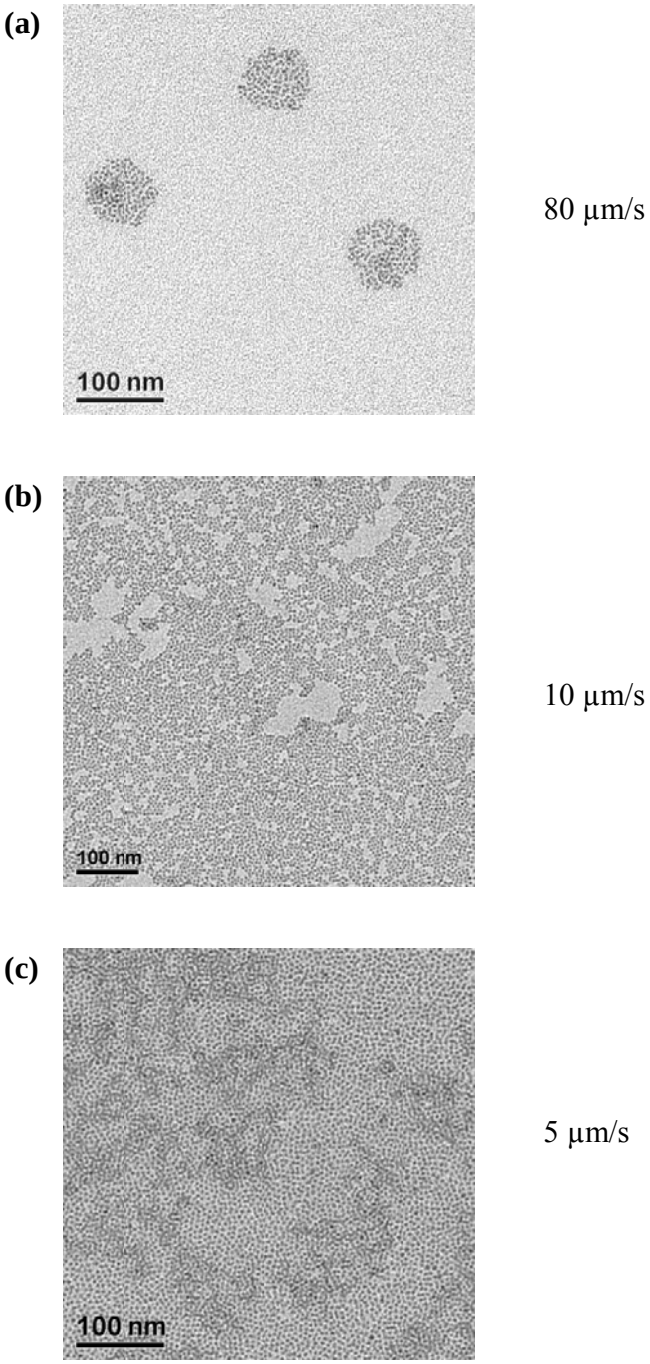

Figure 4-4. TEM images of deposits from 40-nm nanocrystal agglomerates. The carbon substrate was translated at velocities of (a) 80 μm/s, (b) 10 μm/s, and (c) 5 μm/s. The upstream pressure of the first lens was 1100 Pa and the chamber pressure was 1.5 Pa during deposition.

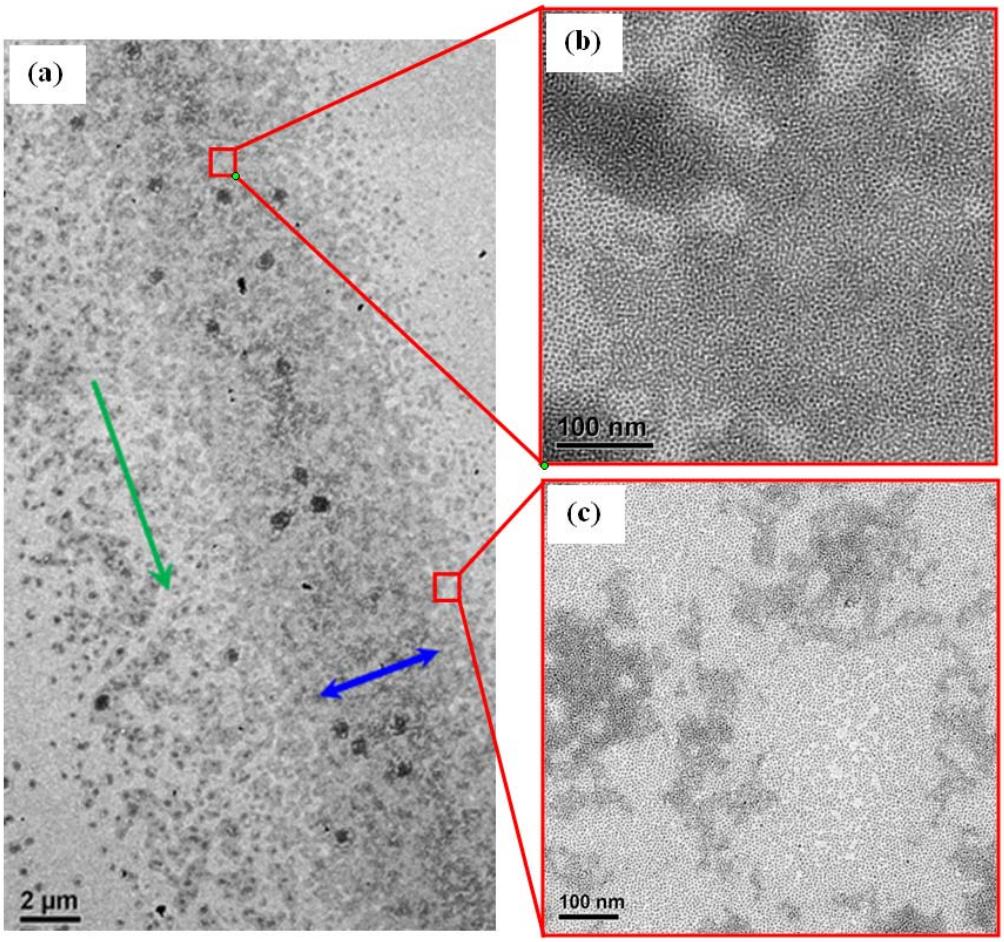

Figure 4-5. (a) TEM image of microline deposited from 100-nm nanocrystal agglomerates. The carbon substrate was translated at 40 µm/s. The green arrow indicates the direction of substrate translation. The blue arrow defines the line width of the microline. The upstream pressure of the first lens was 1100 Pa and the chamber pressure was 1.5 Pa during deposition. Enlarged TEM images of selected areas in (a) are shown in (b) and (c).

4.6 Effect of Surface Wettability

Although the NCs within agglomerates were inorganic, they were capped by organic ligands and surrounded by free surfactants and organic residues from the solution. The aerosolized agglomerates hence tend to spread out on hydrophobic surfaces (*e.g.* carbon films) during impaction, as we have seen in the aforementioned results. However, there are also plenty of hydrophobic substrates utilized in the electronic and optoelectronic devices. A classic example is silicon wafer, which usually has a thin layer of silica atop due to the oxidation by the air. Thus, it is important to study the effect of surface wettability on the deposited film morphology.

Silica film (Silicon Monoxide Type-A grids, Ted Pella), a typical hydrophilic substrate, was used in this investigation. Under identical conditions, aerosolized NC agglomerates were aerodynamically focused and impacted. Images of individual deposited agglomerates with mobility diameters ranging from 55 to 100 nm are shown in Figure 4-6. There is no obvious difference between images of these deposits and those for agglomerates of similar sizes on carbon film substrates (Figure 4-3). Without signs of fracture or splash, all three deposits have a roughly circular shape. The deposit of 55-nm agglomerates are one monolayer thick. As the mobility size increases, multi-layer centers appear in Figure 4-6b and 4-6c. These results show that the surface wettability has little effect during high-velocity impaction of individual NC agglomerates.

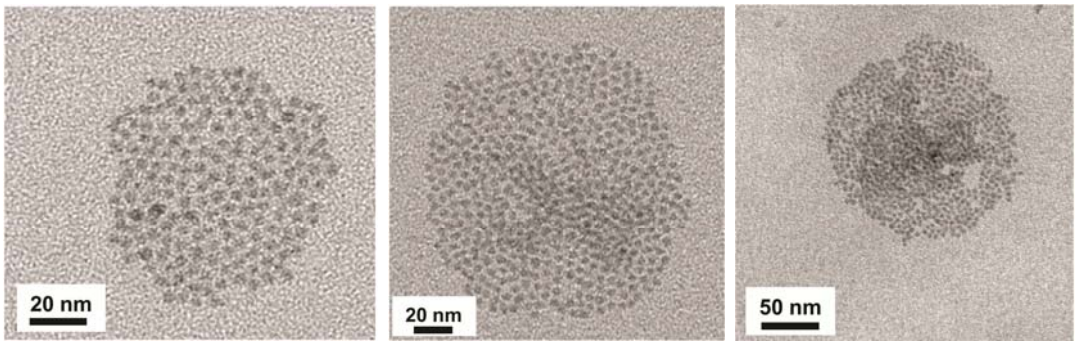

d_m = 55 nm d_m = 81 nm d_m = 100 nm

Figure 4-6. TEM images of deposited nanocrystal agglomerates on silica substrate. The mobility diameters of the agglomerates are (a) 55 nm, (b) 81 nm, and (c) 100 nm, respectively. The agglomerates were deposited at high velocity (~150 m/s).

On the other hand, we found that surface wettability significantly influenced the morphology of deposited NC films. Figure 4-7 compares the morphology of films deposited on carbon and silica substrates under identical experimental conditions. While NCs form single monolayers on the carbon film, they do not appear to spread as uniformly on the silica film, resulting in a poor coverage and islands of multi-layer NCs. No strong substrate effect was observed for individual agglomerate impaction. The dramatic change in the morphology of the deposited film implies that the hydrophilic silica film affects the degree to which overlapping NCs agglomerates undergo

reorganization after they deposit. To some extent, the overlapped agglomerates are likely to "shrink" due to their greater mobility on the silica substrate.

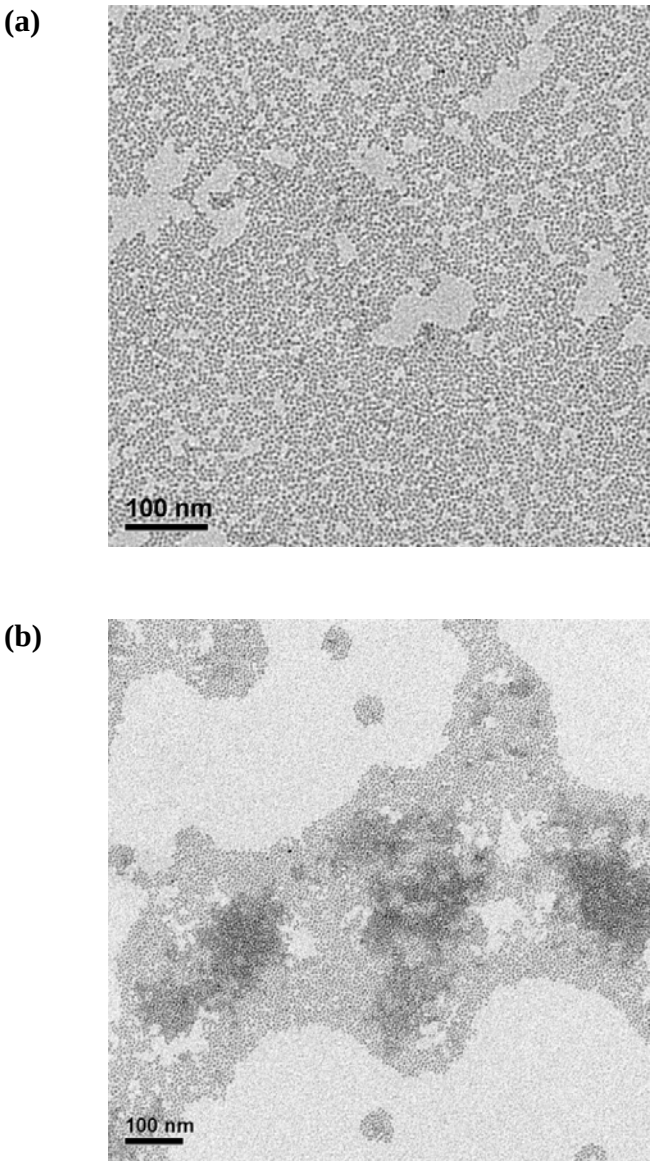

Figure 4-7. TEM images of printed NC films on (a) carbon film and (b) silica film under identical deposition conditions. The upstream pressure of the first lens was 1100 Pa and the chamber pressure was 1.5 Pa during deposition. The translation speed of the substrates was 10 μm/s.

4.7 Conclusion

We have demonstrated the performance of aerodynamic lenses in printing ultrathin NC films. It was found that the deposit morphology was strongly dependent on the mobility diameter of the aerosolized NC agglomerates. One monolayer thick NC films could be attained only when the size of the agglomerates was less than 60 nm. Translation velocity of the substrate also influences the coverage of the final deposit on the substrate. A single monolayer film was obtained by printing 40-nm NC agglomerates and translating the substrate at 10 μm/s. By focusing agglomerates of 100 nm in diameter, a 5 μm wide microline of multiple layered NCs was deposited on carbon substrate. By switching to silica substrate, the effect of surface wettability was also investigated. No obvious effect was observed for individually deposited agglomerates. However, the morphology of overlapped agglomerates was clearly different for carbon and silica substrates. Uniform and single monolayer NC films could no longer form as the agglomerates seemed unlikely to spread out on hydrophilic surfaces. This result indicates that, like other solution based coating methods,[17] the surface wettability controls the morphology of NC films deposited with aerodynamic lenses.

4.8 References

(1) Murray, C. B.; Kagan, C. R.; Bawendi, M. G., *Annual Review of Materials Science* **2000,** *30*, 545-610.

(2) Talapin, D. V.; Lee, J.-S.; Kovalenko, M. V.; Shevchenko, E. V., *Chemical Reviews* **2009,** *110*, 389-458.

(3) Colvin, V. L.; Schlamp, M. C.; Alivisatos, A. P., *Nature* **1994,** *370*, 354-357.

(4) Steckel, J. S.; Snee, P.; Coe-Sullivan, S.; Zimmer, J. P.; Halpert, J. E.; Anikeeva, P.; Kim, L.-A.; Bulovic, V.; Bawendi, M. G., *Angewandte Chemie International Edition* **2006,** *45*, 5796-5799.

(5) Sun, Q.; Wang, Y. A.; Li, L. S.; Wang, D.; Zhu, T.; Xu, J.; Yang, C.; Li, Y., *Nature Photonics* **2007,** *1*, 717-722.

(6) Zhu, T.; Shanmugasundaram, K.; Price, S. C.; Ruzyllo, J.; Zhang, F.; Xu, J.; Mohney, S. E.; Zhang, Q.; Wang, A. Y., *Applied Physics Letters* **2008,** *92*, 023111.

(7) Böberl, M.; Kovalenko, M. V.; Gamerith, S.; List, E. J. W.; Heiss, W., *Advanced Materials* **2007,** *19*, 3574-3578.

(8) Konstantatos, G.; Howard, I.; Fischer, A.; Hoogland, S.; Clifford, J.; Klem, E.; Levina, L.; Sargent, E. H., *Nature* **2006,** *442*, 180-183.

(9) Oertel, D. C.; Bawendi, M. G.; Arango, A. C.; Bulovic, V., *Applied Physics Letters* **2005,** *87*, 213505-3.

(10) Gur, I.; Fromer, N. A.; Geier, M. L.; Alivisatos, A. P., *Science* **2005,** *310*, 462-465.

(11) Huynh, W. U.; Dittmer, J. J.; Alivisatos, A. P., *Science* **2002,** *295*, 2425-2427.

(12) Leschkies, K. S.; Divakar, R.; Basu, J.; Enache-Pommer, E.; Boercker, J. E.; Carter, C. B.; Kortshagen, U. R.; Norris, D. J.; Aydil, E. S., *Nano Letters* **2007,** *7*, 1793-1798.

(13) Liu, D.; Kamat, P. V., *The Journal of Physical Chemistry* **1993,** *97*, 10769-10773.

(14) Robel, I.; Subramanian, V.; Kuno, M.; Kamat, P. V., *Journal of the American Chemical Society* **2006,** *128*, 2385-2393.

(15) Law, M.; Luther, J. M.; Song, Q.; Hughes, B. K.; Perkins, C. L.; Nozik, A. J., *Journal of the American Chemical Society* **2008,** *130*, 5974-5985.

(16) Ridley, B. A.; Nivi, B.; Jacobson, J. M., *Science* **1999,** *286*, 746-749.

(17) Talapin, D. V.; Murray, C. B., *Science* **2005,** *310*, 86-89.

(18) Peng, Z. A.; Peng, X. G., *Journal of the American Chemical Society* **2001,** *123*, 183-184.

(19) Reiss, P.; Bleuse, J.; Pron, A., *Nano Letters* **2002,** *2*, 781-784.

(20) Qi, L.; McMurry, P. H.; Norris, D. J.; Girshick, S. L., *Aerosol Science and Technology* **2010,** *44*, 55 - 60.

(21) Park, K.; Kittelson, D.; McMurry, P., *Aerosol Science and Technology* **2004,** *38*, 881 - 889.

(22) Scheckman, J. H.; McMurry, P. H.; Pratsinis, S. E., *Langmuir* **2009,** *25*, 8248-8254.

(23) Mandelbrot, B. B., *The Fractal Geometry of Nature*. Freemann: San Francisco, 1982.

5

Micropattern Deposition of Colloidal Nanocrystals by Aerodynamic Focusing[*]

In this chapter, the use of aerodynamic lenses to deposit micropatterns of colloidal semiconductor nanocrystals will be demonstrated. CdSe and CdSe/ZnS core/shell nanocrystals, with core diameters of 4-5 nm, were dispersed in hexane and then nebulized to generate agglomerates a few tens of nm in diameter, consisting of hundreds of nanocrystals. These agglomerates were then focused aerodynamically by a lens system. Microscale towers, lines and patterns were deposited on thin sapphire plates and silicon wafers. The heights and widths of the deposits were adjustable by varying the experimental parameters. Line widths below 10 μm at full-width half-maximum are demonstrated. Upon exposure to near-UV illumination, these deposits exhibited robust

[*] Portions of this chapter were published in: L.J. Qi, P.H. McMurry, D.J. Norris, and S. L. Girshick, *Aerosol Science and Technology*, 2010,**44**, 55-60.

fluorescence in the visual, with the color depending on the diameter of the individual nanocrystal cores. A red shift of the photoluminescence peaks from the nanocrystal dispersion to the glassy solid deposits was also observed, which confirmed that the deposits consist of closely packed nanocrystals embedded in the organic matrices. This approach, which is not restricted to semiconductor nanocrystals, provides an alternative means for the deposition of microscale patterns of colloidal nanoparticles.

5.1 Introduction

Semiconductor nanocrystals (NCs) exhibit electrical and optical properties that are different from those of bulk materials. Because these properties can also be easily tailored through choice of growth conditions, they are potentially useful for various optoelectronic devices, including light-emitting diodes,[1-2] photodetectors,[3-5] and solar cells.[6-10] For some of these devices, the deposition of NC assemblies with controlled patterns is an essential step in the fabrication process. Common methods include drop casting,[11] spin coating,[12-13] electrophoretic deposition,[14] and mist deposition.[15] Direct-write methods such as ink-jet printing[5, 16] are also attractive because they avoid mask screening, lithography, and pre-patterning of the substrate and can therefore simplify micropatterning and allow inexpensive and rapid prototyping.[17]

Here, we report the first use, to our knowledge, of aerodynamic lenses to deposit focused beams of fluorescent colloidal NCs that are aerosolized from liquid dispersions. A key aspect of this work is that we found that it was not necessary to produce aerosolized single NCs. Instead, we achieved deposition of fluorescent deposits, with

line widths of ~10 μm, by focusing NC agglomerates, where each agglomerate was a few tens of nm in diameter and contained a few hundred NCs. This approach avoids the potential problems noted above with regard to aerosolization and focusing of single, surface-passivated NCs, while producing a result that is likely superior from the application viewpoint, because of the narrower beam widths associated with aerodynamic focusing of particles that are a few tens of nm rather than a few nm in diameter. The resulting deposits exhibited robust fluorescence, demonstrating that this property survives the high-velocity impact, estimated at 400-500 m/s.

5.2 Experimental

Our process begins with luminescent, nearly monodisperse CdSe NCs synthesized according to standard methods.[18-19] To estimate the NC size, we used the lowest energy absorption peak.[20] On some of our CdSe samples, a thin ZnS shell was grown to increase their fluorescence efficiency to characterize the deposited patterns optically.[21] All of the NCs were capped with tri-*n*-octylphosphine oxide (TOPO) and dispersed in hexane. Before aerosolization, the number concentration was set to about 2×10^{13} NCs/cm^3 by adjusting the optical absorbance at 350 nm(see section 2.2.2 for details).[22-23] A Collison atomizer was then used to nebulize the NC dispersion (see section 2.3.1 for details). Helium gas was injected into the nebulizer at a pressure of 240 kPa to generate a continuous output of droplets about 3 μm in diameter, each of which contained ~300 NCs. After nebulization, the hexane quickly evaporated and the aerosol was fed through a

diffusion dryer filled with freshly activated carbon powder to remove the hexane vapor. After this process, agglomerates of NCs were obtained.

The size distribution of the agglomerates exiting the dryer was measured with a scanning mobility particle sizer (SMPS).[24-25] A typical size distribution that peaks at a diameter of 35 nm (see Figure 2-7). In other experiments, the peak diameter varied from 30 to 40 nm depending on the concentration of free TOPO in the solution and the NC size. The CdSe NCs, which were 3.5 nm in diameter in this case, account for ~30% of the agglomerate volume. The remaining ~70% is presumably occupied by the residue from the aerosolized solution, including free surfactants and nonvolatile impurities.

These aerosolized agglomerates were then passed through a pressure-limiting orifice (200 μm diameter) and flushed into the stainless steel aerodynamic lens assembly. The detailed principles of aerodynamic lenses were discussed previously by Liu *et al.*[26] As illustrated in Figure 5-1, the assembly consists of a series of center-collimated orifices, distributed in a tube, that create converging flow accelerations and diverging decelerations. Particles in the flow are inertially focused into a tight beam after passing through several orifices. The exit nozzle then accelerates them toward the substrate with minimized divergence angle. The pressure-limiting orifice controls the volumetric flow rate through the lens system, and the exit nozzle defines the lens operating pressure. Two important operating parameters, the pressure in front of the first lens and the pressure of the deposition chamber, are monitored respectively by pressure gauges P_1 and P_2 in Figure 5-1. The chamber is evacuated by a turbomolecular pump.

Using the Aerodynamic Lens Calculator [27] and assuming a mass density of 2.0 g/cm^3 for our agglomerates, we found that the lens assembly designed by Di Fonzo *et al.* was also suited to this study.[28] Each lens was 0.3 mm thick with an orifice diameter of 2.26 mm. The exit nozzle had an inner diameter of 1.85 mm and the barrel of the lens assembly was sealed by a system of double o-rings into the deposition chamber. Because our agglomerates were in a size regime where diffusion broadens the beam formed by the aerodynamic lenses, we selected helium as the carrier gas to lessen this effect.[29]

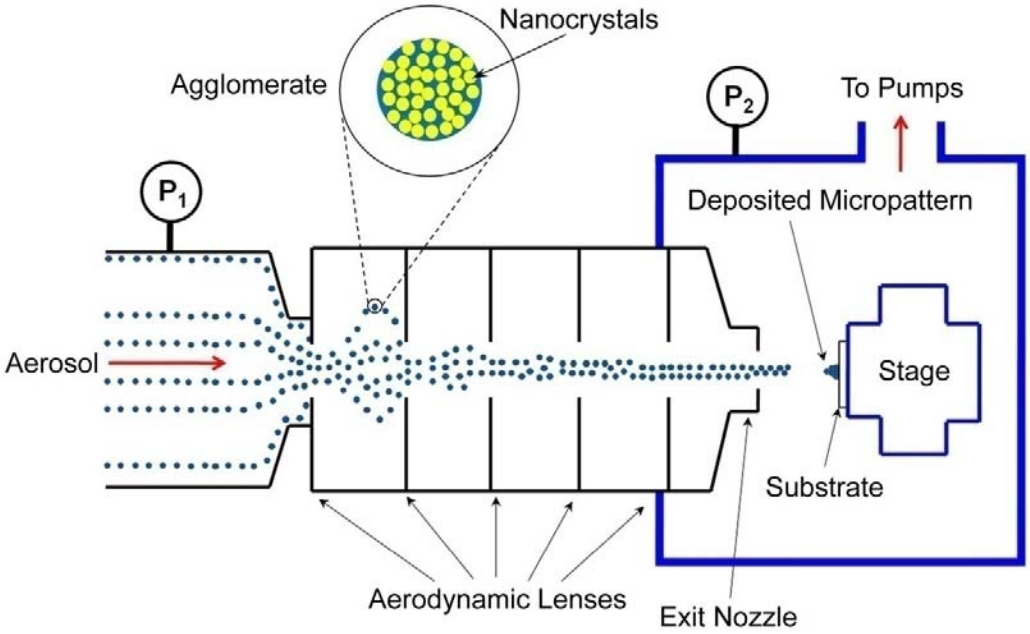

Figure 5-1. Schematic of the focused particle beam deposition system from ref. 30 (not to scale). Red lines indicate the direction of gas flow. The nanocrystal agglomerates from the nebulizer in Figure 1 enter the lens assembly through a pressure-limiting orifice. They then travel through a series of collimated orifices and an exit nozzle to yield a focused beam. The substrate, which is placed several millimeters downstream from the nozzle, is mounted on a motorized translation stage to allow pattern deposition. The pressures before the first lens (P_1) and in the deposition chamber (P_2) are monitored during the process. All depositions reported here were performed at room temperature.

5.3 Microtower Deposition

Figure 5-2 demonstrates a sharp microtower that we deposited on a thin sapphire plate from agglomerates of CdSe/ZnS core/shell NCs. The substrate was located 2 mm downstream from the exit nozzle and held stationary for 10 minutes. As seen in the scanning electron microscopy (SEM) image of Figure 5-2a, the deposit consists of a sharp peak with a surrounding circular area hereafter referred to as the "tail region". The microtower has a height of 158 μm with a full width at half maximum (FWHM) of 27 μm, indicating a height/FWHM ratio of 5.85. The same deposit was also imaged under ultraviolet illumination with a fluorescence microscope (Figure 5-2b). Yellow-green photoluminescence was observed, consistent with the 3.7-nm CdSe cores that were used. This also indicates that the individual NCs remained passivated by the surfactants despite the high impact velocity, estimated at 400-500 m/s, on the sapphire plate. Both the SEM and fluorescence measurements show that the diameter of the entire deposited area (including the tail region) is around 400 μm. Considering the possibility of motion or diffusion of the agglomerates along the substrate after impact, the width of the focused agglomerate beam was likely less than the 400-μm diameter of the deposit. Moreover, because the beam is significantly smaller than the inner diameter of the exit nozzle (1.85 mm) and very few of the agglomerates are expected to be lost in the lens assembly according to the Aerodynamic Lens Calculator, clogging of the nozzle is not an issue.

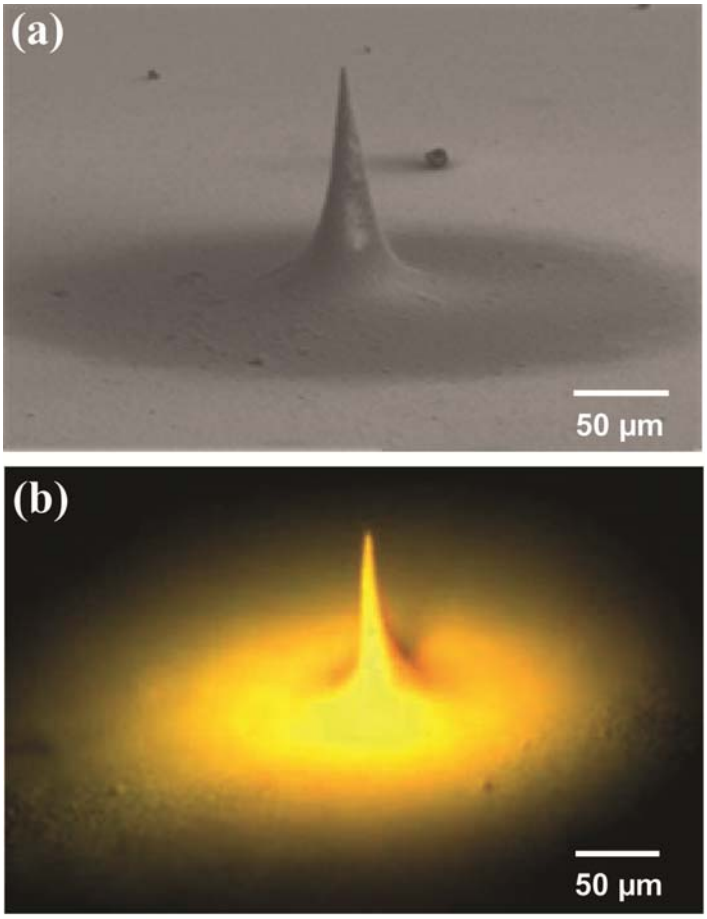

Figure 5-2. (a) SEM image of a microtower of CdSe/ZnS core/shell nanocrystals deposited on a sapphire substrate. P_1 was maintained at 1100 Pa and P_2 at 1.3 Pa during the ten minute deposition. (b) The fluorescence observed from the same microtower using a Leica MZ FLIII stereomicroscope with ultraviolet illumination near 400 nm. The CdSe cores had a diameter of 3.7 nm. The sample was coated with a gold layer of several nm to prevent charging during SEM after the fluorescence image was obtained.

5.4 Microline Deposition

To deposit patterns, the substrates were translated during deposition with a 3-axis computer-controlled motorized stage (Figure 5-1). While the speed of this stage was variable, for the depositions reported here we utilized a speed of 10 μm/s. Figure 5-3 shows a line deposited by scanning the stage back and forth five times across a silicon wafer. Similar lines were also formed on sapphire and glass substrates. After deposition, the substrate was fractured in liquid nitrogen. As seen in the SEM image of Figure 5-3a, with ten passes of the translation stage, the deposited line did not break with the substrate, resulting in a 130-μm-long cantilever suspended at the wafer edge. For this cantilever, only the central portion of the deposit remained; the surrounding thin tail region was removed with the substrate. The same effect was observed for lines deposited on glass slides. As with the microtower above, the line deposits also exhibited photoluminescence (Figure 5-3b).

The three-line pattern (Figure 5-4a) was deposited on a sapphire plate by translating the stage 6×600μm for each line at a velocity of 10 μm/second. When the substrate moved in a zig-zag motion at the same speed, we obtained an "M" pattern with a feature size less than 100 μm (Figure 5-4b). The line deposits show uniform and narrow wires along the translation direction.

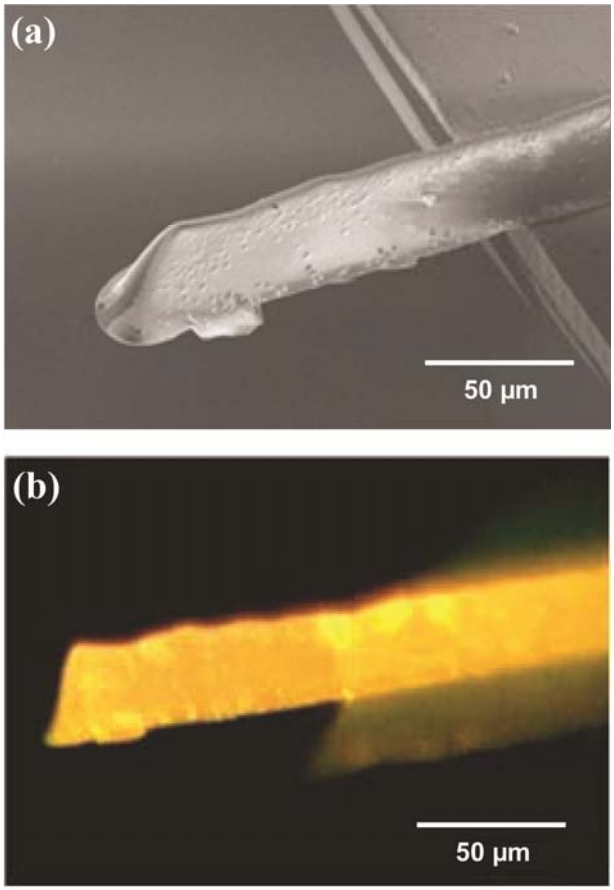

Figure 5-3. (a) SEM image of a line deposited from the same CdSe/ZnS core/shell nanocrystals used in Figure 4. The line was deposited on a 0.5-mm-thick silicon (100) wafer that was fractured in liquid nitrogen, leaving a freestanding portion of the line protruding past the edge of the wafer. The line was deposited by translating the substrate 5 times back and forth at a speed of 10 µm/s while maintaining P_1 at 1100 Pa and P_2 at 1.3 Pa. (b) A fluorescence image of the same deposit obtained as in Figure 5-2b.

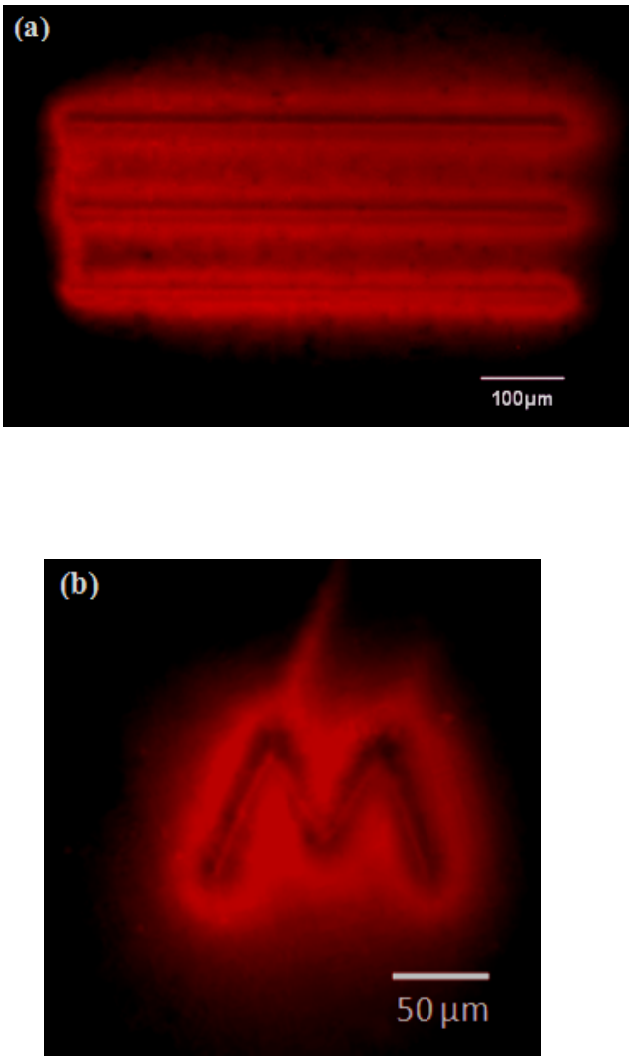

Figure 5-4. Fluorescent images of a three-line deposit (a) and an "M" pattern on sapphire thin plates under 400 nm ultraviolet excitation.

5.5 Self-sharpening of the Deposits

We also deposited lines with fewer passes of the translation stage. In this case, the deposits were thinner and cleaved with the substrate when we fractured the sample in liquid nitrogen. Thus, clean cross-sections could be obtained. Figure 5-5 shows cross-sectional SEM images of two lines deposited on thin glass slides. The conditions were identical except two deposition passes were used in Figure 5-5a, and six in Figure 5-5b. In both cases, the cross sections are seen to have a roughly triangular profile. For the two-pass line the height is 2.9 μm and the FWHM equals 9.4 μm, while for the six-pass line the height is 7.0 μm and the FWHM equals 7.5 μm. These results, as well as the microtower in Figure 5-2, illustrate the "self-sharpening" nature of focused particle beam deposition, which is similar to the arching effect of granular materials and reflects the granular nature of the deposited nanocrystal assembly.[31] The particle concentration in the focused beam at the nozzle exit is axisymmetrically Gaussian-distributed along the radial direction [32], resulting in the triangular cross sections seen in Figure 5-4.

5.6 Photoluminescence Spectroscopy Characterization

Figure 5-5 also indicates that the NCs are densely packed in the deposits without signs of porosity, at least at the resolution of the images. This is also consistent with photoluminescence spectra measured for the tower and line deposits from Figures 5-2 and 5-3. The maximum of the fluorescence was observed at 569 nm, while fluorescence from the same NCs peaked at 565 nm when they were dispersed in hexane (see Figure 5-6). The 4-nm red shift in the deposits is consistent with previous measurements on quantum

dot solids.[33] Hence, we conclude that our tower and line deposits are solids consisting of closely packed NCs in an organic matrix. (Because this matrix is not conductive, charging effects unfortunately made it impossible to obtain SEM images of the deposits at higher magnification than the images shown in Fig. 6.) The coincidence of the photoluminescence peaks in both the towers and lines also implies that the properties of the deposit are not dependent on their shape.

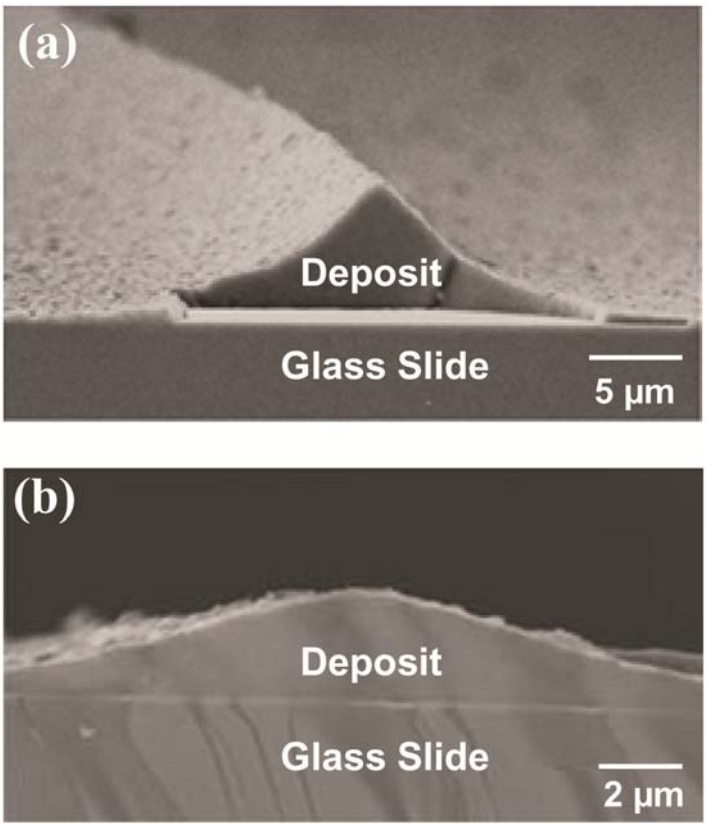

Figure 5-5. SEM cross-sectional images of lines deposited from 5 nm CdSe nanocrystals on thin glass slides. The substrate was passed (a) two and (b) six times through the beam at a speed of 10 μm/s while maintaining P_1 at 1100 Pa and P_2 at 1.3 Pa. The cross sections were obtained by fracturing the substrate perpendicular to the line in liquid nitrogen.

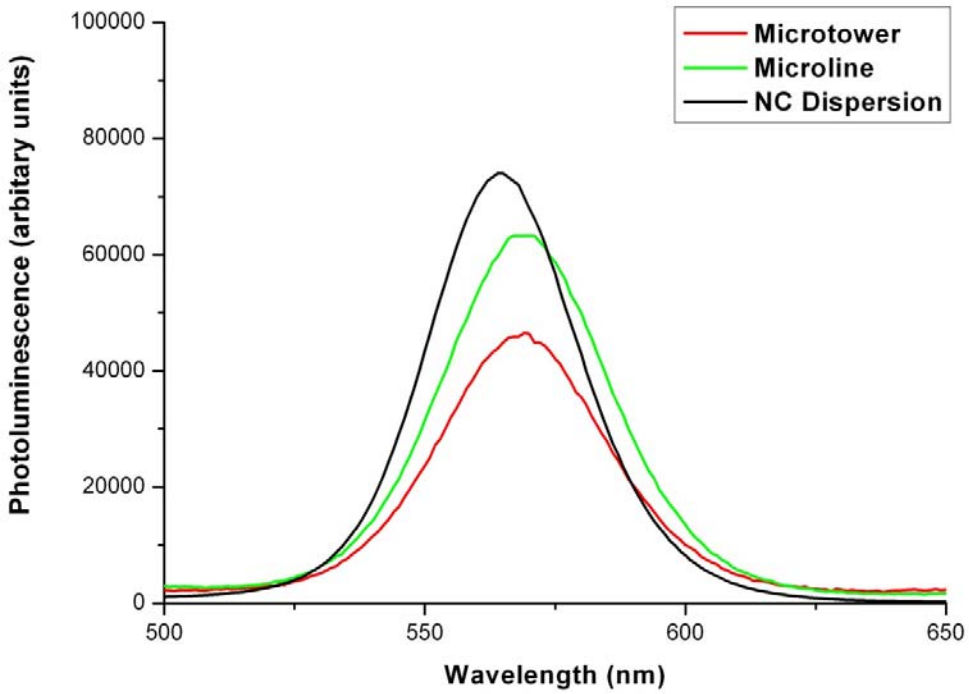

Figure 5-6. Photoluminescence spectra of the CdSe/ZnS core/shell NC dispersion in hexane, microtower and line deposits. The excitation light wavelength was 400 nm.

5.7 Summary

We have introduced a new method for fabricating NC micropatterns on various substrates from colloidal dispersions, based on the use of aerodynamic lenses that produce focused particle beams consisting of NC agglomerates from the nebulized dispersion. Because the sizes of the lens orifices and exit nozzle are in the millimeter range, they are easy to fabricate and can be more reliable than microscale nozzles or

capillaries. We used this approach to demonstrate the fabrication of fluorescent microscale towers and lines on various substrates. FWHM line widths of less than 10 μm were obtained for the deposits, depending on the deposition conditions. The deposits exhibit robust fluorescence, indicating that the NCs remain capped by passivating surfactant throughout the process of atomization and high velocity (~400-500 m/s) impact. Our results are consistent with the deposition of glassy solids of closely packed NCs in an organic matrix.

The ability to pattern fluorescent NCs at specific locations can potentially have applications in creating active areas for devices such as light-emitting diodes or thin-film transistors. While we focused here on semiconductor NCs, our approach is generally applicable and should allow a variety of colloidal nanoparticles to be deposited. Thus, wires of conductive channels consisting of metallic nanoparticles could also be patterned and combined with semiconductor deposits.

5.8 Acknowledgement

This work was supported by the NSF Nanoscale Interdisciplinary Research Team (NIRT) program (CBET-0506748) and utilized resources at the University of Minnesota Characterization Facility, funded by NSF through the NNIN program. D.J.N. benefited from financial support from the Alexander von Humboldt Foundation. We thank K. Iida, R. Mukherjee, M. R. Stolzenburg, and X. L. Wang for helpful discussion and assistance.

Coauthors of this article are coinventors on the following US Patents pertinent to the design and application of aerodynamic lenses: 5,270,542, 5,874,134, 6,924,004, 7,476,851.

5.9 References

(1) Colvin, V. L.; Schlamp, M. C.; Alivisatos, A. P., *Nature* **1994,** *370*, 354-357.

(2) Steckel, J. S.; Coe-Sullivan, S.; Bulovic, V.; Bawendi, M. G., *Adv. Mater.* **2003,** *15*, 1862-1866.

(3) Oertel, D. C.; Bawendi, M. G.; Arango, A. C.; Bulovic, V., *Appl. Phys. Lett.* **2005,** *87*, 213505.

(4) Konstantatos, G.; Howard, I.; Fischer, A.; Hoogland, S.; Clifford, J.; Klem, E.; Levina, L.; Sargent, E. H., *Nature* **2006,** *442*, 180-183.

(5) Böberl, M.; Kovalenko, M. V.; Gamerith, S.; List, E. J. W.; Heiss, W., *Adv. Mater.* **2007,** *19*, 3574-3578.

(6) Liu, D.; Kamat, P. V., *J. Phys. Chem.* **1993,** *97*, 10769-10773.

(7) Huynh, W. U.; Dittmer, J. J.; Alivisatos, A. P., *Science* **2002,** *295*, 2425-2427.

(8) Gur, I.; Fromer, N. A.; Geier, M. L.; Alivisatos, A. P., *Science* **2005,** *310*, 462-465.

(9) Robel, I.; Subramanian, V.; Kuno, M.; Kamat, P. V., *J. Am. Chem. Soc.* **2006,** *128*, 2385-2393.

(10) Leschkies, K. S.; Divakar, R.; Basu, J.; Enache-Pommer, E.; Boercker, J. E.; Carter, C. B.; Kortshagen, U. R.; Norris, D. J.; Aydil, E. S., *Nano Lett.* **2007,** *7*, 1793-1798.

(11) Murray, C. B.; Sun, S. H.; Gaschler, W.; Doyle, H.; Betley, T. A.; Kagan, C. R., *IBM J. Res. Dev.* **2001,** *45*, 47-56.

(12) Finlayson, C. E.; Ginger, D. S.; Greenham, N. C., *Appl. Phys. Lett.* **2000,** *77*, 2500-2502.

(13) Snee, P. T.; Chan, Y. H.; Nocera, D. G.; Bawendi, M. G., *Adv. Mater.* **2005,** *17*, 1131-1136.

(14) Islam, M. A.; Herman, I. P., *Appl. Phys. Lett.* **2002,** *80*, 3823-3825.

(15) Zhu, T.; Shanmugasundaram, K.; Price, S. C.; Ruzyllo, J.; Zhang, F.; Xu, J.; Mohney, S. E.; Zhang, Q.; Wang, A. Y., *Appl. Phys. Lett.* **2008,** *92*, 3.

(16) Tekin, E.; Smith, P. J.; Hoeppener, S.; van den Berg, A. M. J.; Susha, A. S.; Rogach, A. L.; Feldmann, J.; Schubert, U. S., *Adv. Funct. Mater.* **2007,** *17*, 23-28.

(17) Chrisey, D. B., *Science* **2000,** *289*, 879-881.

(18) Peng, Z. A.; Peng, X. G., *J. Am. Chem. Soc.* **2001,** *123*, 183-184.

(19) Reiss, P.; Bleuse, J.; Pron, A., *Nano Lett.* **2002,** *2*, 781-784.

(20) Yu, W. W.; Qu, L. H.; Guo, W. Z.; Peng, X. G., *Chem. Mater.* **2003,** *15*, 2854-2860.

(21) Hines, M. A.; Guyot-Sionnest, P., *J. Phys. Chem.* **1996,** *100*, 468-471.

(22) Klimov, V. I.; McBranch, D. W.; Leatherdale, C. A.; Bawendi, M. G., *Phys. Rev. B* **1999,** *60*, 13740-13749.

(23) Leatherdale, C. A.; Woo, W. K.; Mikulec, F. V.; Bawendi, M. G., *The Journal of Physical Chemistry B* **2002,** *106*, 7619-7622.

(24) Wang, S. C.; Flagan, R. C., *Aerosol Sci. Technol.* **1990,** *13*, 230-240.

(25) McMurry, P. H., *Atmos. Environ.* **2000,** *34*, 1959-1999.

(26) Liu, P., Ziemann, P. J.,Kittelson, D. B. and McMurry, P. H., *Aerosol Science and Technology* **1995,** *22*, 293-313.

(27) Wang, X. L.; McMurry, P. H., *Aerosol Science and Technology* **2006,** *40*, 320-334.

(28) Di Fonzo, F.; Gidwani, A.; Fan, M. H.; Neumann, D.; Iordanoglou, D. I.; Heberlein, J. V. R.; McMurry, P. H.; Girshick, S. L.; Tymiak, N.; Gerberich, W. W.; Rao, N. P., *Applied Physics Letters* **2000,** *77*, 910-912.

(29) Wang, X. L.; Kruis, F. E.; McMurry, P. H., *Aerosol Sci. Technol.* **2005,** *39*, 611-623.

(30) Qi, L.; McMurry, P. H.; Norris, D. J.; Girshick, S. L., *Aerosol Science and Technology* **2010,** *44*, 55 - 60.

(31) Duran, J., *Sands, Powders, and Grains: An Introduction to the Physics of Granular Materials*. Springer-Verlag: New York, 2000.

(32) Liu, P.; J., Z. P.; B., K. D.; McMurry, P. H., *Aerosol Sci. Technol.* **1995,** *22*, 293-313.

(33) Kagan, C. R.; Murray, C. B.; Bawendi, M. G., *Phys. Rev. B* **1996,** *54*, 8633-8643.

6

Summary and Future Work

6.1 Summary of the Thesis

This thesis research presents a systematic attempt to print colloidal semiconductor NCs by aerodynamic focusing. While aerodynamic focusing has been demonstrated for particles down to 3 nm in diameter,[1] the d_p^{-2} dependence of Brownian diffusion coefficients, where d_p is particle diameter, causes particle beam widths to increase as particle diameter decreases, particularly in the sub-10-nm diameter regime. The other issue is that atomizing NC colloids to generate an aerosol consisting of single NCs may be prohibitively difficult, particularly if one considers that each NC must remain capped by a passivating surfactant.[2] A key aspect of this work is that we found that it was not necessary to produce aerosolized single NCs. By focusing aerosolized NC agglomerates a few tens of nm in diameter, we are able to efficiently direct-write micropatterns of NCs

with thickness ranging from a single monolayer up to several microns on carbon substrates.

This thesis research starts with a detailed investigation of impact dynamics of individual aerosolized NC agglomerates, the building blocks of NC film printing. The results of aerosol characterization on the agglomerates reveal that agglomerates aerosolized from colloidal dispersions in hexane are compact and close to spherical. The cohesive interaction between the NCs inside the agglomerates could be adjusted by altering number concentration of colloidal NC dispersion. The higher the concentration, the stronger the cohesion between the NCs. Mildly cohesive agglomerates from relatively dilute dispersions behaved like viscous liquids during impact deformation. NCs of overlapped agglomerate deposits could coalesce and form a continuous structure. The granular nature of the NCs in the agglomerates was also revealed through quantitative analysis of STEM images of the impact deformed agglomerates.

Advancing with the knowledge of the cohesive granular properties of aerosolized NC agglomerates, we found a strong dependence of the deposit thickness on the individual agglomerate size, as a result of the granular property of the NC agglomerates. A single monolayer NC film was obtained by focusing monodisperse 40-nm NC agglomerates and translating the carbon substrate at a velocity of 10 μm/s, while a multi-layer microline of NCs was printed by depositing 100-nm NC agglomerates and translating the substrate at 40 μm/s. A strong effect of substrate surface wettability on the printed film formation was also observed, indicating additional surface treatment had to be done on the hydrophilic substrate prior to aerosol printing of colloidal semiconductor NCs.

By aerodynamically focusing polydisperse NC agglomerates, microscale towers, lines, and patterns were printed on thin sapphire plates and silicon wafers. The thickness and width of the deposits were adjustable by varying experimental conditions. Micropatterns of NCs with line width less than 10 μm were demonstrated. The printed NCs exhibited robust fluorescence under near-UV illumination. The optical spectroscopic measurements confirmed that the printed micropatterns consist of closely packed NCs embedded in the organic matrices.

6.2 Recommendations for Future Work

1. **Device fabrication.** A straightforward step beyond this thesis research is to fabricate a NC-based device by aerosol printing with aerodynamic lenses. A simple structured photodetector based on CdSe NCs is recommended, which has been successfully made using the contact printing method.[3] The heterojunction photodetector of lateral geometry requires a CdSe NC pattern of ~ 50 nm thick and several tens of microns wide atop of a conducting organic layer.[3] It is promising to utilize the aerodynamic lens assembly used in this thesis research (section 2.4.2) and print the desired CdSe NC pattern of the photodetector.

2. **Numerical simulation.** Although classical molecular dynamics (MD) simulation has succeeded in modeling high-velocity impact deformation of silicon nanoparticles,[4-5] the difficulty in finding appropriate mechanisms of energy dissipation limits its application in simulating the deformation process of

impacted NC agglomerates. On the other hand, molecular simulations of the interactions between capped NCs have been well developed, especially for the system of Au particles and thiol ligands.[6-8] Quantitative information related to the interaction between the Au NCs can be used for reference to simulate interaction between the CdSe NCs capped by TOPO, which make it possible to simulate the deformation process of impacted NC agglomerates by discrete element modeling (DEM).[9] As we already have enough information for DEM simulation, such as NC size and density, number of NCs in an agglomerate, and the interaction between NCs, it seems promising to reproduce the morphologies of deformed NC agglomerates by DEM.[10] The simulation results may help further understand the deformation process of impacted NC agglomerates (*e.g.* the formation of envelope ring for large liquid-like agglomerates during high-velocity impaction).

3. **Printing NC-polymer composites.** The incorporation of semiconductor NCs into polymer networks is an important strategy to achieve better performance of the NC-based devices since it allows combining the desirable properties of NCs and polymers.[11] NCs have been dispersed into different polymer matrices by various methods, among which direct blending of NCs and polymers is the simplest way and is compatible with the solution-based fabrication process. Displays based on blends of CdSe NCs and polyisobutylene (PIB) polymers,[12] and hybrid solar cells based on composite of Si NCs and poly-3(hexylthiophene) (P3HT) polymers,[13] have been reported. However, mixing NCs and polymers

into a uniform composite film is still challenging, because of the phase separation of NCs and polymers,[13] and the coffee ring effect during the solvent evaporation.[14-15] Moreover, it was reported that CdTe NCs were incorporated into poly(vinyl alcohol) (PVA) solid nanofibers by electrospinning with volatile solvents.[16] It was found that fast evaporation rate of the solvent could quickly freeze the polymer chains, resulting in the local confinement of the CdTe NCs without enough time to aggregate.[16] This report suggests that it is promising to produce uniform films and patterns of NC and polymer blends by the aerosol printing approach developed in this thesis research. By atomizing the dispersions containing NCs and polymers, aerosol composite particles of NC-polymer blends could be obtained and then printed on substrates by aerodynamic focusing. As the dispersion is broken into tiny droplets during nebulization, the scale of possible phase separation will be controlled by the droplet size. The utilization of volatile solvent (*e.g.* hexane) may further suppress the phase separation and lead to the deposition of uniform composite films of NCs and polymers.

6.3 References

(1) Wang, X. L.; McMurry, P. H., *International Journal of Mass Spectrometry* **2006,** *258*, 30-36.

(2) Klimov, V. I.; McBranch, D. W.; Leatherdale, C. A.; Bawendi, M. G., *Physical Review B* **1999,** *60*, 13740-13749.

(3) Osedach, T. P.; Geyer, S. M.; Ho, J. C.; Arango, A. C.; Bawendi, M. G.; Bulovic, V., *Applied Physics Letters* **2009,** *94*, 043307-3.

(4) Valentini, P.; Gerberich, W. W.; Dumitrică, T., *Physical Review Letters* **2007,** *99*, 175701.

(5) Suri, M.; Dumitrică, T., *Physical Review B* **2008,** *78*, 081405.

(6) Luedtke, W. D.; Landman, U., *The Journal of Physical Chemistry B* **1998,** *102*, 6566-6572.

(7) Landman, U.; Luedtke, W. D., *Faraday Discussions* **2004,** *125*, 1-22.

(8) Schapotschnikow, P.; Pool, R.; Vlugt, T. J. H., *Nano Letters* **2008,** *8*, 2930-2934.

(9) Potyondy, D. O.; Cundall, P. A., *International Journal of Rock Mechanics and Mining Sciences* **2004,** *41*, 1329-1364.

(10) *Particle Flow Code in 3-Dimensions (PFC^{3D}), Version 3.1 Manuals*. Itasca Consulting Group: Minneapolis, MN, USA, 2005.

(11) Zhang, H.; Han, J.; Yang, B., *Advanced Functional Materials* **2010,** *20*, 1533-1550.

(12) Wood, V.; Panzer, M. J.; Chen, J.; Bradley, M. S.; Halpert, J. E.; Bawendi, M. G.; Bulovi, V.; cacute. *Advanced Materials* **2009,** *21*, 2151-2155.

(13) Liu, C.-Y.; Holman, Z. C.; Kortshagen, U. R., *Nano Letters* **2008,** *9*, 449-452.

(14) Deegan, R. D.; Bakajin, O.; Dupont, T. F.; Huber, G.; Nagel, S. R.; Witten, T. A., *Nature* **1997,** *389*, 827-829.

(15) Tekin, E.; Smith, P. J.; Hoeppener, S.; van den Berg, A. M. J.; Susha, A. S.; Rogach, A. L.; Feldmann, J.; Schubert, U. S., *Advanced Functional Materials* **2007,** *17*, 23-28.

(16) Li, M.; Zhang, J.; Zhang, H.; Liu, Y.; Wang, C.; Xu, X.; Tang, Y.; Yang, B., *Advanced Functional Materials* **2007,** *17*, 3650-3656.

Bibliography

Aldana, J., Wang, Y. A. and Peng, X. (2001). "Photochemical Instability of CdSe Nanocrystals Coated by Hydrophilic Thiols". *Journal of the American Chemical Society* 123:8844-8850.

Bayvel, L. P. and Orzechowski, Z. (1993). *Liquid Atomization*. Taylor & Francis, Washington D.C., USA.

Böberl, M., Kovalenko, M. V., Gamerith, S., List, E. J. W. and Heiss, W. (2007). "Inkjet-Printed Nanocrystal Photodetectors Operating up to 3 μm Wavelengths". *Advanced Materials* 19:3574-3578.

Brus, L. E. (1984). "Electron-electron and Electron-hole Interactions in Small Semiconductor Crystallites-the Size Dependence of the Lowest Excited Electronic State". *Journal of Chemical Physics* 80:4403-4409.

Caruge, J. M., Halpert, J. E., Wood, V., Bulovic, V. and Bawendi, M. G. (2008). "Colloidal quantum-dot light-emitting diodes with metal-oxide charge transport layers". *Nature Photonics* 2:247-250.

Chandler, R. E., Houtepen, A. J., Nelson, J. and Vanmaekelbergh, D. (2007). "Electron Transport in Quantum Dot Solids: Monte Carlo Simulations of the Effects of Shell Filling, Coulomb Repulsions, and Site Disorder". *Phys. Rev. B* 75:085325.

Cheng, K.-Y., Anthony, R., Kortshagen, U. R. and Holmes, R. J. (2010). "Hybrid Silicon Nanocrystal−Organic Light-Emitting Devices for Infrared Electroluminescence". *Nano Letters* 10:1154-1157.

Chrisey, D. B. (2000). "Materials processing - The power of direct writing". *Science* 289:879-881.

Chu, M. Q., Wu, F., Zhang, Q., Liu, T. T., Yu, Y., Ji, A. L., Xu, K. Y., Feng, Z. H. and Zhu, J. (2010). "A novel method for preparing quantum dot nanospheres with narrow size distribution". *Nanoscale* 2:542-547.

Coe, S., Woo, W.-K., Bawendi, M. and Bulovic, V. (2002). "Electroluminescence from single monolayers of nanocrystals in molecular organic devices". *Nature* 420:800-803.

Colvin, V. L., Schlamp, M. C. and Alivisatos, A. P. (1994). "Light-emitting diodes made from cadmium selenide nanocrystals and a semiconducting polymer". *Nature* 370:354-357.

Deegan, R. D., Bakajin, O., Dupont, T. F., Huber, G., Nagel, S. R. and Witten, T. A. (1997). "Capillary flow as the cause of ring stains from dried liquid drops". *Nature* 389:827-829.

Deegan, R. D. (2000). "Pattern formation in drying drops". *Physical Review E* 61:475-485.

Di Fonzo, F., Gidwani, A., Fan, M. H., Neumann, D., Iordanoglou, D. I., Heberlein, J. V. R., McMurry, P. H., Girshick, S. L., Tymiak, N., Gerberich, W. W. and Rao, N. P. (2000). "Focused nanoparticle-beam deposition of patterned microstructures". *Applied Physics Letters* 77:910-912.

Dong, Y., A. Bapat, S. Hilchie, U. Kortshagen, and S. A. Campbell (2004). "Generation of nano-sized free standing single crystal silicon particles". *Journal of Vacuum Science and Technology B* 22:1923-1930.

Duran, J. (2000). *Sands, Powders, and Grains: An Introduction to the Physics of Granular Materials*. Springer-Verlag, New York.

Ehara, K., Hagwood, C. and Coakley, K. J. (1996). "Novel method to classify aerosol particles according to their mass-to-charge ratio--Aerosol particle mass analyser". *Journal of Aerosol Science* 27:217-234.

Emery, M. S. (2005). "Theoretical Analysis of Data from DMA-APM System", in *Mechanical Engineering*, University of Minnesota, Minneapolis.

Fernández-Feria, R., P. Riesco-Chueca, J. Rosell-Llompart, J. Fernández de la Mora, and and O'Brien, J. (1991). *Brownian Motion Limited Aerodynamic Focusing of Heavy Molecules*. Weinheim.

Fernández de la Mora, J., J. Rosell-Llompart, and P. Riesco-Chueca (1989). *Aerodynamic Focusing of Particles and Molecules in Seeded Supersonic Jets*. AIAA, Washington DC.

Finlayson, C. E., Ginger, D. S. and Greenham, N. C. (2000). "Optical Microcavities Using Highly Luminescent Films of Semiconductor Nanocrystals". *Applied Physics Letters* 77:2500-2502.

Frankel, F. and Bawendi, M. G *www.nanocluster.mit.edu*.

Gidwani, A. (2003). "Studies of Flow and Particle Transport in Hypersonic Plasma Particle Deposition and Aerodynamic Focusing", in *Department of Mechanical Engineering*, University of Minnesota, Minneapolis.

Gur, I., Fromer, N. A., Geier, M. L. and Alivisatos, A. P. (2005). "Air-stable all-inorganic nanocrystal solar cells processed from solution". *Science* 310:462-465.

Harrison, M. T., Kershaw, S. V., Burt, M. G., Rogach, A. L., Kornowski, A., Eychmüller, A. and Weller, H. (2000). "Colloidal nanocrystals for telecommunications. Complete coverage of the low-loss fiber windows by mercury telluride quantum dot". *Pure and Applied Chemistry* 72:295-307.

Hinds, W. C. (1999). *Aerosol Technology: Properties, Behavior, and Measurement of Airborne Particles*.

Hines, M. A. and Guyot-Sionnest, P. (1996). "Synthesis and Characterization of Strongly Luminescing ZnS-Capped CdSe Nanocrystals". *The Journal of Physical Chemistry* 100:468-471.

Houtepen, A. J. and Vanmaekelbergh, D. (2005). "Orbital Occupation in Electron-Charged CdSe Quantum-Dot Solids". *The Journal of Physial Chemistry B* 109:19634–19642.

Houtepen, A. J., Kockmann, D. and Vanmaekelbergh, D. (2008). "Reappraisal of Variable-Range Hopping in Quantum-Dot Solids". *Nano Lett.* 8:3516–3520.

Huynh, W. U., Dittmer, J. J. and Alivisatos, A. P. (2002). "Hybrid nanorod-polymer solar cells". *Science* 295:2425-2427.

Islam, M. A. and Herman, I. P. (2002). "Electrodeposition of Patterned CdSe Nanocrystal Films Using Thermally Charged Nanocrystals". *Applied Physics Letters* 80:3823-3825.

Jaeger, H. M., Nagel, S. R. and Behringer, R. P. (1996). "Granular solids, liquids, and gases". *Rev. Mod. Phys.* 68:1259-1273.

Jarosz, M. V., Porter, V. J., Fisher, B. R., Kastner, M. A. and Bawendi, M. G. (2004). "Photoconductivity studies of treated CdSe quantum dot films exhibiting increased exciton ionization efficiency". *Physical Review B* 70:195327.

Jayne, J. T., Leard, D. C., Zhang, X., Davidovits, P., Smith, K. A., Kolb, C. E. and Worsnop, D. R. (2000). "Development of an Aerosol Mass Spectrometer for Size and Composition Analysis of Submicron Particles". *Aerosol Science and Technology* 33:49 - 70.

Kagan, C. R., Murray, C. B. and Bawendi, M. G. (1996). "Long-range resonance transfer of electronic excitations in close-packed CdSe quantum-dot solids". *Physical Review B* 54:8633-8643.

Kanskaya, L. M., Kokhanovskii, S. I., Seisyan, R. P. and Efros, A. L. (1982). "Diamagnetic Excitons and Parameters of Energy of Energy-bands of InSb Crystals". *Soviet Physics Semiconductors-Ussr* 16:1315-1317.

Kim, D. J. and Koo, K. K. (2009). "Synthesis of Colloidal ZnSe Nanospheres by Ultrasonic-Assisted Aerosol Spray Pyrolysis". *Crystal Growth and Design* 9:1153-1157.

Kim, L., Anikeeva, P. O., Coe-Sullivan, S. A., Steckel, J. S., Bawendi, M. G. and Bulović, V. (2008). "Contact Printing of Quantum Dot Light-Emitting Devices". *Nano Letters* 8:4513-4517.

Klajn, R., Bishop, K. J. M., Fialkowski, M., Paszewski, M., Campbell, C. J., Gray, T. P. and Grzybowski, B. A. (2007). "Plastic and moldable metals by self-assembly of sticky nanoparticle aggregates". *Science* 316:261-264.

Klimov, V. I., McBranch, D. W., Leatherdale, C. A. and Bawendi, M. G. (1999). "Electron and Hole Relaxation Pathways in Semiconductor Quantum Dots". *Physical Review B* 60:13740-13749.

Klimov, V. I., Mikhailovsky, A. A., Xu, S., Malko, A., Hollingsworth, J. A., Leatherdale, C. A., Eisler, H.-J. and Bawendi, M. G. (2000). "Optical Gain and Stimulated Emission in Nanocrystal Quantum Dots". *Science* 290:314-317.

Klimov, V. I. (2006). "Mechanisms for Photogeneration and Recombination of Multiexcitons in Semiconductor Nanocrystals: Implications for Lasing and Solar Energy Conversion". *The Journal of Physical Chemistry B* 110:16827-16845.

Klimov, V. I., Ivanov, S. A., Nanda, J., Achermann, M., Bezel, I., McGuire, J. A. and Piryatinski, A. (2007). "Single-exciton optical gain in semiconductor nanocrystals". *Nature* 447:441-446.

Konstantatos, G., Howard, I., Fischer, A., Hoogland, S., Clifford, J., Klem, E., Levina, L. and Sargent, E. H. (2006). "Ultrasensitive solution-cast quantum dot photodetectors". *Nature* 442:180-183.

Konstantatos, G. and Sargent, E. H. (2007). "PbS colloidal quantum dot photoconductive photodetectors: Transport, traps, and gain". *Applied Physics Letters* 91:173505-173503.

Konstantatos, G., Levina, L., Fischer, A. and Sargent, E. H. (2008). "Engineering the Temporal Response of Photoconductive Photodetectors via Selective Introduction of Surface Trap States". *Nano Letters* 8:1446-1450.

Lakowicz, J. R. (2006). *Principles of Fluorescence Spectroscopy* Springer Science+Business Media, LLC, New York, NY, USA.

Landman, U. and Luedtke, W. D. (2004). "Small is different: energetic, structural, thermal, and mechanical properties of passivated nanocluster assemblies". *Faraday Discussions* 125:1-22.

Law, M., Luther, J. M., Song, Q., Hughes, B. K., Perkins, C. L. and Nozik, A. J. (2008). "Structural, Optical, and Electrical Properties of PbSe Nanocrystal Solids Treated Thermally or with Simple Amines". *Journal of the American Chemical Society* 130:5974-5985.

Leatherdale, C. A., Kagan, C. R., Morgan, N. Y., Empedocles, S. A., Kastner, M. A. and Bawendi, M. G. (2000). "Photoconductivity in CdSe quantum dot solids". *Physical Review B* 62:2669-2680.

Leatherdale, C. A., Woo, W. K., Mikulec, F. V. and Bawendi, M. G. (2002). "On the Absorption Cross Section of CdSe Nanocrystal Quantum Dots". *The Journal of Physical Chemistry B* 106:7619-7622.

Lee, D., Jia, S., Banerjee, S., Bevk, J., Herman, I. P. and Kysar, J. W. (2007). "Viscoplastic and Granular Behavior in Films of Colloidal Nanocrystals". *Physical Review Letters* 98:026103.

Lee, J.-W., M.-Y. Yi, and S.-M. Lee (2003). "Inertial Focusing of Particles with an Aerodynamic Lens in the Atmospheric Pressure Range". *Journal of Aerosol Science* 34:211-234.

Leschkies, K. S., Divakar, R., Basu, J., Enache-Pommer, E., Boercker, J. E., Carter, C. B., Kortshagen, U. R., Norris, D. J. and Aydil, E. S. (2007). "Photosensitization of ZnO Nanowires with CdSe Quantum Dots for Photovoltaic Devices". *Nano Letters* 7:1793-1798.

Li, M., Zhang, J., Zhang, H., Liu, Y., Wang, C., Xu, X., Tang, Y. and Yang, B. (2007). "Electrospinning: A Facile Method to Disperse Fluorescent Quantum Dots in Nanofibers without Förster Resonance Energy Transfer". *Advanced Functional Materials* 17:3650-3656.

Lim, J. A., Lee, W. H., Lee, H. S., Lee, J. H., Park, Y. D. and Cho, K. (2008). "Self-Organization of Ink-jet-Printed Triisopropylsilylethynyl Pentacene via Evaporation-Induced Flows in a Drying Droplet". *Advanced Functional Materials* 18:229-234.

Lin, Y., Skaff, H., Boker, A., Dinsmore, A. D., Emrick, T. and Russell, T. P. (2003). "Ultrathin cross-linked nanoparticle membranes". *Journal of the American Chemical Society* 125:12690-12691.

Liu, C.-Y., Holman, Z. C. and Kortshagen, U. R. (2008). "Hybrid Solar Cells from P3HT and Silicon Nanocrystals". *Nano Letters* 9:449-452.

Liu, D. and Kamat, P. V. (1993). "Photoelectrochemical Behavior of Thin CdSe and Coupled TiO_2 CdSe Semiconductor Films". *The Journal of Physical Chemistry* 97:10769-10773.

Liu, J. Y. (2005). "Scanning transmission electron microscopy and its application to the study of nanoparticles and nanoparticle systems". *Journal of Electron Microscopy* 54:251-278.

Liu, P., Ziemann, P. J.,Kittelson, D. B. and McMurry, P. H. (1995a). "Gernerting Particle Beams of Controlled Dimensions and Divergence.1. Theory of Particle Motion in Aerodynamic Lenses and Nozzle Expansions". *Aerosol Science and Technology* 22:293-313.

Liu, P., Ziemann, P. J., Kittelson, D. B. and McMurry, P. H. (1995b). "Generating Particle Beams of Controlled Dimensions and Divergence.2. Experimental Evaluation of Particle Motion in Aerodynamic Lenses and Nozzle Expansions". *Aerosol Science and Technology* 22:314-324.

Loeb, L. B. (1958). *Static Electrification* Springer-Verlag, Berlin, Germany.

Luedtke, W. D. and Landman, U. (1998). "Structure and Thermodynamics of Self-Assembled Monolayers on Gold Nanocrystallites". *The Journal of Physical Chemistry B* 102:6566-6572.

Mandelbrot, B. B. (1982). *The Fractal Geometry of Nature*. Freemann, San Francisco.

McMurry, P. H. (2000). "A Review of Atmospheric Aerosol Measurements". *Atmospheric Environment* 34:1959-1999.

Mette, A., Richter, P. L., Hörteis, M. and Glunz, S. W. (2007). "Metal Aerosol Jet Printing for Solar Cell Metallization". *Progress in Photovoltaics: Research and Applications* 15:621-627.

Mueggenburg, K. E., Lin, X. M., Goldsmith, R. H. and Jaeger, H. M. (2007). "Elastic membranes of close-packed nanoparticle arrays". *Nature Materials* 6:656-660.

Mukherjee, R. (2007). "Mechanical Properties of Impact-Assembled Nanoparticle Composites: Fabrication, Measurements, and Simulation", in *Mechanical Engineering*, University of Minnesota, Mineneapolis.

Murray, C. B., Norris, D. J. and Bawendi, M. G. (1993). "Synthesis and characterization of nearly monodisperse CdE (E = sulfur, selenium, tellurium) semiconductor nanocrystallites". *Journal of the American Chemical Society* 115:8706-8715.

Murray, C. B., Kagan, C. R. and Bawendi, M. G. (2000). "Synthesis and Characterization of Monodisperse Nanocrystals and Close-packed Nanocrystal Assemblies". *Annual Review of Materials Science* 30:545-610.

Murray, C. B., Sun, S. H., Gaschler, W., Doyle, H., Betley, T. A. and Kagan, C. R. (2001). "Colloidal Synthesis of Nanocrystals and Nanocrystal Superlattices". *IBM Journal of Research and Development* 45:47-56.

Oertel, D. C., Bawendi, M. G., Arango, A. C. and Bulovic, V. (2005). "Photodetectors based on treated CdSe quantum-dot films". *Applied Physics Letters* 87:213505-213503.

Osedach, T. P., Geyer, S. M., Ho, J. C., Arango, A. C., Bawendi, M. G. and Bulovic, V. (2009). "Lateral heterojunction photodetector consisting of molecular organic and colloidal quantum dot thin films". *Applied Physics Letters* 94:043307-043303.

Pang, J., Stuecker, J. N., Jiang, Y., Bhakta, A. J., Branson, E. D., Li, P., III, J. C., Sutton, D., Calvert, P. and Brinker, C. J. (2008). "Directed Aerosol Writing of Ordered

Silica Nanostructures on Arbitrary Surfaces with Self-Assembling Inks". *Small* 4:982-989.

Park, J. U., Hardy, M., Kang, S. J., Barton, K., Adair, K., Mukhopadhyay, D. K., Lee, C. Y., Strano, M. S., Alleyne, A. G., Georgiadis, J. G., Ferreira, P. M. and Rogers, J. A. (2007). "High-Resolution Electrohydrodynamic Jet Printing". *Nature Materials* 6:782-789.

Park, K., Cao, F., Kittelson, D. B. and McMurry, P. H. (2002). "Relationship between Particle Mass and Mobility for Diesel Exhaust Particles". *Environmental Science & Technology* 37:577-583.

Park, K., Kittelson, D. and McMurry, P. (2004). "Structural Properties of Diesel Exhaust Particles Measured by Transmission Electron Microscopy (TEM): Relationships to Particle Mass and Mobility". *Aerosol Science and Technology* 38:881 - 889.

Peng, Z. A. and Peng, X. G. (2001). "Formation of high-quality CdTe, CdSe, and CdS nanocrystals using CdO as precursor". *Journal of the American Chemical Society* 123:183-184.

Peter Reiss, J. B., and Adam Pron (2002). "Highly Luminescent CdSe/ZnSe Core/Shell Nanocrystals of Low Size Dispersion". *Nano Letters* 2:781-784.

Potyondy, D. O. and Cundall, P. A. (2004). "A bonded-particle model for rock". *International Journal of Rock Mechanics and Mining Sciences* 41:1329-1364.

Qi, L., McMurry, P. H., Norris, D. J. and Girshick, S. L. (2010). "Micropattern Deposition of Colloidal Semiconductor Nanocrystals by Aerodynamic Focusing". *Aerosol Science and Technology* 44:55 - 60.

Reiss, P., Bleuse, J. and Pron, A. (2002). "Highly luminescent CdSe/ZnSe core/shell nanocrystals of low size dispersion". *Nano Letters* 2:781-784.

Ridley, B. A., Nivi, B. and Jacobson, J. M. (1999). "All-Inorganic Field Effect Transistors Fabricated by Printing". *Science* 286:746-749.

Robel, I., Subramanian, V., Kuno, M. and Kamat, P. V. (2006a). "Quantum Dot Solar Cells: Harvesting Light Energy with CdSe Nanocrystals Molecularly Linked to Mesoscopic TiO2 Films". *Journal of the American Chemical Society* 128:2385-2393.

Schapotschnikow, P., Pool, R. and Vlugt, T. J. H. (2008). "Molecular simulations of interacting nanocrystals". *Nano Letters* 8:2930-2934.

Scheckman, J. H. (2008). "Mass-Mobility Relationship for Silica Agglomerates: Implications for Transport and Morphological Properties", in *Mechanical Engineering*, University of Minnesota, Minneapolis.

Scheckman, J. H., McMurry, P. H. and Pratsinis, S. E. (2009). "Rapid Characterization of Agglomerate Aerosols by In Situ Mass−Mobility Measurements". *Langmuir* 25:8248-8254.

Shaffer, S. A., Tang, K. Q., Anderson, G. A., Prior, D. C., Udseth, H. R. and Smith, R. D. (1997). "A novel ion funnel for focusing ions at elevated pressure using electrospray ionization mass spectrometry". *Rapid Communications in Mass Spectrometry* 11:1813-1817.

Singh, M., Haverinen, H. M., Dhagat, P. and Jabbour, G. E. (2010). "Inkjet Printing - Process and Its Applications". *Advanced Materials* 22:673-685.

Snee, P. T., Chan, Y. H., Nocera, D. G. and Bawendi, M. G. (2005). "Whispering-Gallery-Mode Lasing from a Semiconductor Nanocrystal/Microsphere Resonator Composite". *Advanced Materials* 17:1131-1136.

Soreni-Harari, M., Mocatta, D., Zimin, M., Gannot, Y., Banin, U. and Tessler, N. (2010). "Interface Modifications of InAs Quantum-Dots Solids and Their Effects on FET Performance". *Advanced Functional Materials* 20:1005-1010.

Steckel, J. S., Coe-Sullivan, S., Bulovic, V. and Bawendi, M. G. (2003). "1.3 mu m to 1.55 mu m tunable electroluminescence from PbSe quantum dots embedded within an organic device". *Advanced Materials* 15:1862-1866.

Steckel, J. S., Snee, P., Coe-Sullivan, S., Zimmer, J. P., Halpert, J. E., Anikeeva, P., Kim, L.-A., Bulovic, V. and Bawendi, M. G. (2006). "Color-Saturated Green-Emitting QD-LEDs". *Angewandte Chemie International Edition* 45:5796-5799.

Stolzenburg, M. R. and McMurry, P. H. (1991). "An Ultrafine Aerosol Condensation Nucleus Counter". *Aerosol Science and Technology* 14:48 - 65.

Sun, Q., Wang, Y. A., Li, L. S., Wang, D., Zhu, T., Xu, J., Yang, C. and Li, Y. (2007). "Bright, multicoloured light-emitting diodes based on quantum dots". *Nature Photonics* 1:717-722.

Suri, M. and Dumitrică, T. (2008). "Efficient sticking of surface-passivated Si nanospheres via phase-transition plasticity". *Physical Review B* 78:081405.

Suzuki, T., Imazeki, N., G. Yu, H. I. and Oda, M. (1997). "Direct Drawing System with Micro-Dispenser Using Dispersed Ultra Fine Particle Paste", in *IEMT/IMC Symposium, 1st Joint International Electronic Manufacturing Symposium and the International Microelectronics Conference*, 267-270.

Swihart, M. T. (2003). "Vapor-phase synthesis of nanoparticles". *Current Opinion in Colloid & Interface Science* 8:127-133.

Talapin, D. V. and Murray, C. B. (2005). "PbSe Nanocrystal Solids for n- and p-Channel Thin Film Field-Effect Transistors". *Science* 310:86-89.

Talapin, D. V., Lee, J.-S., Kovalenko, M. V. and Shevchenko, E. V. (2009). "Prospects of Colloidal Nanocrystals for Electronic and Optoelectronic Applications". *Chemical Reviews* 110:389-458.

Tekin, E., Smith, P. J., Hoeppener, S., van den Berg, A. M. J., Susha, A. S., Rogach, A. L., Feldmann, J. and Schubert, U. S. (2007b). "Inkjet Printing of Luminescent CdTe Nanocrystal-Polymer Composites". *Advanced Functional Materials* 17:23-28.

Valentini, P., Gerberich, W. W. and Dumitrică, T. (2007). "Phase-Transition Plasticity Response in Uniaxially Compressed Silicon Nanospheres". *Physical Review Letters* 99:175701.

Vanmaekelbergh, D. and Liljeroth, P. (2005). "Electron-Conducting Quantum Dot Solids: Novel Materials Based on Colloidal Semiconductor Nanocrystals". *Chemical Society Reviews* 34:299–312.

Wang, S. C. and Flagan, R. C. (1990). "Scanning Electrical Mobility Spectrometer". *Aerosol Science and Technology* 13:230-240.

Wang, X. L., Kruis, F. E. and McMurry, P. H. (2005a). "Aerodynamic focusing of nanoparticles: I. Guidelines for designing aerodynamic lenses for nanoparticles". *Aerosol Science and Technology* 39:611-623.

Wang, X. L., Gidwani, A., Girshick, S. L. and McMurry, P. H. (2005b). "Aerodynamic focusing of nanoparticles: II. Numerical simulation of particle motion through aerodynamic lenses". *Aerosol Science and Technology* 39:624-636.

Wang, X. L. and McMurry, P. H. (2006a). "An experimental study of nanoparticle focusing with aerodynamic lenses". *International Journal of Mass Spectrometry* 258:30-36.

Wang, X. L. and McMurry, P. H. (2006b). "A Design Tool for Aerodynamic Lens Systems". *Aerosol Science and Technology* 40:320-334.

Wood, V., Panzer, M. J., Caruge, J.-M., Halpert, J. E., Bawendi, M. G. and Bulović, V. (2009a). "Air-Stable Operation of Transparent, Colloidal Quantum Dot Based LEDs with a Unipolar Device Architecture". *Nano Letters* 10:24-29.

Wood, V., Panzer, M. J., Chen, J., Bradley, M. S., Halpert, J. E., Bawendi, M. G., Bulovi, V. and cacute (2009b). "Inkjet-Printed Quantum Dot-Polymer Composites for Full-Color AC-Driven Displays". *Advanced Materials* 21:2151-2155.

Yarin, A. L. (2006). "Drop impact dynamics: Splashing, spreading, receding, bouncing". *Annual Review of Fluid Mechanics* 38:159-192.

Yu, W. W., Qu, L. H., Guo, W. Z. and Peng, X. G. (2003a). "Experimental Determination of the Extinction Coefficient of CdTe, CdSe, and CdS Nanocrystals". *Chemistry of Materials* 15:2854-2860.

Yu, W. W., Qu, L. H., Guo, W. Z. and Peng, X. G. (2003b). "Experimental determination of the extinction coefficient of CdTe, CdSe, and CdS nanocrystals". *Chem. Mater.* 15:2854-2860.

Zhang, H., Han, J. and Yang, B. (2010). "Structural Fabrication and Functional Modulation of Nanoparticle-Polymer Composites". *Advanced Functional Materials* 20:1533-1550.

Zhao, J., Bardecker, J. A., Munro, A. M., Liu, M. S., Niu, Y., Ding, I. K., Luo, J., Chen, B., Jen, A. K. Y. and Ginger, D. S. (2006). "Efficient CdSe/CdS Quantum Dot Light-Emitting Diodes Using a Thermally Polymerized Hole Transport Layer". *Nano Letters* 6:463-467.

Zhu, T., Shanmugasundaram, K., Price, S. C., Ruzyllo, J., Zhang, F., Xu, J., Mohney, S. E., Zhang, Q. and Wang, A. Y. (2008). "Mist Fabrication of Light Emitting Diodes with Colloidal Nanocrystal Quantum Dots". *Applied Physics Letters* 92:023111.

Ziemann, P. J., Liu, P., Rao, N. P., Kittelson, D. B. and McMurry, P. H. (1995). "Particle Beam Mass Spectrometry of Submicron Particles Charged to Saturation in an Electron Beam". *Journal of Aerosol Science* 26:745-756.

Zu, L. (2006). "Doping Semiconductor Nanocrystals", in *Chemical Engineering and Materials Science*, University of Minnesota, Minneapolis.

Particle Flow Code in 3-Dimensions (PFC^{3D}), Version 3.1 Manuals.(2005) Itasca Consulting Group, Minneapolis, MN, USA.